INVESTIGATION OF THE TRANSIENT FUEL PREBURNER MANIFOLD AND COMBUSTOR

Final Report, Contract NAS8-37461
Report No. SECA-89-10

Prepared for

National Aeronautics and Space Administration
George C. Marshall Space Flight Center
Marshall Space Flight Center, AL 35812

By

Ten-See Wang
Yen-Sen Chen
Richard C. Farmer

SECA, Inc.
3311 Bob Wallace Avenue
Suite 213
Huntsville, AL 35805

June 1989

INVESTIGATION OF THE TRANSIENT FUEL PREBURNER MANIFOLD AND COMBUSTOR

Final Report, Contract NAS8-37461
Report No. SECA-89-10

Prepared for

National Aeronautics and Space Administration
George C. Marshall Space Flight Center
Marshall Space Flight Center, AL 35812

By

Ten-See Wang
Yen-Sen Chen
Richard C. Farmer

SECA, Inc.
3311 Bob Wallace Avenue
Suite 213
Huntsville, AL 35805

June 1989

TABLE OF CONTENTS

SUMMARY

A computational fluid dynamics (CFD) code with finite-rate reactions, FDNS2DR, has been developed to study the start transient of the Space Shuttle Main Engine (SSME) Fuel Preburner (FPB) operation. FDNS2DR is a versatile, pressure based, compressible/incompressible, implicit/explicit CFD code. It uses a time centered, time marching algorithm for time accuracy. An upwind scheme is employed for spatial discretization. The upwind scheme is based on second and fourth order central differencing with adaptive artificial dissipation. A state of the art two-equation turbulence model is employed for the turbulence calculation. A PARASOL chemistry algorithm is coupled with the point implicit procedure. In this study, FDNS2DR was benchmarked with three well documented experiments: a confined swirling coaxial jet, a non-reactive ramjet dump combustor and a reactive ramjet dump combustor. Excellent comparisons were obtained with the benchmark cases. The code was then used to study the start transient of an axisymmetric SSME fuel preburner. Excellent agreement was obtained for the temporal occurrence and magnitude of the temperature spikes in comparison with results obtained from an Aerojet experiment. Furthermore, it was also found in this study that an appreciable amount of unburned oxygen entered the turbine stages.

The significance of this study is that a time accurate CFD design tool has been developed to accurately predict the severe thermal gradients which are impressed upon the fuel preburner and turbine during the start transient. Previously, various factors were suspected to cause the ignition temperature spikes, such as the collection of unreacted propellants, a mismatch of the fuel and oxidizer supply rate, and mixture maldistribution prior and during ignition. These factors can now be studied, quantitatively. Numerical experiments can be designed for study with FDNS2DR to alter the ignition and shut down characteristics to attenuate the possible thermal loads.

TABLE OF FIGURES

NOMENCLATURE

A	a NxN species jacobian matrix
A_i	chemical symbol of the ith species
A_r	Arrhenius constant
ASI	subscript denotes augumented spark igniter flow properties
B	a N element column vector
C_{pn}	heat capacity for species n
C_1	turbulence model constant, =1.15 for k-ε(T) model =1.43 for standard k-ε model
C_2	turbulence model constant, =1.90 for k-ε(T) model =1.92 for standard k-ε model
C_3	turbulence model constant, =0.25
C_4	turbulence model constant, =0.6
C_μ	turbulence model constant, =0.09
c	local speed of sound
D	outer pipe diameter of ramjet dump combustor
d	dissipation term
E	activation energy
F	convection and diffusion fluxes
G	geometrical matrices
h	enthalpy
INJ	subscript denotes faceplate injector properties
J	Jacobian of coordinate transformation
J_n	diffusion flux for species n
K	chemical reaction rate
k	turbulent kinetic energy
M	molecular weight
N	total number of species
P	Pade' approximants in λth order
p	static pressure
p_c	fuel preburner chamber static pressure
Pr	turbulent kinetic energy production
Q	Pade' approximants in δth order
R	gas constant
REC	adaptive dissipation parameter
S	fuel preburner inlet area
S_q	source term for equation q
T	static temperature
T^*	ratio of static to room temperature
t	time
U	contravariant velocity
u	x-direction mean velocity
v	y-direction mean velocity
u'	updated transient inlet x-direction mean velocity
v'	updated transient inlet y-direction mean velocity
W_n	mass production rate for species n
W_i	mass flow rate of either fuel or oxidizer
W_T	total mass flow rate
x	physical coordinate
Y	α/M
Φ	energy dissipation function

ξ, η computational coordinate
μ_{eff} effective viscosity
μ molecular viscosity
μ_t turbulent eddy viscosity
ε turbulent kinetic energy dissipation rate
σ_q turbulence model constant for equation q. (σ_u=1.0, σ_ρ=0.9, σ_T=1.0, σ_k=0.8927 and $\sigma\varepsilon$=1.15 for k-ε{T} model, σ_k=1.0 and σ_ε=1.3 for standard k-ε model
α species mass fraction
ρ density
ρ' updated transient inlet density
β pressure relaxation parameter, =10.0
γ temperature dependency for Arrhenius equation
τ, chemistry time integration step
ν_{ik}', ν_{ik}'' stoichiometric coefficients
{ } denote functionality

INTRODUCTION

Numerous flow anomalies have been found in both the fuel and oxidizer preburners and turbine hot end parts. Cracks have been found on housings, Kaiser-hat nuts, struts, sheetmetal, nozzles and shrouds. After many studies and modifications to the preburner components, several problems remain with the SSME preburner operation, such as cracking of the first and second stage blade shanks, of the blade root fillets and under the blade platform. The damage is more severe on the fuel side since it operates at a higher power level and temperature. It is postulated that the extreme thermal environment during the start up transient produces the initial blade cracks; the severity of the cracks will depend on the specific transient operations the engine experiences. The cracks can continue to grow due to both high cycle fatigue and low cycle fatigue as the number of turbine load cycles accumulate. Other flow anomaly theories such as inefficient atomization and possible unmixedness of the gaseous oxygen during steady state operation are considered to be of secondary importance in creating locally excessive heating problems.

Computational analyses of the axisymmetric and three-dimensional FPB flowfield (ref. 1) indicated that under steady operating conditions, striated flows go through the preburner chamber with little turbulent mixing between the parallel shear layers. Mixing at the injector face is thought to be very rapid, and assuming that some mixing occurs immediately allows the entire flowfield to be simulated. These observations and assumptions are consistent with a computational analysis of a single injector element (ref. 2), in which the percentage of oxidizer atomization, vaporization and fuel/oxidizer reaction reached 100 percent almost immediately below the injection inlet. Results from such analyses show that striations severe enough to cause local streamlines to be at near stoichiometric mixture ratios should not be present at the inlet to the turbopump under steady-state operation of the preburner. Temperature measurements at the turbine inlet (ref. 3) shown in Fig. 1 show that two temperature spikes exist under start-up. Estimates of thermocouple response suggest that the actual temperatures are sufficiently high to create blade cracking (ref. 4). A transient fuel preburner thermal flowfield computational analysis was performed in this study in order to understand and make recommendations for improving the component life of the SSME engine.

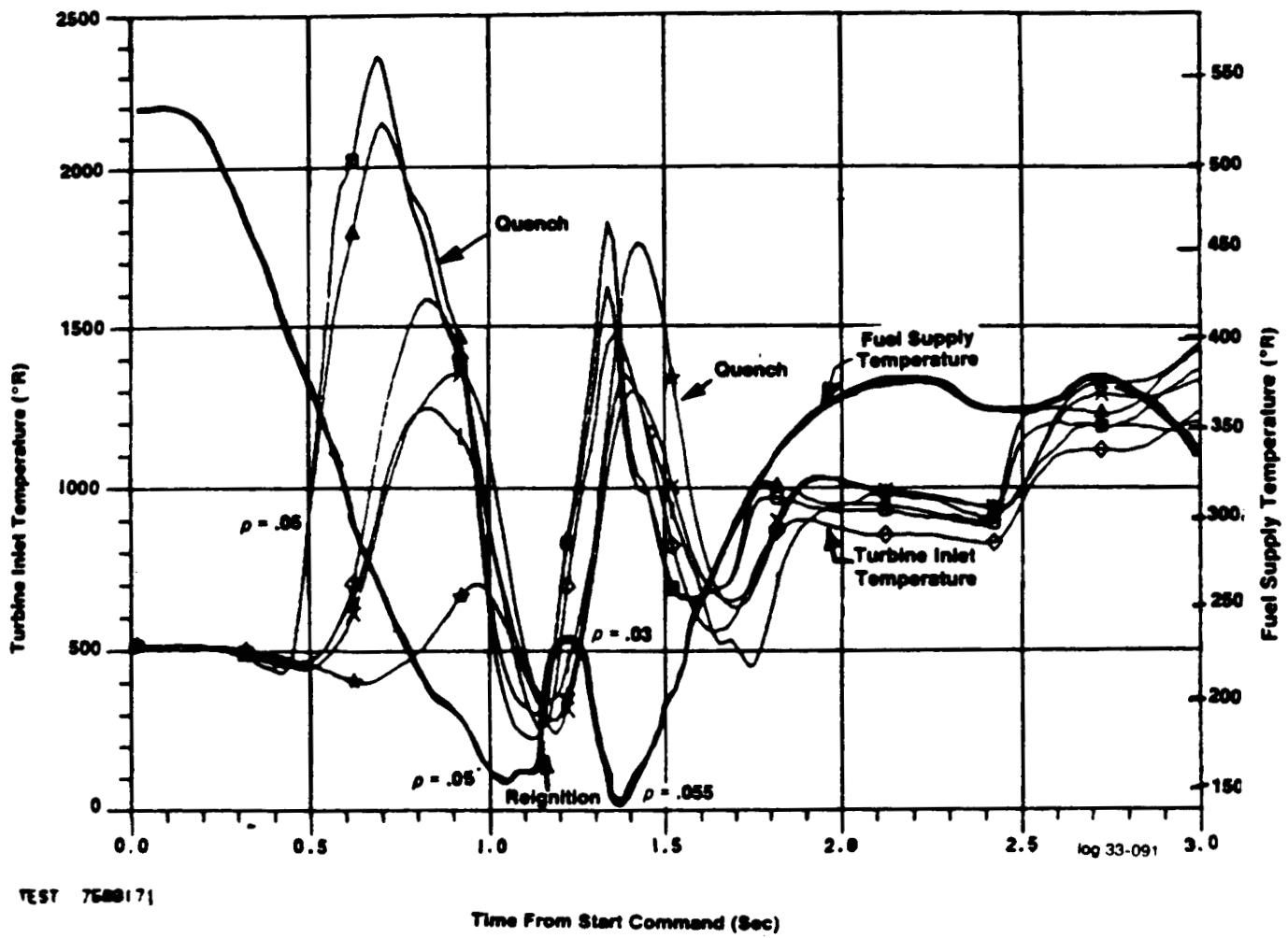

Fig. 1 Turbine inlet temperature.

TRANSIENT FUEL PREBURNER OPERATION

The configuration of the FPB is shown in Fig. 2. The flow passage from the fuel preburner oxidizer valve (FPOV) into the oxidizer manifold above the injector faceplate is shown in this figure. The oxidizer flow to the augmented spark igniter (ASI) is supplied from a bleed line from the FPOV. The FPOV is shown in Fig. 3. The valves which control the engine flows are shown schematically in Fig. 4. Notice there is not a fuel control valve for each preburner. Flows from the fuel and oxidizer manifolds enter the FPB chamber through the injector faceplate, the layout of which is shown in Fig. 5. These figures are from references 3 and 5.

The coaxial injectors and the ASI are designed to be high intensity mixers. The fact that additional hydrogen jets were required to mix the ASI flow indicate that the original design was not as sound as anticipated, nevertheless the current configuration does apparently avoid excessive hot spots on the turbopump dome. When simulating the preburner flowfield, it is not computationally feasible to resolve each flow injector or the detailed convective flows within the ASI. Rocketdyne has reported (ref. 6) experimental measurements of temperature, velocity, density gradients, and OH concentrations for single coaxial elements and for groups of four coaxial injector flows. These measurements showed that injectors create back-flow recirculation up to the injector faceplate, with the hydrogen from the bleed holes constituting the bulk of the fluid which is recirculated. If unmixed lumps of oxygen were present, the hot spheres of radiating OH shall be visible as the hot balls of gases react. Such flow structures were not observed, hence, large unmixedness effects of the oxygen probably does not exist. Ignition probes provide sparks that cause ignition. Initial flames move around until recirculating flows cause the entire near face flow to be ignited. The injector faceplate then acts as a flameholder. Incomplete mixing along the centerline of the coaxial jets cause the flow to be cool until sufficient hydrogen diffuses in to change the mixture ratios. These cool regions are roughly located from two to six inches downstream of the faceplate. These experiments support the contention that unmixedness is not a major factor in preburner flows. Detailed experiments of ASI flows are not available, but the ASI was designed so that tangential velocities of hydrogen cause the flow to be intensely mixed. Assuming that the hot spots on the turbopump dome were caused by ASI flow, the extra hydrogen which would have to remain unmixed suggests that a hot core surrounded by very cold, almost pure, hydrogen would have to exist. The modification which consisted of adding extra hydrogen jets on the baffle tips was apparently adequate to solve this problem, although, the simultaneous change in ASI start-up procedure may

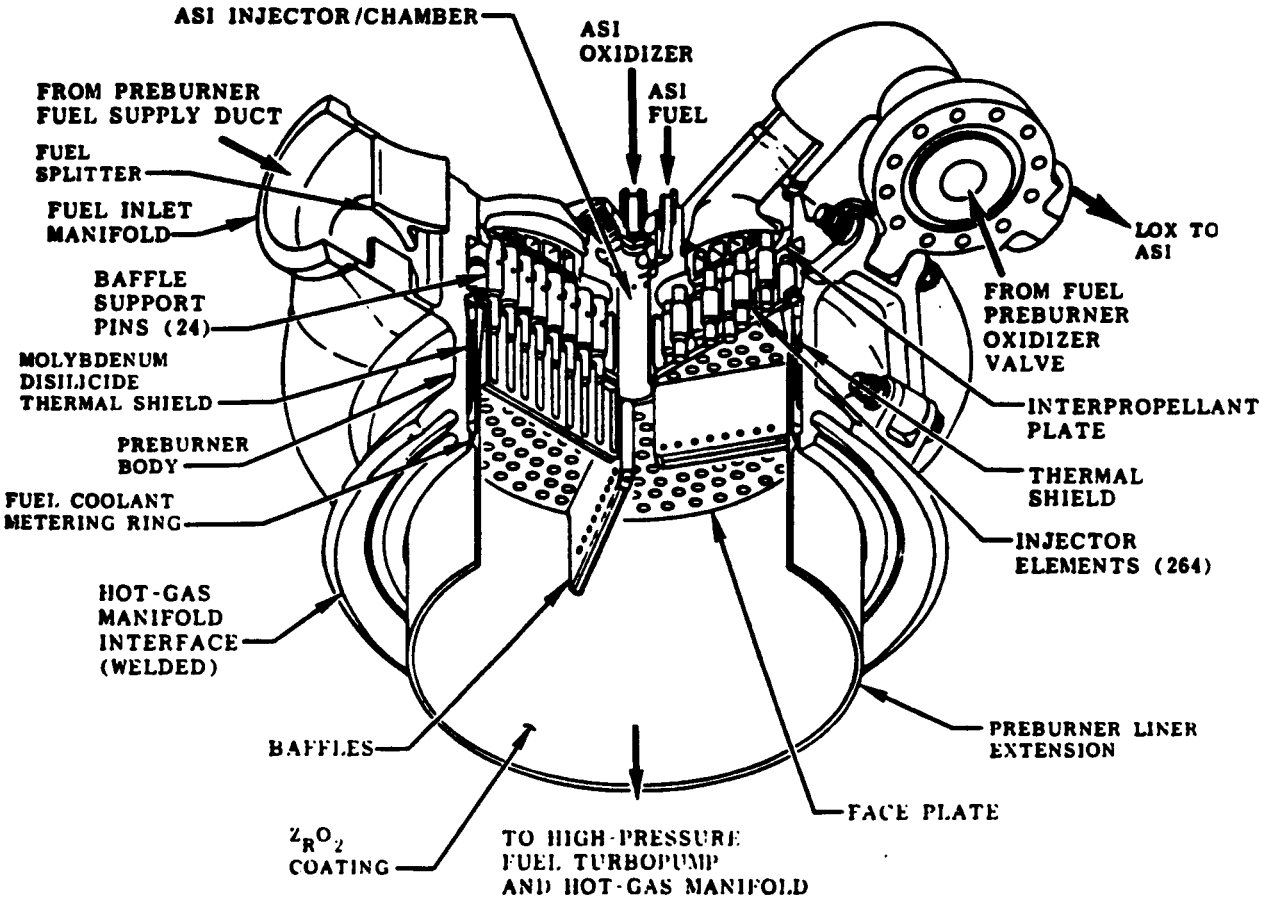

Fig. 2 Fuel preburner.

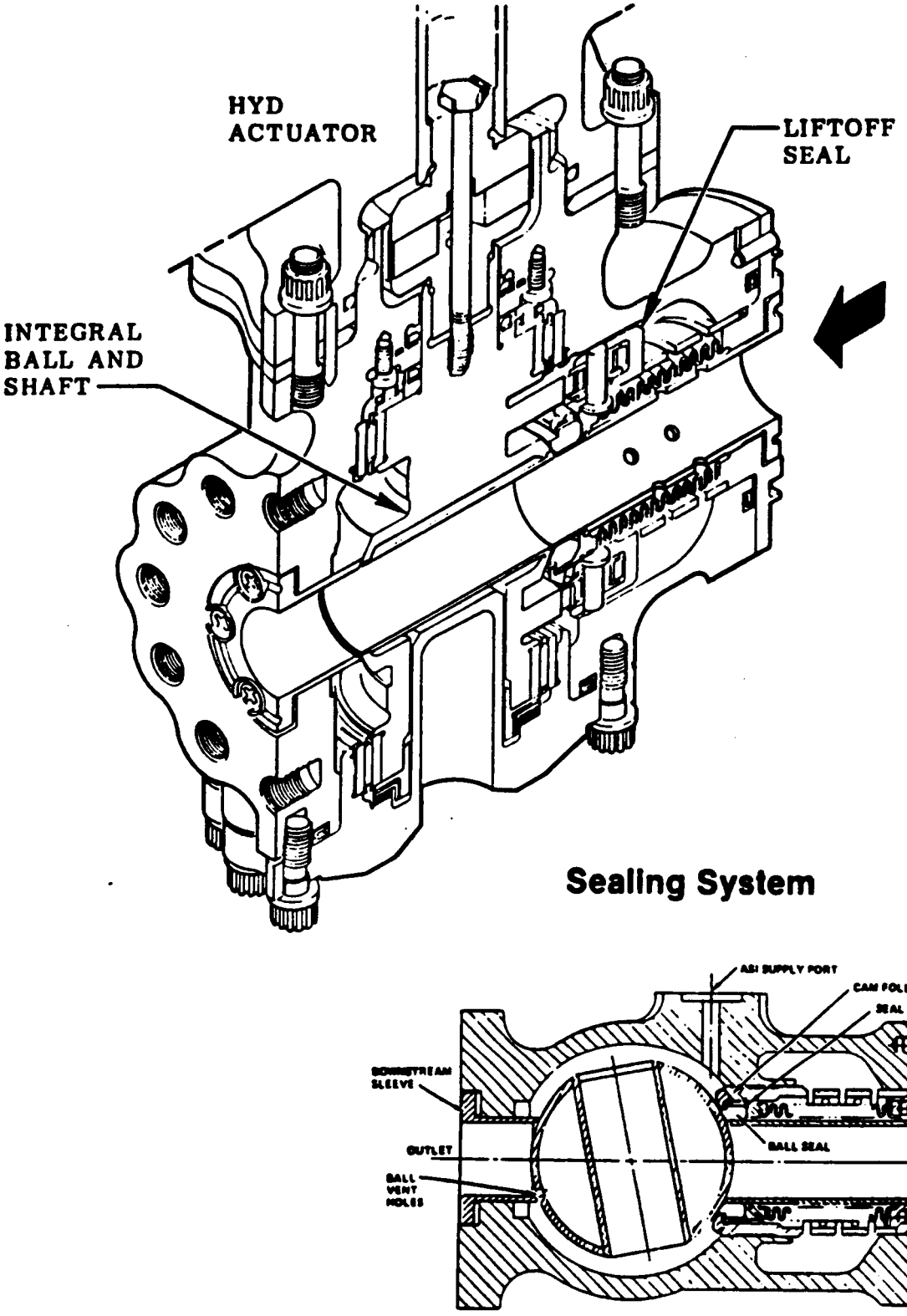

Fig. 3 SSME fuel preburner oxidizer valve assembly and sealing system.

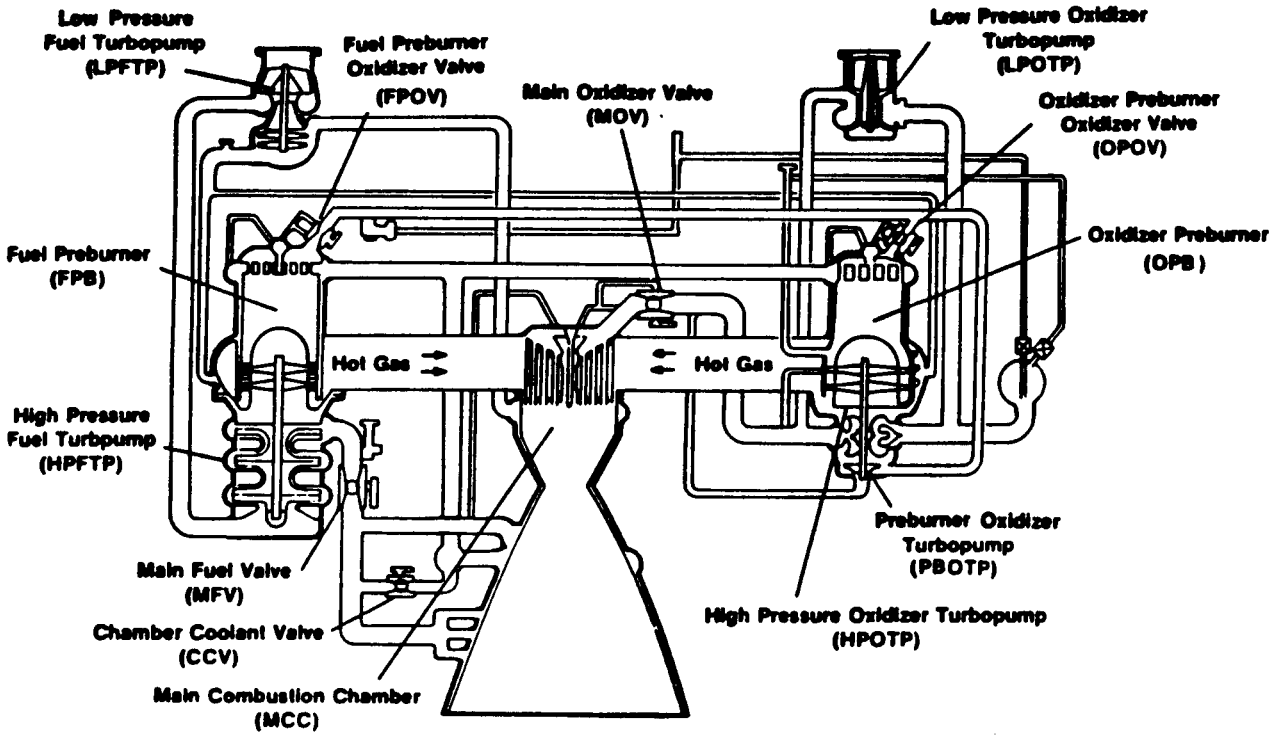

Fig. 4 SSME control valves.

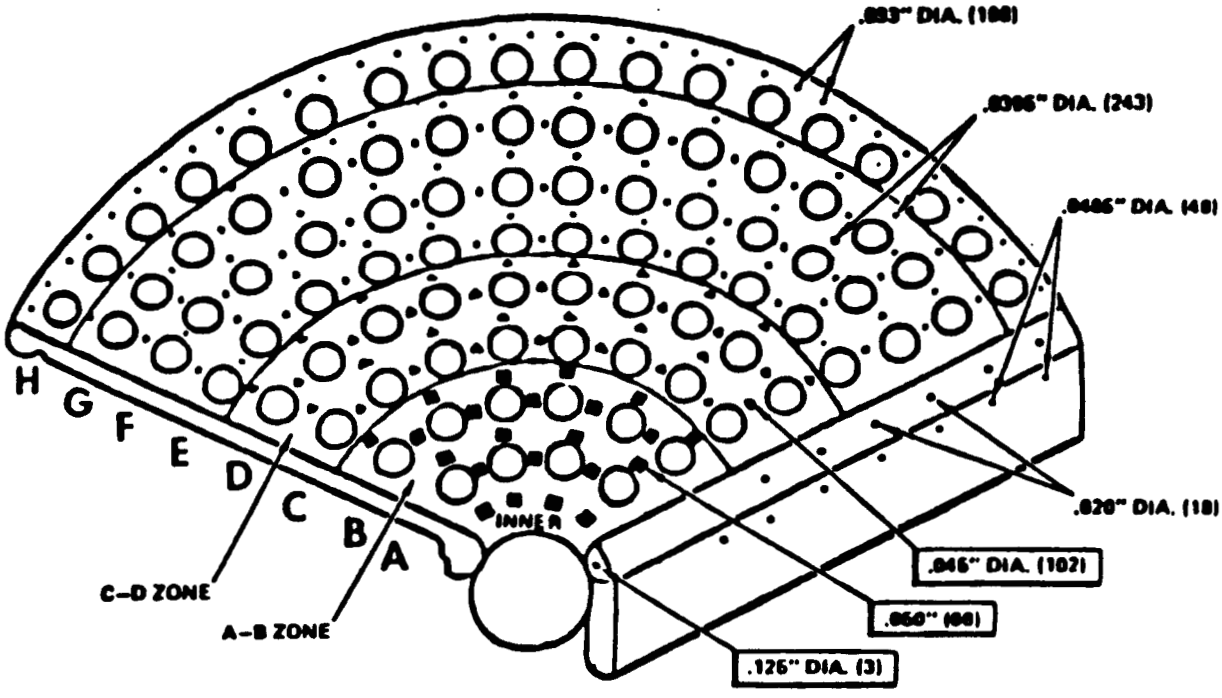

Fig. 5 The layout of SSME fuel preburner injector faceplate.

have been the actual cause of reducing the thermal loads in the turbopump dome. Computational analysis for single coaxial elements with the ARICC code (ref. 2) also suggests that atomization and combustion is complete in about two inches, although radial concentration gradients may still exist out to several more inches. An alternative analysis may also be considered by using Rosner's treatment (ref. 7) of supercritical combustion. This more elementary model treats the process as a one-dimensional mass diffusion with laminar diffusion coefficients. For a mean drop (or lump) size of 150 μm, combustion should be complete in about two inches. These analyses are admittedly approximate but they offer no justification for arbitrarily delaying the mixing (by fixing transport coefficients) until oxygen globules are present at the preburner exit, during steady state operation. Since unmixedness appears to unlikely cause of turbine blade heating, what other explanations can be postulated? This is the motivation for a transient FPB study.

The turbine inlet temperature measurements reported in ref. 3 and the one-dimensional, transient start-up analyses performed by ref. 8 indicate that transient flow phenomena may be the cause of high thermal loads on turbine blades. Operations of the preburners are designed to have a fuel lead, but the starting flows of oxygen may be much different from those at steady state operation. Two scenarios can be used to explain the transient flow phenomena of the fuel preburner operation. The first scenario recognizes that under both steady and transient start-up the hydrogen is at gaseous state. But gaseous oxygen (GOX) is probably the first oxidizer to flow into the preburner although LOX is injected at steady-state. Actually, these flows are even more complicated because valve sequencing and transient heat transfer must be considered in detail to describe these multi-dimensional, unsteady flows. Interpreting these flows is even further complicated by the fluid state being supercritical with respect to pressure. If LOX flashes to GOX as it flows into the unchilled LOX dome, then GOX will flow through the injectors for some brief period of time. Such GOX flow might make the preburner leaner than expected before steady state flow is established. The second scenario considers the response of the flow in the fuel supply line to the increase of pressure in the combustion chamber. Remember there is no fuel control valve in the fuel supply line, as shown in Fig. 4. The engine main fuel valve begins to ramp open at the start command, and the FPB oxidizer valve begins to open at about 0.1 of a second. Propellants begin to accumulate in the preburner but do not react. Combustion does not actually begin until about 0.4 of a second, when the turbine inlet temperature begins to rise. The preburner chamber pressure also starts to rise after about 0.4 seconds during the priming process. The pressure rise rate is quite steep after the priming event. A pressure wave would be felt upstream of the faceplate. The fuel supply line would feel the pressure increase and shut down the fuel supply momentarily. To compensate for the fuel flow loss, the oxidizer flow rate will

have a temporary increase. This combination of fuel flow loss and oxidizer flow gain would create a temporarily leaner mixture ratio in the chamber.

Aerojet (ref. 3) studied the engine test data and concluded that the two temperature spikes which are observed on start-up are due to burning of propellants accumulated in the combustion chamber and extinguishment caused by cold slugs of fuel flowing into the FPB before the steady-state is achieved. Seymour (ref. 8) has made an extensive DTM study and concluded that temperature spikes are closely associated with the decline of the fuel supply which occurs during start-up. These observations are thought to favor the second scenario, although they do not totally exclude the possibility of the first one. The DTM simulation also provides the precise sequencing of control valves and the reaction of the fuel supply line to the pressure wave, which are thought to be the dominating factor of the transient FPB operation by the second scenario. It is therefore proposed in this study that the result of the DTM simulation be used as the input for the transient FPB thermal flowfield study.

Since the results of Seymour's study were not available at the beginning of this investigation, an analysis using the first scenario as the possible explanation of the transient mechanism was initiated. Two codes, COBRA/TRAC and FDNS were evaluated for use in describing the transient flow of GOX into the inlet manifold to the preburner and the subsequent chilling of the manifold. It was determined that either of these codes could be used for making the required analysis, if suitable oxygen property data were available. A general procedure for the calculation of the thermodynamic and transport properties for two phase oxygen was prepared and is included in the Appendix for future usage. However, when Seymour's analysis revealed that the relative flows of the two propellants could possibly explain the temperature spikes, development of the first scenario was terminated in order to evaluate the second one.

Based on the considerations just presented, it was determined that the transient fuel preburner could best be simulated by including finite-rate combustion reactions in the FDNS code and using the DTM to represent the unsteady upstream boundary conditions. The reacting FDNS code was developed, validated with several test cases, and the transient operation of the fuel preburner was simulated. The results of these analyses are described in the following sections of this report.

FDNS METHODOLOGY

Governing Equations

The basic equations employed in this study to describe a general combustor flowfield are the axisymmetric, multi-component conservation equations. A generalized form of these equations written in curvilinear coordinates is given by

$$(1/J)(\partial \rho q/\partial t) = \partial[-\rho U_i q + \mu_{eff} G_{ij}(\partial q/\partial \xi_j)]/\partial \xi_i + S_q \qquad (1)$$

where J, U_i and G_{ij} represent the Jacobian of the coordinate transformation, contravariant velocities and diffusion metrics respectively. They are written as:

$$J = \partial(\xi,\eta)/\partial(x,y)$$

$$U_i = (u_j/J)(\partial \xi_i/\partial x_j)$$

$$G_{ij} = (\partial \xi_i/\partial x_k)(\partial \xi_j/\partial x_k)/J \qquad (2)$$

$\mu_{eff} = (\mu + \mu_t)/\sigma_q$ is the effective viscosity when the turbulent eddy viscosity concept is employed to model the turbulent flows. $\mu_t = \rho C_\mu k^2/\varepsilon$, is the turbulence eddy viscosity and C_μ and σ_q denote turbulence modeling constants. Source terms S_q are given by

$$S_q = (1/J) \begin{bmatrix} 0 \\ -p_x + \nabla[\mu_{eff}(u_j)_x] \\ -p_y + \nabla[\mu_{eff}(u_j)_y] \\ Dp/Dt + \Phi + \sum J_n C_{pn} \nabla T - \sum h_n W_n \\ \rho(P_r - \varepsilon) \\ \rho(\varepsilon/k)(C_1 P_r - C_2 \varepsilon + C_3 T^* C_4 Pr^2/\varepsilon) \\ W_n \\ n = 1,\ldots,N \end{bmatrix} \qquad (3)$$

The equation of state for an ideal gas is used to close the above system of equations.

Numerical Schemes

The spatial accuracy of numerical schemes for finite

difference or finite volume Navier-Stokes solvers applied to convection dominated flow problems depends strongly on the order of approximation in discretizing the convection fluxes. In recent years, many numerical schemes have been developed for high to low speed flows based on the concept of upwind differencing. The flux vector splitting schemes (refs. 9 and 10), the flux difference schemes (refs. 11 - 13) and central plus artificial dissipation schemes (refs. 14 - 16) are the most commonly used. All these schemes approximately follow the characteristics of the flow by an upwinding treatment of the numerical fluxes, while attempting to satisfy the conservation laws. Numerical accuracy of second-order or higher can be attained throughout the entire flow field except near regions of sharp gradients, e.g. shock wave discontinuities. It is also a common practice to use first-order upwind schemes near shock waves to maintain monotonicity of the solutions; this practice is justified by the total variation diminishing concept (ref. 13).

It is also known that both flux splitting and flux difference methods require certain matrix operations in order to construct an upwind scheme based on the eigenvalues of the flux Jacobian matrices. On the other hand, the methods of MacCormack and Jameson require no extra matrix operations. Additional savings in computational time are achieved when artificial dissipation methods are employed. As has been pointed out by Pulliam (ref. 17), artificial dissipation methods can be very accurate and do not exhibit numerical oscillations near shock waves, if they are constructed to reflect the same features as the flux vector upwind methods.

In the present development, an upwind scheme was employed to approximate the convective terms of the momentum, energy and continuity equations; the scheme is based on second and fourth order central differencing with artificial dissipation. First order upwinding is used for the species and turbulence equations, since the parameters involved are positive quantities. Different eigenvalues are used for weighing the dissipation terms depending on the conserved quantity being evaluated, in order to give correct diffusion fluxes near wall boundaries. This procedure is different from those proposed in other works (refs. 13 - 15) in which the sum of the absolute value of the convection velocity and the local speed of sound is used to weigh the dissipation terms. For simplicity, let us consider fluxes in ξ-direction only. That is,

$$\partial F/\partial \xi \cong (F_{i+1} - F_{i-1})/2 - (d_{i+1/2} - d_{i-1/2}) \qquad (4)$$

The dissipation terms are constructed such that a fourth-order central and fourth-order damping scheme is activated in smooth regions, and a second-order central and second-order damping scheme is used near shock waves. Since the Jacobian matrices of the Euler fluxes have eigenvalues of U, U+c and U-c, it is sufficient to use the magnitudes of these eigenvalues to weigh the dissipation terms to maintain the smoothness of the

solution without losing accuracy. It is suggested in this study that |U|+c should be used for the continuity equation and |U| should be used for other transport equations. A general form of the dissipation term is given below.

$$d_{i+1/2} = 0.25[2\varepsilon_1|\rho U| + \varepsilon_2(|U|+c)]_{i+1/2}$$
$$(q_{i+1} - q_i) + [\varepsilon_3(1-\varepsilon_1)MAX[0.5$$
$$\Delta s\rho(|u|+|v|),2|\rho U|] + \varepsilon_4(|U|+c)]_{i+1/2}$$
$$(q_{i-1} - 3q_i + 3q_{i+1} - q_{i+2}) \qquad (5)$$

where $a_i = |p_{i+1} - 2p_i + p_{i-1}|/(p_{i+1} + 2p_i + p_{i-1})$

$$\upsilon_{i+1/2} = MAX(a_i, a_{i+1})$$

$$d_1 = MAX[REC,MIN(1.0,25\upsilon_{i+1r/2})]$$

$$d_4 = MAX(0.0, 0.01-0.25\upsilon_{i+1/2})$$

Different values for ε_1, ε_2, ε_3 and ε_4 are used for the continuity, energy and momentum transport equations. Table 1 summarizes these parameters.

Table 1. Dissipation Parameters

	Momentum & Energy	Continuity
ε_1	d_1	0
ε_2	0	$\upsilon_{i+1/2}$
ε_3	0.015	0
ε_4	0	d_4

A pressure based solution method was selected so that a wide range of flow speeds could be analyzed with the same code. Successful results of viscous flow computations using pressure based methods have been reported (refs. 18 and 19). For high speed flow cases, a hyperbolic pressure correction equation was employed by perturbing the density in the mass conservation equation. This provides a smooth transition from low to high speed flow characteristics. For time accuracy, a time-centered, time-marching scheme with a multiple pressure corrector algorithm was employed. In general, a noniterative time-marching scheme was used for time dependent flow computations; however, subiterations can be used if necessary.

To solve the system of nonlinear coupled partial differential equations, Eq. 1, finite difference approximations were used to establish a system of linearized algebraic

equations. A relaxation solution procedure was employed to couple the governing equations. For convenience, Eq. 1 was rewritten as:

$$(1/J)(\partial \rho q/\partial t) = -\partial F_i/\partial \xi_i + S_q = R_q \qquad (6)$$

First, Eq. (6) is discretized in time with a time-centered (Crank-Nicholson) scheme. That is,

$$(1/J\Delta t)[(\rho q)^{n+1} - (\rho q)^n] = (R_q^{n+1} + R_q^n)/2 \qquad (7)$$

where the superscript ^{n} denotes the current time level. If a sub-iteration procedure within a time step is applied, the following linearization can be incorporated.

$$(\rho q)^{n+1} = (\rho q)^k + \rho^n \Delta q^k \qquad (8)$$

$$R_q^{n+1} = (\partial R_q/\partial q)^k \Delta q + R_q^k \qquad (9)$$

where the superscript ^{k} denotes the k-th sub-iteration. With the above approximations, the final form of the time-marching scheme can be written as:

$$[(\rho^n/J\Delta t) - (\partial R_q/\partial q)^k]\ \Delta q^k$$

$$= -(1/J\Delta t)[(\rho q)^k - (\rho q)^n] + (R_q^k + R_q^n)/2 \qquad (10)$$

The solution at time level n+1 is then updated by:

$$q^{n+1} = q^{k+1} = q^k + \Delta q^k \qquad (11)$$

When k = 1 is selected, a non-iterative time-marching scheme is used. As reported in ref. 18, the non-iterative time-marching scheme with a multi-corrector solution method can provide time accurate solutions for transient flow problems. This multi-corrector procedure will be described below.

A simplified momentum equation was combined with the continuity equation to form a pressure correction equation. This pressure correction equation exhibits elliptic behavior for low speed flow and becomes continuously more hyperbolic as flow speed increases. The simplified momentum equation can be written as:

$$\partial \rho u_i/\partial t \cong -\nabla p' \qquad (12)$$

or, in discrete form,

$$u'_i \cong -\beta(\Delta t/\rho)\nabla p' \qquad (13)$$

where β represent a pressure relaxation parameter (β = 10 was used for all test cases in this paper). The velocity and density fields in the continuity equation are then perturbed to form a correction equation. That is,

$$\nabla(\rho u_i)^{n+1} = \nabla[(\rho^n + \rho')(u^n{}_i + u'_i)] = 0 \qquad (14)$$

By neglecting the $\rho'u'$ terms, the following equation results.

$$\nabla(u_i\rho') + \nabla(\rho u'_i) = -\nabla(\rho u_i)^n \qquad (15)$$

Substituting Eq. (13) into Eq. (15) and letting $\rho' = p'/RT$, the following pressure correction equation is obtained.

$$\nabla[(u_i/RT)p'] - \nabla(\beta\Delta t\ \nabla p') = -\nabla(\rho u_i)^n \qquad (16)$$

To provide smooth shock solutions the adaptive dissipation terms described above were added to the right hand side of Eq. (16). Once solution of Eq. (16) is obtained, the velocity field and the pressure field are updated through Eq. (13) and the following relation.

$$p^{n+1} = p^n + p' \qquad (17)$$

The density field is then updated by applying the equation of state. To ensure that the updated velocity, density and pressure fields satisfy the continuity equation, the above pressure correction solution procedure is repeated several times (usually 4 times are sufficient) before marching to the next time step. This represents a multi-corrector solution procedure.

To solve the system of linear algebraic equations, a semi-implicit matrix solver (ref. 20) was utilized. This matrix solution algorithm is a modified Stone's method (ref. 21). This method has been reported to be very efficient for matrix systems resulting from complex curvilinear coordinates systems including high aspect ratios and high grid skewness. However, this method does require a large amount of memory.

PARASOL, a Finite Rate Chemistry Algorithm

The finite rate chemistry source terms were evaluated with a point implicit procedure before the species equations were solved. The source term was solved by an improved algorithm, PARASOL (Pade' Rational Solution). This algorithm was first proposed by ref. 22 for stiff chemistry systems. The improvement made in this study was to incorporate LINPACK (ref. 23) , instead of the original Crout's method, to solve the matrix system. A benchmark case involving twelve reactions and eleven species in a streamtube calculation resulted in fifty times reduction in CPU time in comparison to the Crout's method.

Consider a general chemical system of N species undergoing m simultaneous elementary reactions

$$\sum_{i=1}^{N} \nu'_{ik} A_i \;===\; \sum_{i=1}^{N} \nu''_{ik} A_i, \qquad k=1,2,.....m \tag{18}$$

The source term S_{gi} for volumetric chemical reaction mass production rate of species i is

$$S_{gi} = \rho(d\alpha_i/dt)$$

$$= M_i \sum_{k=1}^{m} (\nu''_{ik}-\nu'_{ik})[K_{fk} \prod_{r=1}^{N} (\rho y_r)^{\nu rk}$$

$$- K_{bk} \prod_{r=1}^{N} (\rho y_r)^{\nu rk}], \tag{19}$$

$$i=1,2,.....N$$

Eq. (19) is a set of coupled, nonlinear system of stiff ordinary differential equations for general combustion systems. The stiffness comes from the inherent, widely disparate time constants of the nonlinear terms in Eq. (19). The stiffness can also be interpreted as the drastic change of local eigenvalues occurred near a flame front (ref.24). PARASOL started by casting Eq. (19) in a general form

$$dy/dt = f\{y, T, \rho\} \tag{20}$$

Nonlinear instability will occur if Eq. (20) were to be solved directly with even modest time steps. Locally linearizing Eq. (20) through the first order terms, and assuming the temperature change is small within an integration step, yields a system of linear ordinary differential equations with constant coefficients and can be regrouped as

$$dy/dt = A\ y\{t\} + B \tag{21}$$

The formal solution of Eq.(21) at $t=\tau$ is

$$y\{\tau\} = \exp\{\tau A\}(y_o + A^{-1}B) - A^{-1}B \tag{22}$$

In Eq.(22), the matrix exponential term can not be evaluated directly but may be approximated as polynomials, and the form of the approximation will determine whether it is accurate, efficient and stable. For a family of unconditionally stable schemes, the Pade' approximants are found to be more efficient than the other approximants. The Pade' approximation of the matrix exponential of Eq.(23) can be expressed as

$$\exp(\tau A) = Q^{-1}P + O(\tau A)^{\lambda+\delta+1} \tag{23}$$

while

$$P = \sum_{k=0}^{\lambda} \frac{(\lambda + \delta - k)!\lambda!}{(\lambda + \delta)!k!(\delta - k)!} (\tau A)^k \qquad (24)$$

and

$$Q = \sum_{k=0}^{\delta} \frac{(\lambda + \delta - k)!\delta!}{(\lambda + \delta)!k!(\delta - k)!} (-\tau A)^k \qquad (25)$$

The truncation error means that these formula must agree with the exponential power series for at least $\lambda + \delta + 1$ terms. Substituting the approximants into Eq. (22), the integration formula becomes

$$y(h) = Q^{-1}[Py_o + (P - Q)A^{-1}B] \qquad (26)$$

The diagonal Pade' approximants ($\delta = \lambda$) have the smallest truncation error of these approximants and are A-stable. The integration formula Eq. (26) can be derived for any order of truncation. Fifth order polynomials (p = q = 2) were found to be sufficient in this study. An automatic species jacobian writer was also developed in this study.

Turbulence Modeling

k-ε{T} Turbulence Model

The two-equation k-ε turbulence modeling approach was employed in the present study to describe the flowfield. The conventional wall function approach was used for near wall boundary conditions. It has been shown that in the extended k-ε model (ref. 25), two time scales (the production range time scale, k/Pr, and the dissipation rate time scale, k/ε) can be included in the dissipation rate equation to cause the dissipation rate to respond more effectively to the mean strain than it does in the standard k-ε model. The net effect of that energy transfer function is to enhance the development of ε when the mean strain is strong and suppress its production when the main strain is weak. The source term for the dissipation rate equation is:

$$S_\varepsilon = \rho(C_1 Pr\varepsilon/k - C_2\varepsilon^2/k + C_3 Pr^2/k) \qquad (27)$$

The last term represents the energy transfer from large scale turbulence to small scale turbulence controlled by the production range scale and the dissipation rate time scale. This formulation enables the dissipation rate to control the development of the turbulent kinetic energy more effectively. It has proved to be effective for isothermal flows such as boundary layer type flows and general elliptic type flows. For non-isothermal flows such as a chemically reacting flow in a ramjet dump combustor configuration, the isothermal standard k-ε and extended k-ε models predicted too rapid a decay of the centerline kinetic energy profile. The extended k-ε model did predict a slower centerline velocity decay than the standard k-ε model. It was therefore postulated that a temperature dependent term could be added to the last term of Eq. (27) for non-isothermal flows, without changing the modeling constants already determined for the isothermal turbulent flows. The value of the temperature dependency term would be unity for isothermal flows and provides no effect for the turbulent flowfield. The rationale behind this new turbulence model (k-ε{T}) is that the temperature rise in the reacting flow would cause an increase in the dissipation rate, and the net effect would be a reduced effective viscosity and a longer recirculation zone in a recirculating flow environment. The final expression for the dissipation rate equation source term is

$$S_\varepsilon = \rho(C_1 Pr\varepsilon/k - C_2\varepsilon^2/k + C_3(T^*)^{C4} Pr^2/k) \qquad (28)$$

The final values of these model constants for k-ε{T} turbulence model are: C_1=1.15, C_2=1.9, C_3=0.25 and C_4=0.6. Note that the temperature dependence has been established only for the reactive ramjet dump combustor experiment.

Chemistry Modeling

One Step Reversible H2/O2 Kinetics

To study the reactive hydrogen/oxygen system with the elliptic Navier-Stokes equations, the introduction of a detailed chemical reaction mechanism is often cost prohibitive. Simplification of the reaction system while maintaining important combustion characteristics is a rational strategy for reactive flow modeling. This idea has been developed as a quasi-global kinetics model for complex hydrocarbon fuels like NO. 2 fuel oil and coal derived fuels (refs. 26 and 27). For hydrogen/air combustion, a seven reaction mechanism has been proposed in ref. 28. Recently a two reaction global (ref. 29) was proposed for supersonic Scramjet combustor calculation by comparing the ignition delay times with a 28 reaction mechanism. This two reaction model consists of four species, therefore five species equations are needed for a hydrogen/air combustion calculation. In this study, a one step reversible H2/O2 kinetics model was proposed and the reaction model is given by

$$H_2 + 0.5\ O_2 = H_2O \qquad (29)$$

The reaction rates are functions of temperature and are usually expressed in a general Arrhenius form. For example, the forward reaction rate can be expressed as

$$K_f = A_r T^{\gamma} \exp\{-E/RT\} \qquad (30)$$

The rate constants for the forward reactions are: A_r=1.1068E6, γ=0.5 and E=8568.9; and for the reverse reaction: A_r=1.0E5 and E=19870.0.

The rate constants were obtained through parameter optimization by comparing the ignition delay times and the temperature histories with those predicted from a 28 reaction mechanism. Fig. 6 and 7 shows the comparison of the one-step model with the 28 reaction mechanism for H_2-air combustion. The predicted temperature profiles and the ignition delay times for the one step model agreed well with those from the 28 reaction mechanism. It is not implied that these simplified kinetics rate constants have general applicability, merely that they are useful under conditions where they have been verified.

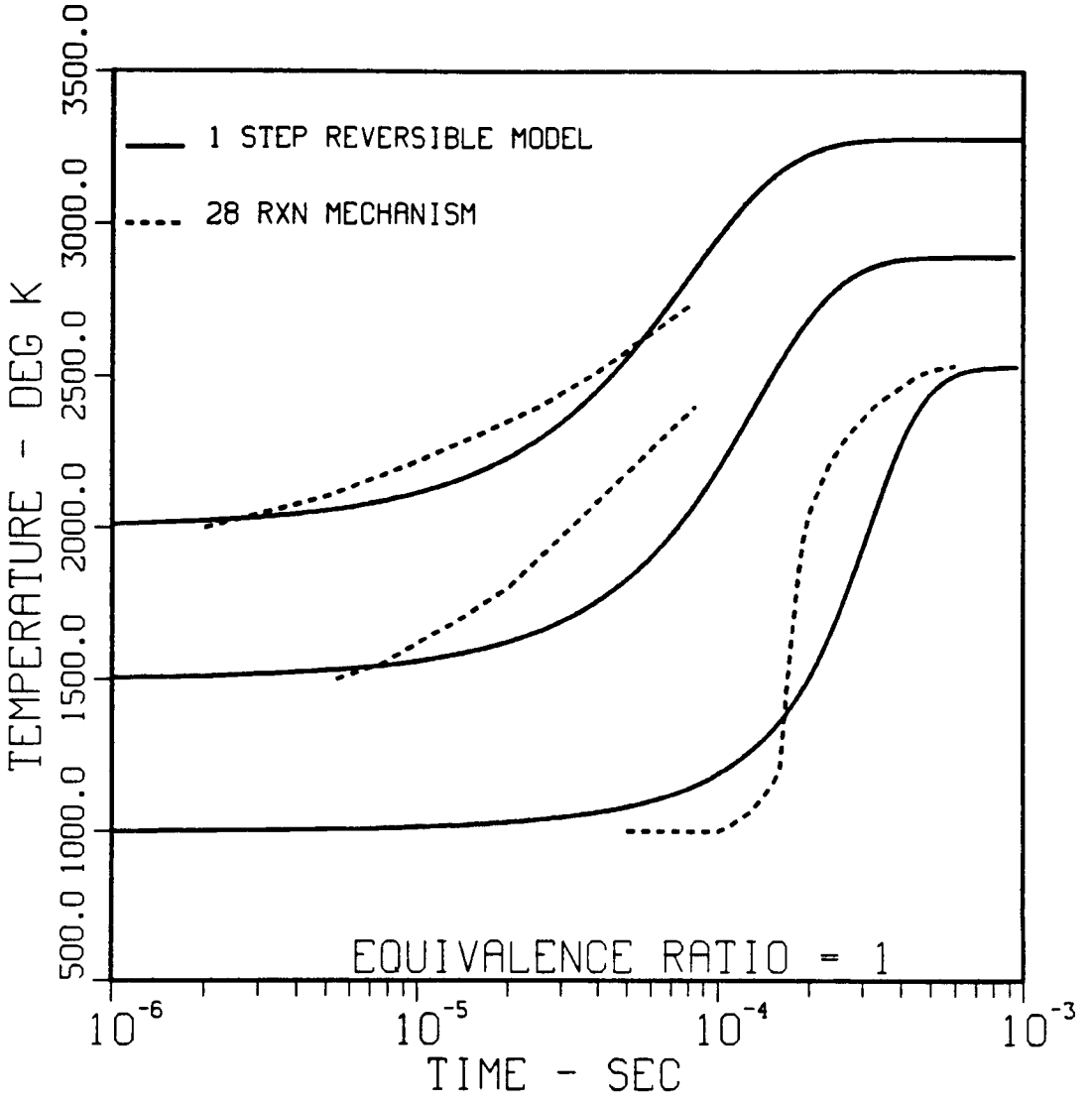

Fig. 6 Comparison of temperature histories for H2-air combustion at 1 atm.

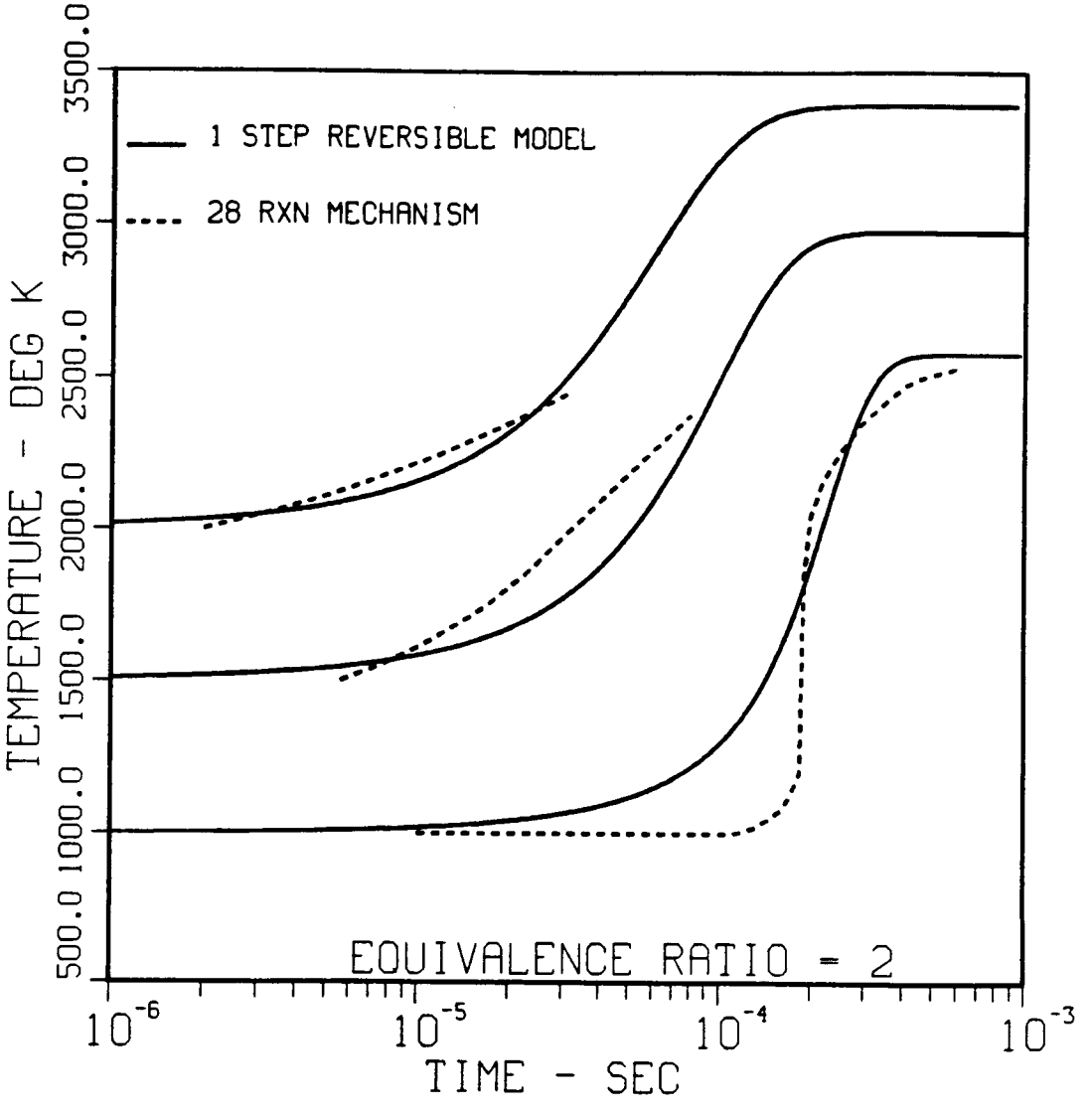

Fig. 7 Comparison of temperature histories for H2-air combustion at 1 atm.

CODE VERIFICATION

A Confined Swirling Coaxial Jet

The ASI unit of the SSME FPB is a confined, small injector and combustion chamber. It initiates ignition of propellants in the suddenly expanded FPB combustion chamber. The injector has a single pair of impinging oxidizer orifices and eight hydrogen orifices directed tangentially around the oxidizer. The tangential motion of the hydrogen flow makes the igniter flow a confined suddenly expanded swirling jet. Roback and Johnson (ref. 30) have accumulated extensive experimental data for swirling turbulent flows in confined suddenly expanded coaxial jets. Their experiment is therefore chosen for validation of FDNS2DR with respect to a confined swirling jet.

Experiment

Roback and Johnson (ref. 30) documented the flowfields for the configuration as shown in Fig. 8. Experimentally, the swirling flow channel consisted of two coaxial inlet pipes with the swirling guide vanes installed between the inner and outer pipes. The inner and outer pipes had radius of 12.5 mm and 29.5 mm respectively. The inlet channel was followed by a sudden pipe expansion with expansion ratio at about 1:2. The radius of the downstream pipe, R_o, was 61mm. The flow chosen for documentation has Reynolds numbers of 15,900 and 47,500 for the inner and annular streams respectively. These values are within the turbulent flow range and are typical of gas turbine combustors. For these experiments, water was the working fluid. The use of water limits the simulation in that it eliminates combustion and multiple species as variables to be considered. In this study, this experiment was only used to justify the ability of FDNS2DR to compute swirl. Multiple species mixing and combustion were evaluated with the dump combustor experiment. Flow condition 1 of the documentation was chosen for the code evaluation.

Results and Discussion

In order to avoid geometrical and flow complexities upstream of the expansion plane, where a three-dimensional flow field was expected and detailed experimental data were not available, the present computation employed the first data plane, which is 5 mm downstream of the expansion, as the inlet boundary where detailed experimental data were provided (ref. 30). A grid size of 61x41 was used for this test case. The grid layout is shown in Fig. 9. The exit boundary was located 1800 mm downstream of the

expansion. Notice the ratio of length to height of the grid layout in Fig. 9 was not plotted to the actual scale. The grid points were clustered near the inlet boundary where rapid flow development was expected.

The inlet swirling velocity generated by the swirling guide vane created a central recirculation zone along the pipe center line downstream of the expansion plane. This central recirculation zone was accompanied by a corner recirculation region downstream of the step. Comparisons of the development of the center line velocity are given in Fig. 10. The extended k-ε model predicted much better results than that of the standard k-ε model. Figs. 11 and 12 show the comparison of mean axial velocity and the mean azimuthal velocity at various axial stations, respectively. The extended k-ε model predictions again performed better than those of the standard k-ε model. The ability to predict the low wave number turbulence is believed to be the reason why the extended k-ε model outperform the standard k-ε model.

30 DEG MEAN ANGLE SWIRLER IN ANNULAR INLET DUCT

DIMENSION	R_{i1}	R_{i2}	R_s	R_o	S	L
LENGTH (mm)	12 5	15 3	29 5	61 0	51	1016
LENGTH (in)	0 492	0 601	1 162	2 402	2 0	40
RADIUS RATIO r/R_o	0 205	0 251	0 484	1 0	–	–

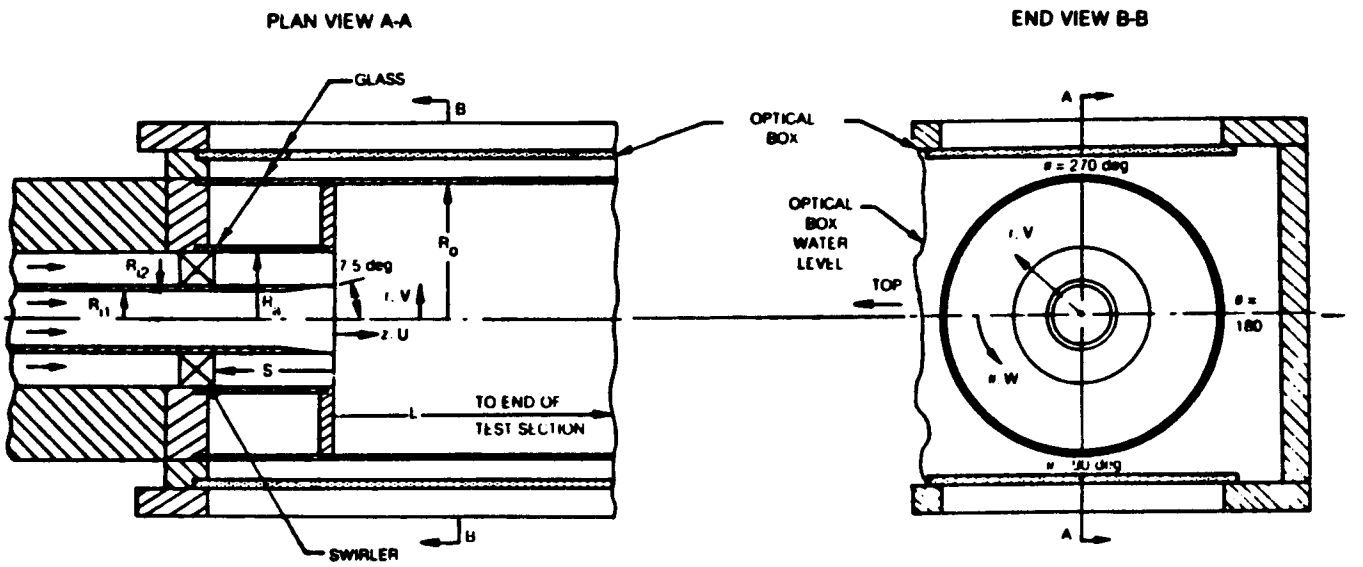

Fig. 8 Sketches of confined swirling coaxial jets test section inlet region with velocity and coordinate system.

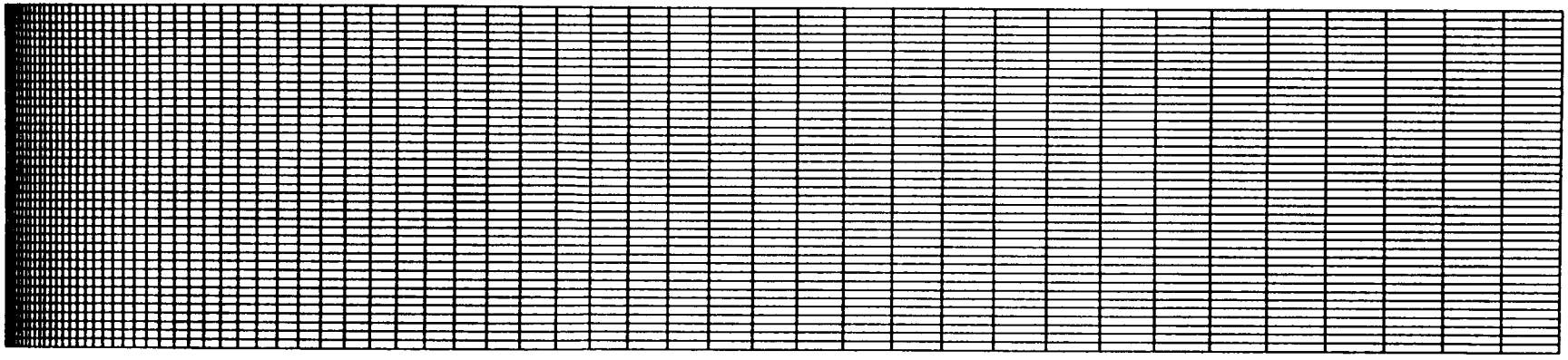

Fig. 9 Finite difference grid used to compute confined swirling coaxial jets flowfield.

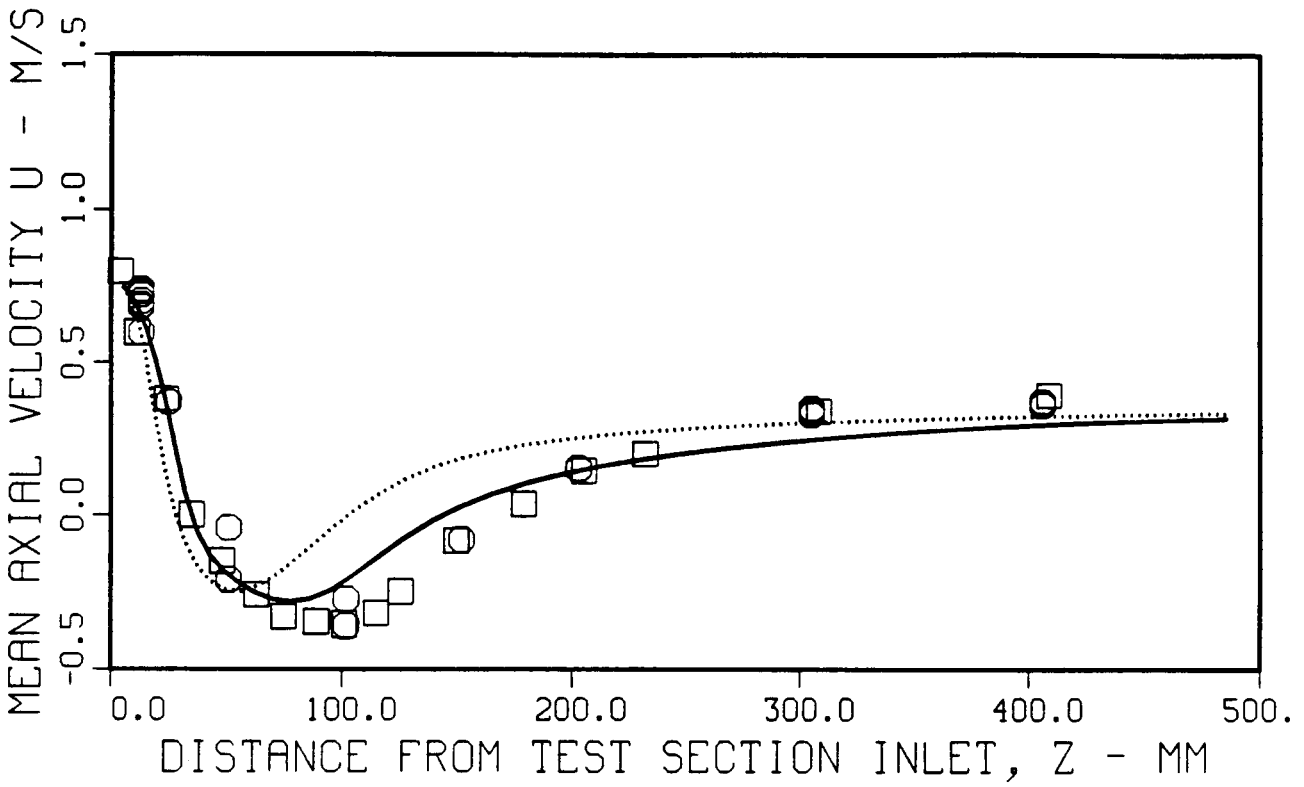

Fig. 10 Comparison of mean axial velocity along test section centerline. symbols, experiment; solid line, k-ε{T} model; dotted line, standard k-ε model.

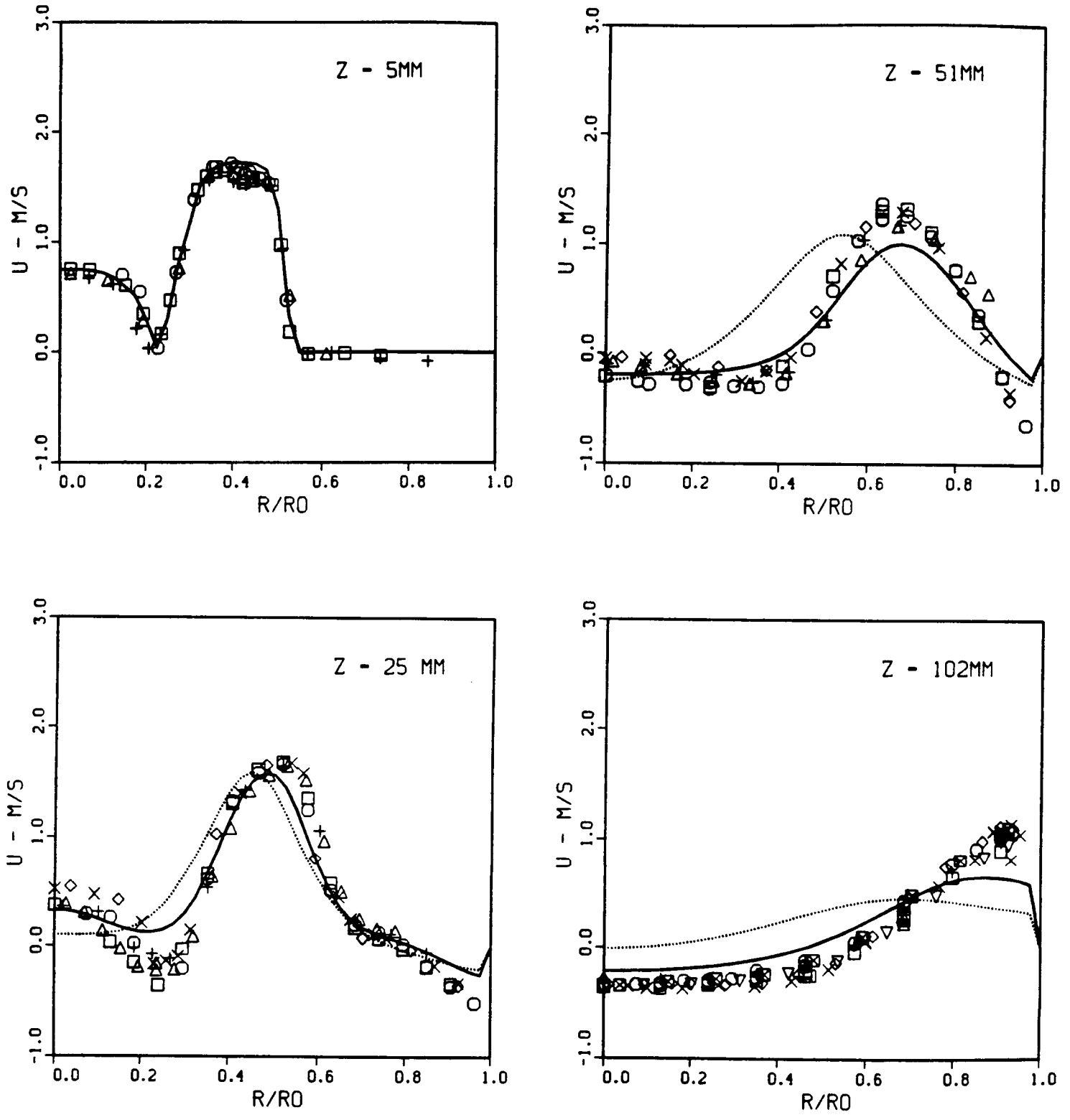

Fig. 11 Comparison of radial distribution of mean axial velocity profiles. symbols, experiment; solid line, k-ε{T} model; dotted line, standard k-ε model.

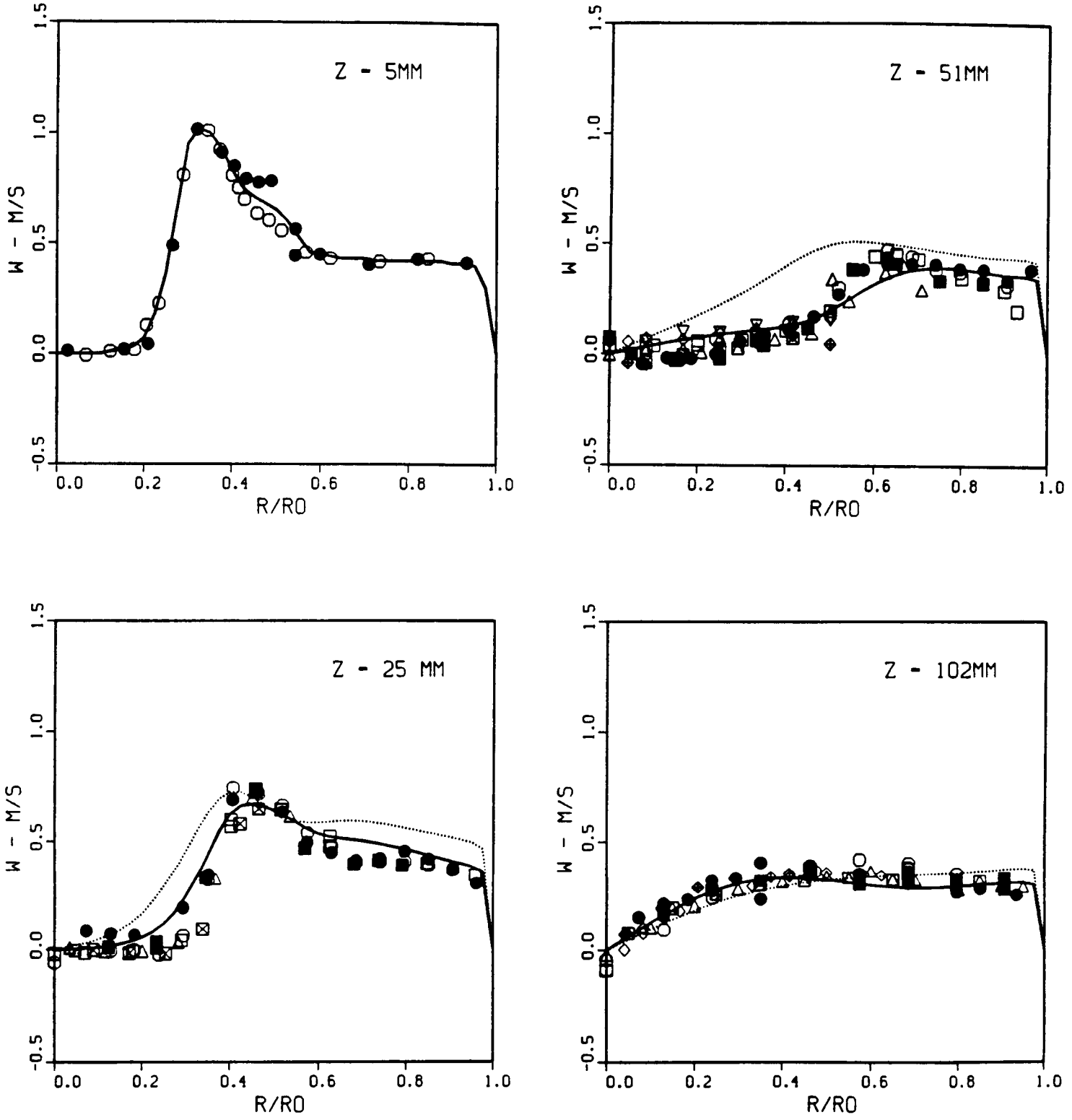

Fig. 12 Comparison of radial distribution of mean azimuthal velocity profiles. symbols, experiment; solid line, k-ε{T} model; dotted line, standard k-ε model.

A Non-reactive Hydrogen/Air Ramjet Dump Combustor

The ability to accurately predict the multiple species mixing and finite rate combustion of FDNS2DR are demonstrated in two test cases: a non-reactive hydrogen/air ramjet dump combustor, and a reactive hydrogen/air ramjet dump combustor. A tremendous effort has been devoted to the development of improved numerical techniques for design and analyzing such systems in recent years. This is mainly due to the increased demand for higher performance and the tighter system size and weight constraints on future propulsion and combustion systems in general, and of the National Aerospace Plane in particular. A critical requirement in achieving the future demand is the ability to accurately describe the combustor flowfield for varied design parameters. Unfortunately, the physical phenomena occurring in a ramjet dump combustor are quite complex and present quite a task for numerical tools and computer resources. It is for this reason that modular models (refs. 31 and 32) were first used to predict ramjet combustor flowfields. Such models assumed that the entire flowfield can be broken down into several neat elements: the recirculation zone, the core region, the shear layer and the mixing region. The recirculation zone can then be represented by a perfectly stirred reactor to stabilize the flame, and the central core can be described by parabolic equations. These two regions can then be joined by a shear layer model and the parabolic mixing model to complete the calculation. The modular model has obviously utilized assumptions regarding the structure of the flowfield, e.g., the size of the recirculation region. It will be shown later in this study, that the recirculation length might vary by a factor of two, depending on whether the flow is reactive or non-reactive. Nevertheless, the modular approach is a computational simple and physically sound model which is useful in initial parametric analyses.

More complete models that recognize the spatially elliptic nature of ramjet dump combustor flowfields require the solution of the full Navier-Stokes equations. These models describe the entire dump combustor flowfield without resorting to the modular components. An excellent pioneering work was reported by Drummond (ref. 33), his analysis of the dump combustor flowfield included the solution of the spatially elliptic and temporally parabolic form of the governing equations. An unsplit MacCormack finite difference scheme (ref. 34) was used to integrate the system equations with time stepping. An algebraic eddy-viscosity model was used for the turbulence, and a decoupled, instantaneous reaction was utilized for the chemical reaction. The results from that study predicted the flowfield to be somewhat more diffusive than observed in the experiments. Drummond concluded that the overprediction of the mixing rate and large diffusion were caused by the turbulence model. Trinh (ref. 35) has performed a similar analysis on a non-reactive dump combustor

simulation. A standard two-equation k-ε turbulence model (ref. 18) and a staggered grid finite difference solver (ref. 19) were used to perform the calculation. Improved mixing rates and recirculation region size were obtained with the more sophisticated k-ε turbulence model, but the reacting cases were not analyzed.

Experiment

A ramjet dump combustor simulation experiment was carried out at the Arnold Engineering Development Center (ref. 36). The dump combustor simulation facility is shown in Fig. 13. Air was injected from the inner 2.07 in. diameter pipe at a mass flow rate of 0.58 lbm/sec. The inner air nozzle was surrounded by a 5.24 in. diameter outer pipe from which gaseous hydrogen was injected at a mass flow rate of 0.002 lbm/sec. The one-dimensional velocity of the primary and secondary stream was 335 ft/sec and 3 ft/sec, respectively and the inlet temperatures were nominally 525 deg. R. for the nonreactive case and 1300 deg. R. for the reactive case. The nominal static pressure in the exhaust duct was 13.7 psia. Measurements were made at axial stations from zero to six duct diameters from the primary nozzle exit plane. The diameter ratio of this configuration was 2.5.

Results of the Non-reactive Dump Combustor Calculation

The analysis of the non-reacting dump combustor flowfield was carried out in a physical domain, beginning one half outer pipe diameter upstream of the step and concluding six diameters downstream of the step. The central primary flow was air, and the secondary flow coming out of the step was hydrogen. Fig. 14 shows the final computational grid (60x31) selected from a series of grid dependency tests. The grid lines were clustered near the wall and the corner of the step to resolve the boundary layers. The predicted non-reacting dump combustor steady state vector field is shown in Fig. 15. Notice the recirculation region downstream of the secondary flow step. The convergence history is given in Fig. 16. Approximate convergence was obtained after the original value of the residual had dropped four orders of magnitude. It took 525 CPU seconds and 1066 iterations for a typical k-ε{T} turbulence model calculation on a CRAY XMP computer. The secondary flow velocities were estimated for this simulation, since negative velocities were reported (ref. 36). Estimates were based on the overall secondary mass flow rates. This was also the case for the reactive flow calculation.

Fig. 17 shows the comparison of the experimental and the computed centerline velocities. The temperature dependency of the k-ε{T} model was negligible on the non-reacting case since the flow was at room temperature. It therefore behaves like the extended k-ε turbulence model. Both turbulence models predicted

ORIGINAL PAGE
BLACK AND WHITE PHOTOGRAPH

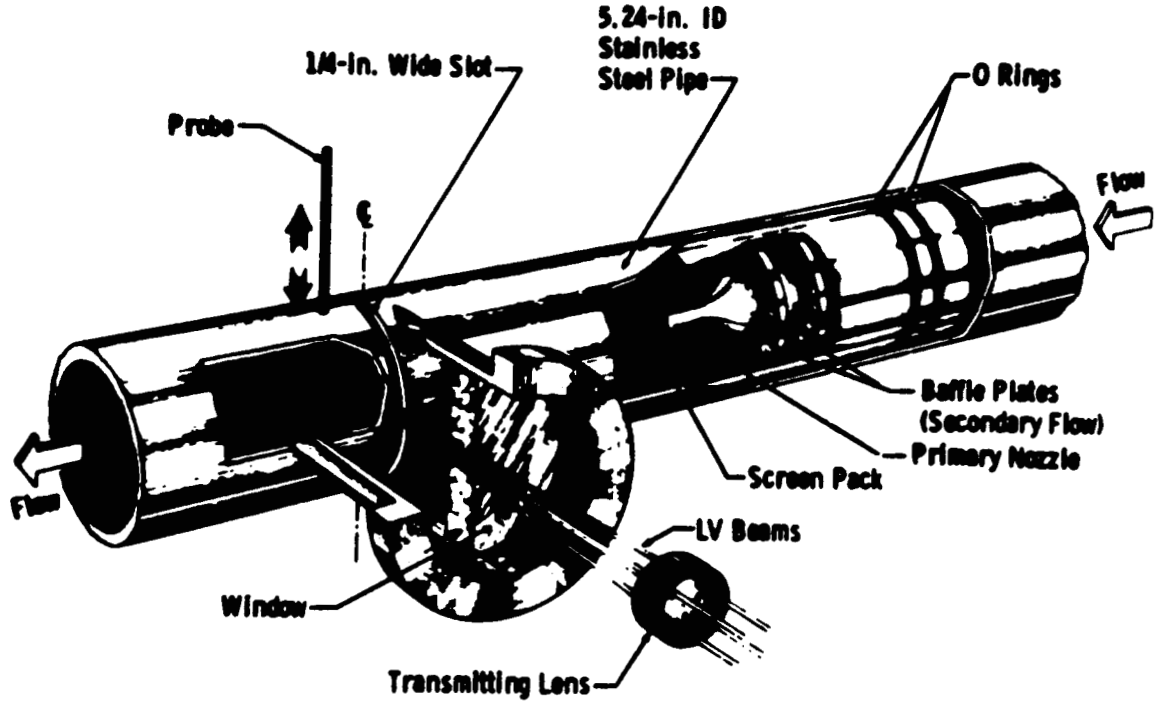

Fig. 13 AEDC dump combustor simulation facility.

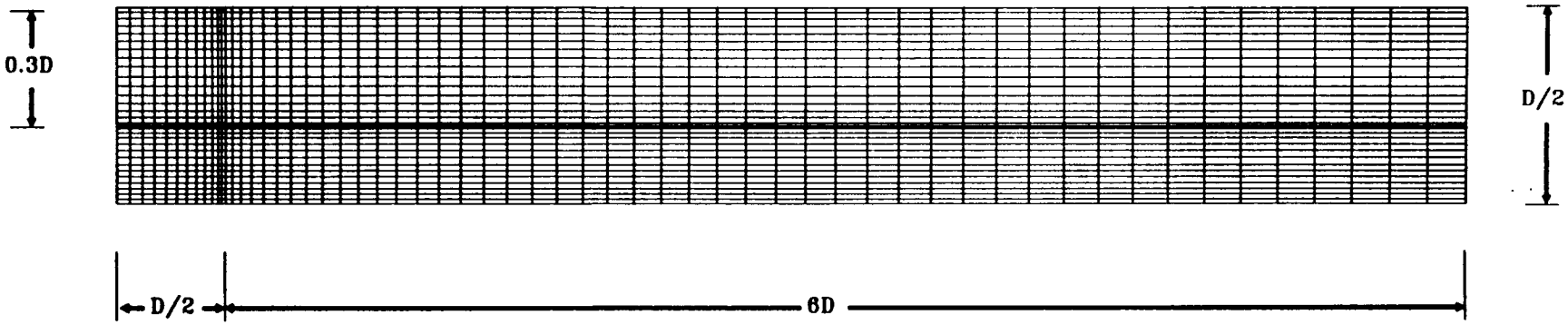

Fig. 14 Finite difference grid used to compute dump combustor flowfield.

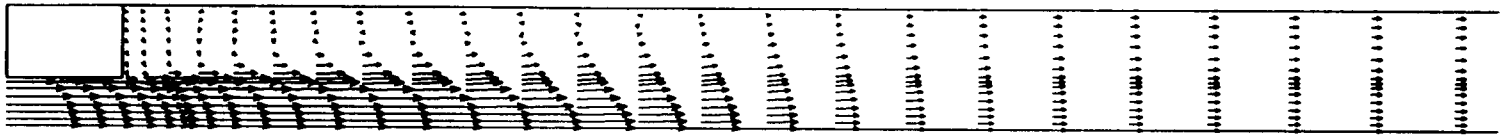

Fig. 15 Computed steady-state velocity vector field in non-reacting dump combustor simulator.

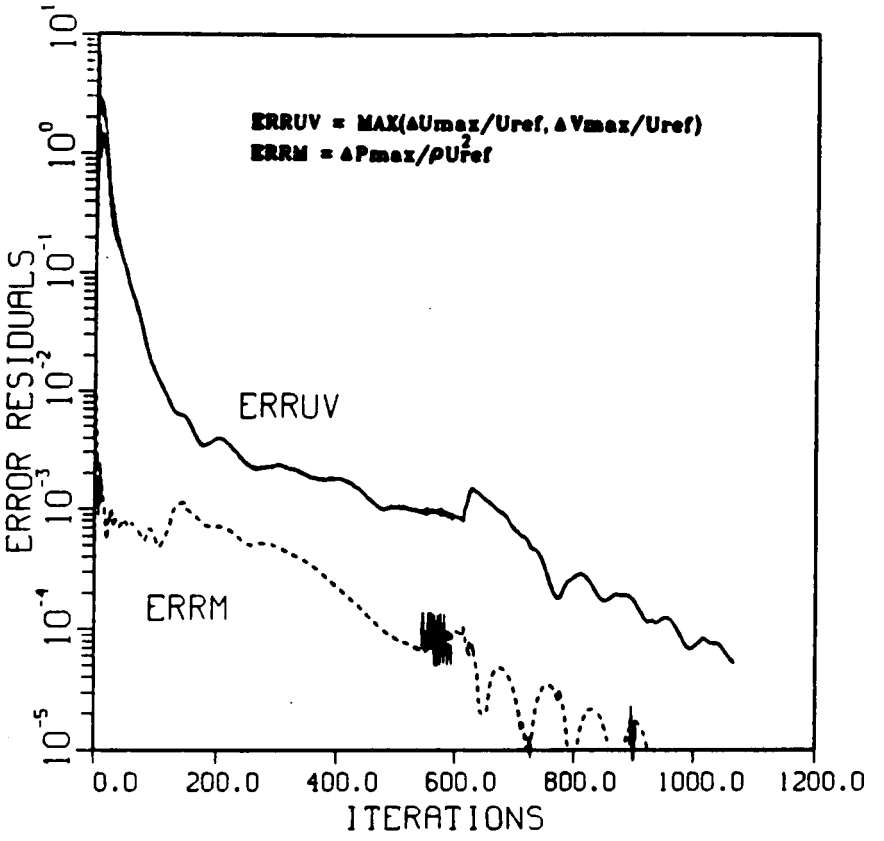

Fig. 16 Convergence history for the non-reacting dump combustor calculation.

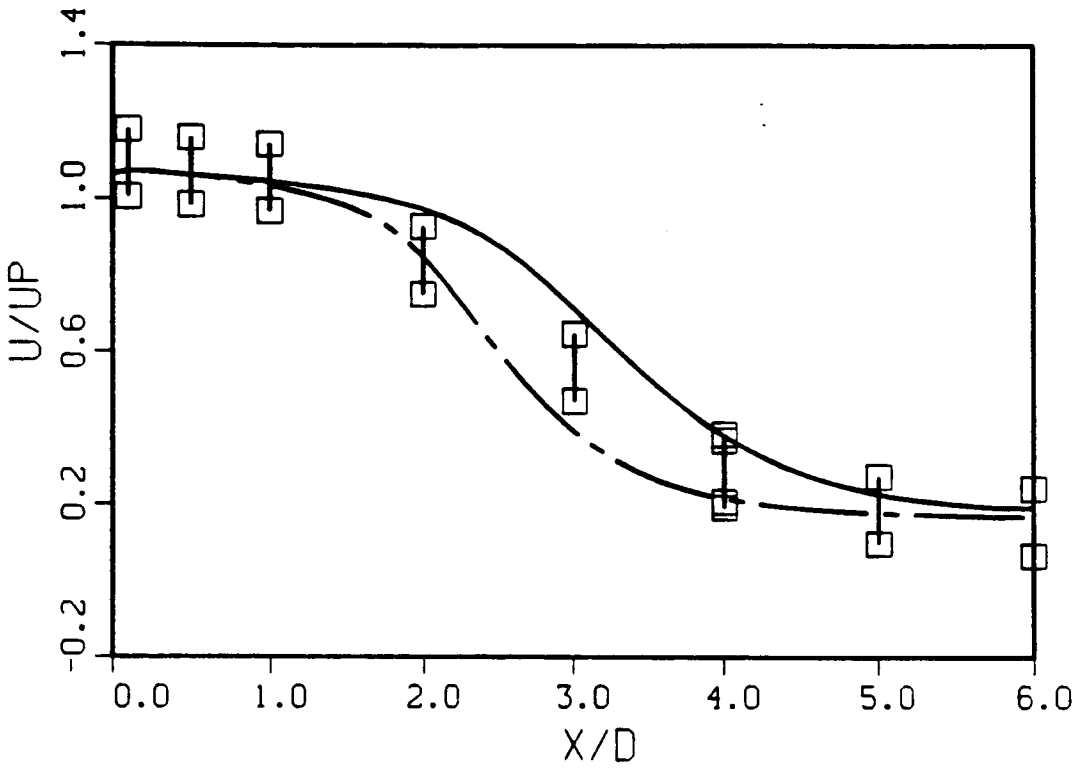

Fig. 17 Comparison of computed and experimental centerline velocities. □ , experiment; solid line, k−ϵ{T} model; dashed line, standard k−ϵ model.

the centerline velocities well in the initial region (X/D=0 to X/D=1) and the final region (X/D=5 to X/D=6). Near the measured reattachment point (X/D=3), the standard k-ε model underpredicted the velocity and the k-ε(T) model overpredicted the velocity. The measured reattachment length for the non-reactive dump combustor corresponds to a step height of 9.9 at an expansion ratio of 2:5. While Chaturvedi's (ref. 37) pipe expansion experiment has measured a 9.2 step heights for an expansion ratio of 1:2. The standard k-ε turbulence predicted a shorter reattachment length at 8.32 step heights, and the k-ε(T) turbulence model predicted a longer reattachment length at 10.7 step heights in this study. The longer measured reattachment length for the non-reactive dump combustor is certainly reasonable for a larger expansion ratio, in comparison to Chaturvedi's measurement. In general, predictions made by both models were within the error bounds of the experimental data.

Fig. 18 gives the comparison of the axial distributions of wall static pressures. The predictions agreed well with the experimental data at both ends. From X/D=1 to X/D=4, the standard k-ε model overpredicted the pressure and the k-ε(T) model underpredicted the pressure.

Fig. 19 gives the comparison of the axial distribution of hydrogen mass fraction along the wall. Both turbulence models predicted complete mixing after four diameters downstream. The experiment and prediction agreed reasonably well beyond one diameter downstream. The suddenly drop of the hydrogen mass fraction near about 0.5 diameter downstream is believed to have caused by the formation of the recirculation zone.

A comparison of the radial distribution of mean axial velocity at several axial stations downstream of the step is given in Fig. 20. Both turbulence models predicted good results in comparison with the experimental data. The predicted reattachment point was about three diameters downstream of the step that matched the experimental data. Comparison of the computed and experimental radial profile of hydrogen mass fraction are shown in Fig. 21. The predictions agreed well with the data. Although there was a small difference of about 0.001 between the predicted values and the experimental values at the last station. The predicted values are well within the error bound of the experiment.

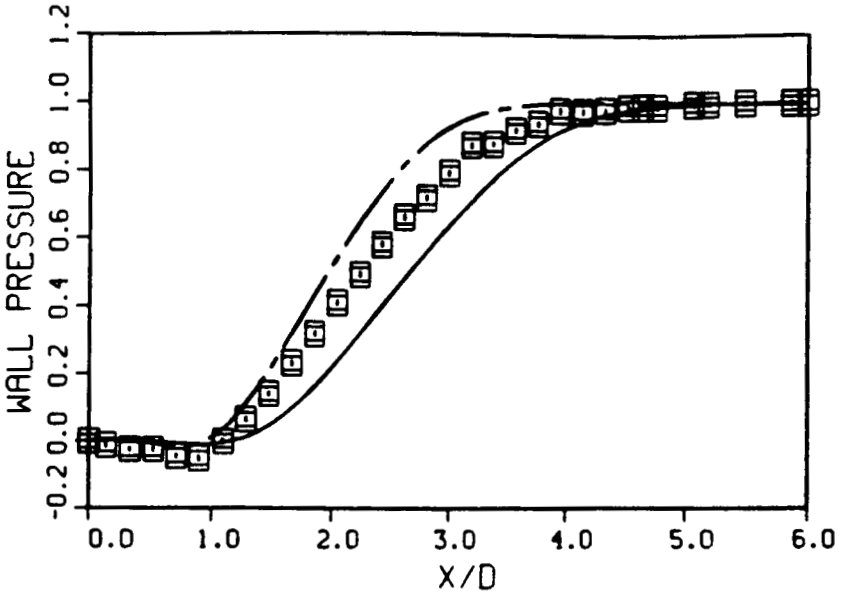

Fig. 18 Axial distribution of wall static pressure. ◻, experiment; solid line, k−ε{T} model; dashed line, standard k−ε model.

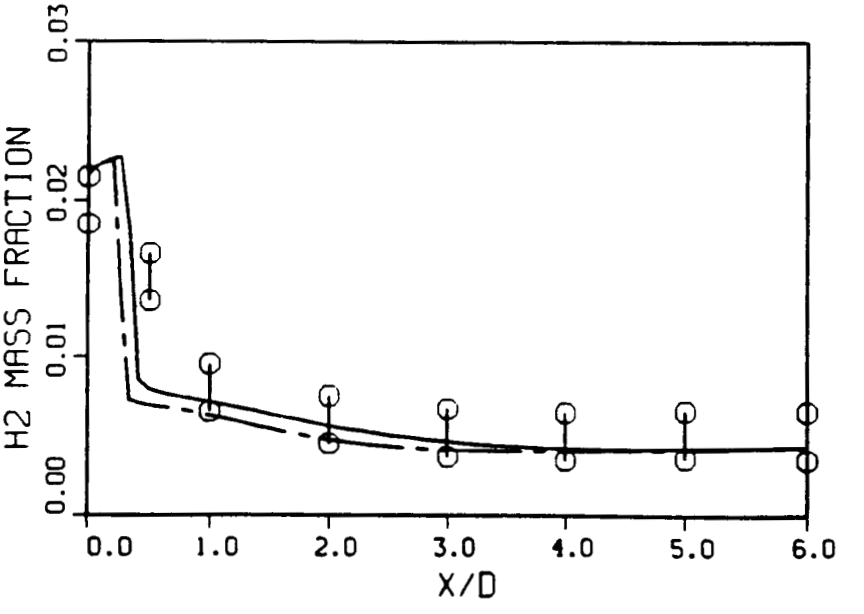

Fig. 19 Axial decay of hydrogen mass fraction at wall. ○, experiment; solid line, k−ε{T} model; dashed line, standard k−ε model.

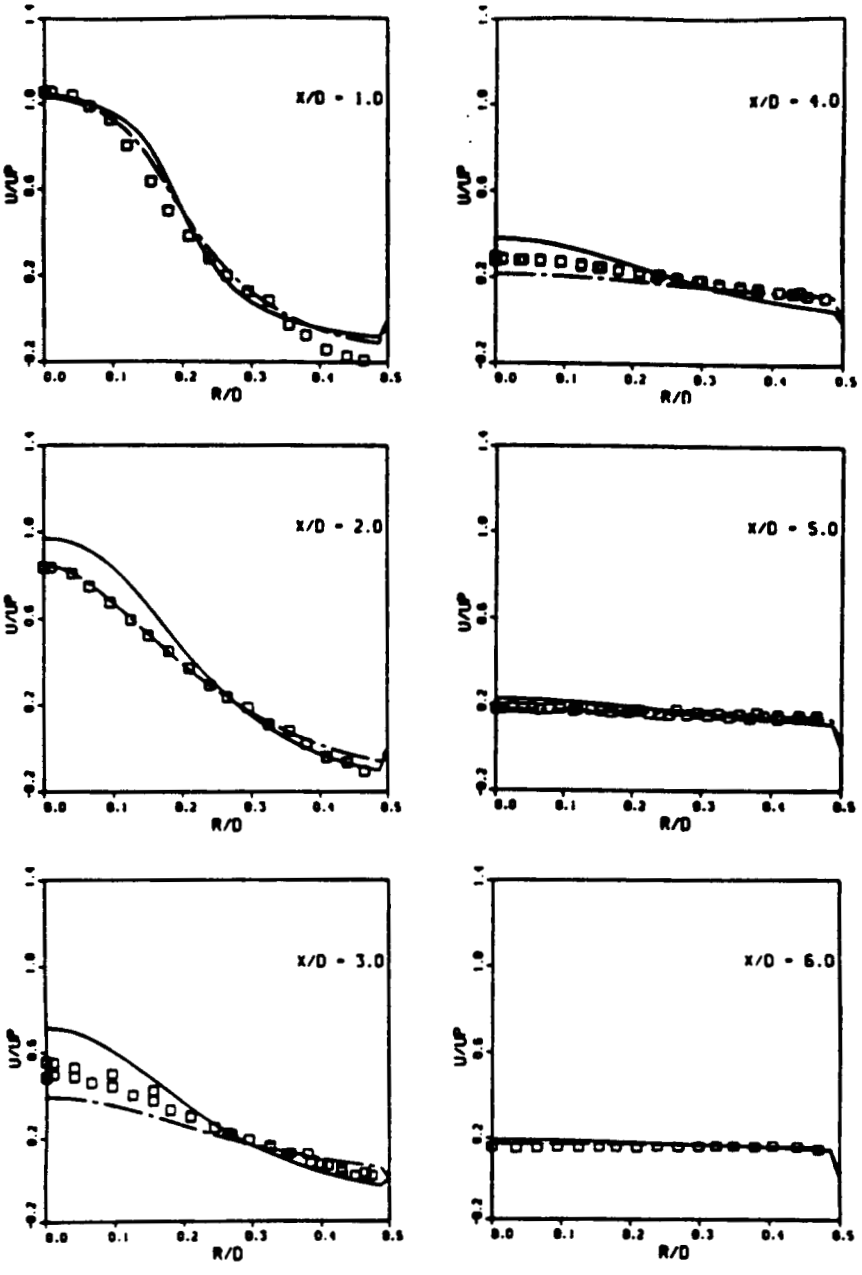

Fig. 20 Radial distribution of mean axial velocity. □, experiment; solid line, k−ϵ{T} model; dashed line, standard k−ϵ model.

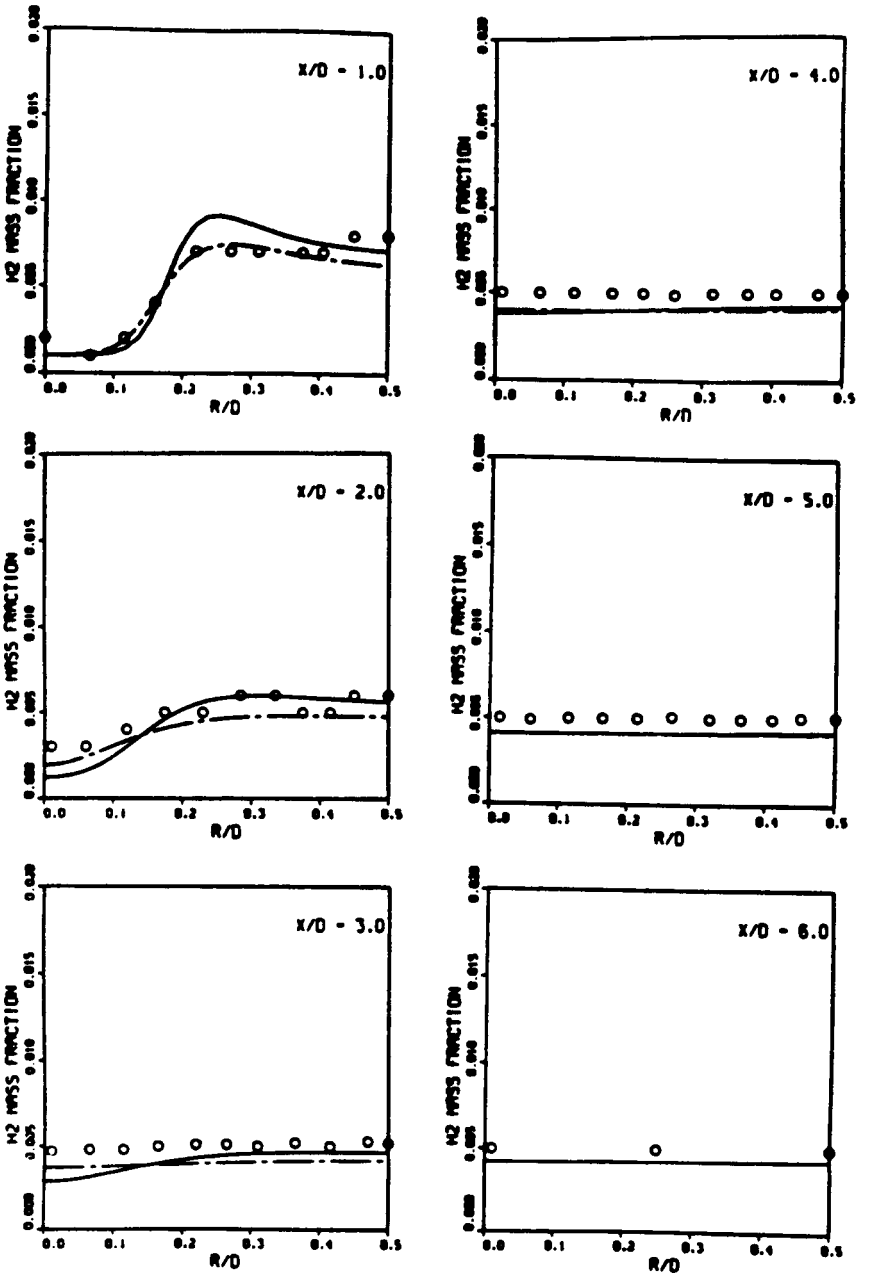

Fig. 21 Radial distribution of hydrogen mass fraction. o, experiment; solid line, k−ϵ{T} model; dashed line, standard k−ϵ model.

A Reactive Hydrogen/Air Ramjet Dump Combustor

Results of the Reactive Dump Combustor Calculation

The experimental results of the reactive dump combustor have shown a longer recirculation zone due to the heat release of the exothermic chemical reaction. The computational domain of the reactive dump combustor calculation was therefore extended to eight diameters downstream of the step so that the longer recirculation zone could be properly contained. The typical grid size used was 70x31. A grid size of 105x31 to include fifteen diameters downstream of the step was also computed, but the results showed little or no difference with the 70x31 case.

Fig. 22 shows the comparison of computed and experimental centerline velocities for the reactive dump combustor calculation. The k-ε{T} prediction gives excellent comparison with the data. It was used exclusively for latter comparisons. The predictions with the standard k-ε and the extended k-ε turbulence models showed too rapid a mixing rate without considering the temperature effect. The effect of the k-ε{T} turbulence was to reduce the turbulent eddy viscosity. Fig. 23 gives the comparison of axial wall static pressures. The prediction and the experimental data are in good agreement.

The comparison of experimental and computed radial distributions of mean axial velocity are shown in Fig. 24. The computed values are in good agreement with the experimental data. The reattachment length predicted was a little less than six diameters after the step and matched the reported data. In comparison, Drummond's predictions showed no reversed axial velocity at any the axial stations. The k-ε{T} turbulence is obviously a better representation for the chemically reacting, recirculating flow calculation. Fig. 25 gives the comparison of the computed and experimental radial temperature profiles. Excellent agreement was obtained between the predicted values and the experimental data at all stations. The predicted flame front was located approximately between X/D=1 and X/D=2. The heat release of the reaction was therefore properly represented by the one-step reversible chemical kinetics model. In comparison, Drummond's predictions show an early radial temperature rise and then a drop of temperature as it approaches the wall at X/D=1, and the wall temperatures were consistently lower than the experimental value for the rest of the stations. This was probably caused by a combined effect of the chemistry and turbulence models. The complete combustion chemistry forced a flame front very close to the step, and the algebraic turbulence model produced fast mixing that did not allow enough unreacted fuel to remain near the wall. The predicted hydrogen mass fraction profiles were in reasonable agreement with measured data. The required CPU time for the reactive dump combustor calculation was approximately three times longer than that of the

non-reactive dump combustor calculation. The convergence criterion was relaxed to three orders of magnitude decrease in the residuals since further integration did not improve the results.

In comparison of the non-reactive and the reactive cases, both the experiments and the predictions indicated that the heat release of the chemical reaction have reduced the effective eddy viscosity and increased the length of the recirculation length for the dump combustor configurations.

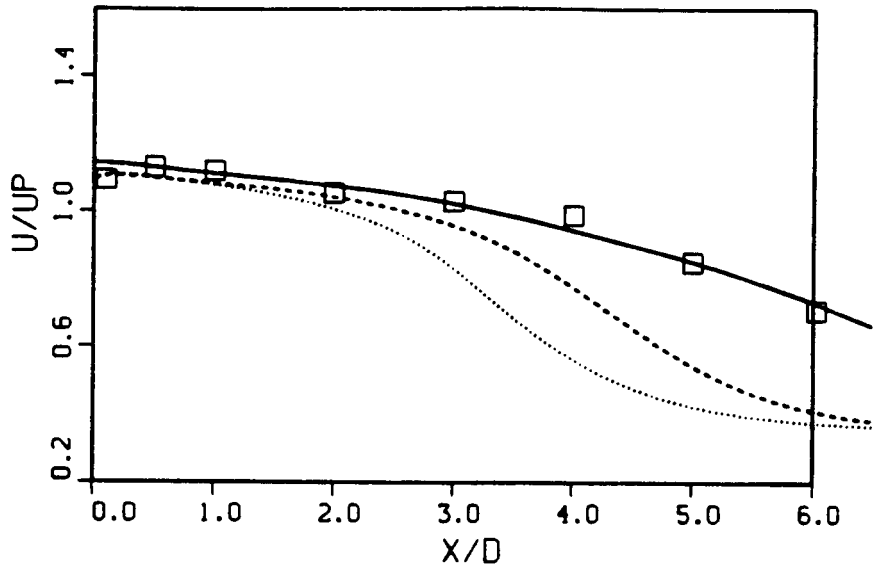

Fig. 22 Comparison of computed and experimental centerline velocities. □, experiment; solid line, k−ε{T} model; dashed line, extended k−ε model; dotted line, standard k−ε model.

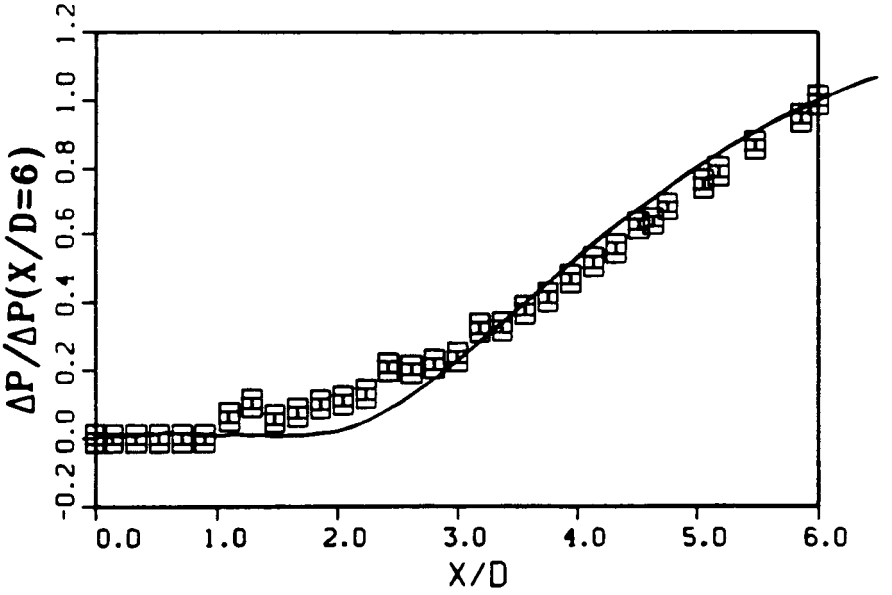

Fig. 23 Axial distribution of wall static pressure. □, experiment; solid line, k−ε{T} model.

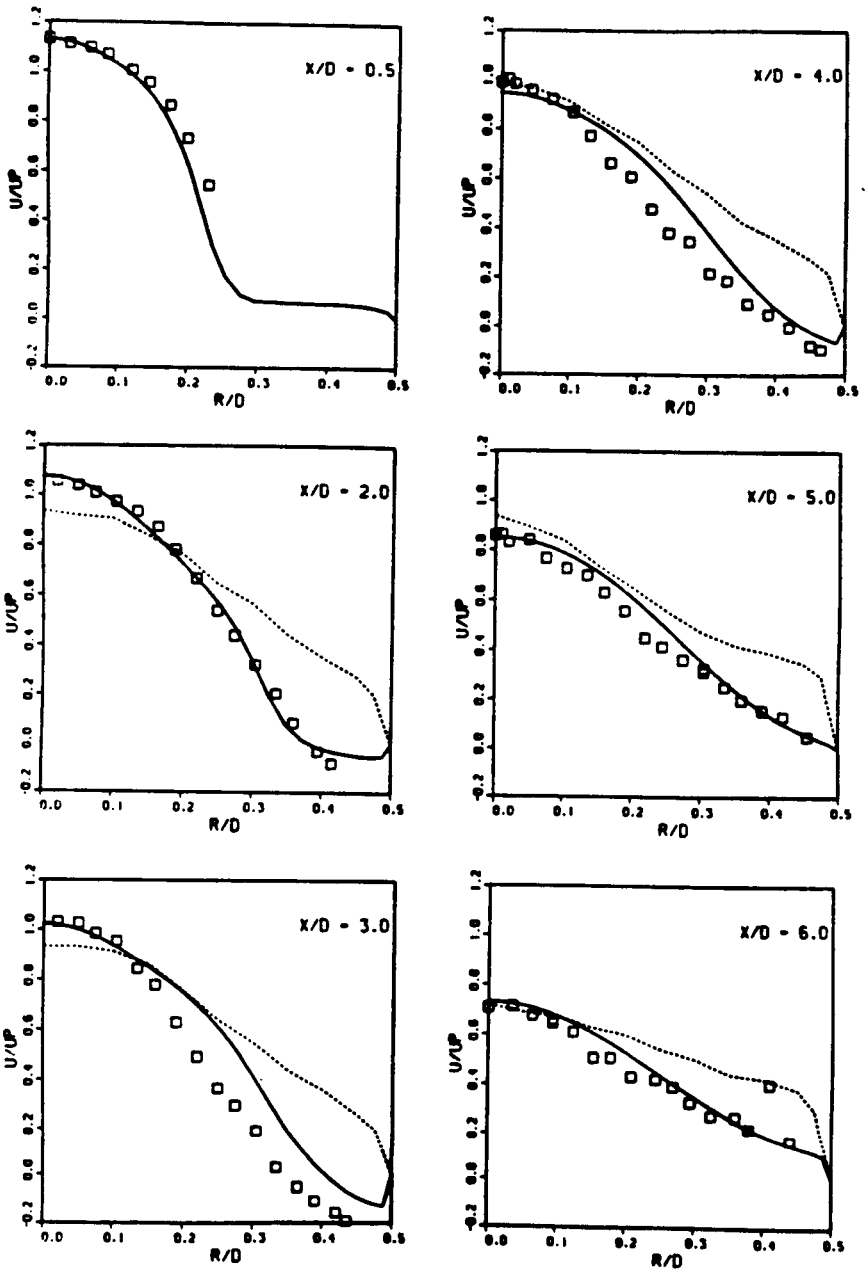

Fig. 24 Radial distribution of mean axial velocity for reactive dump combustor. □, experiment; solid line, k−ϵ{T} model; dashed line, Drummond's calculation.

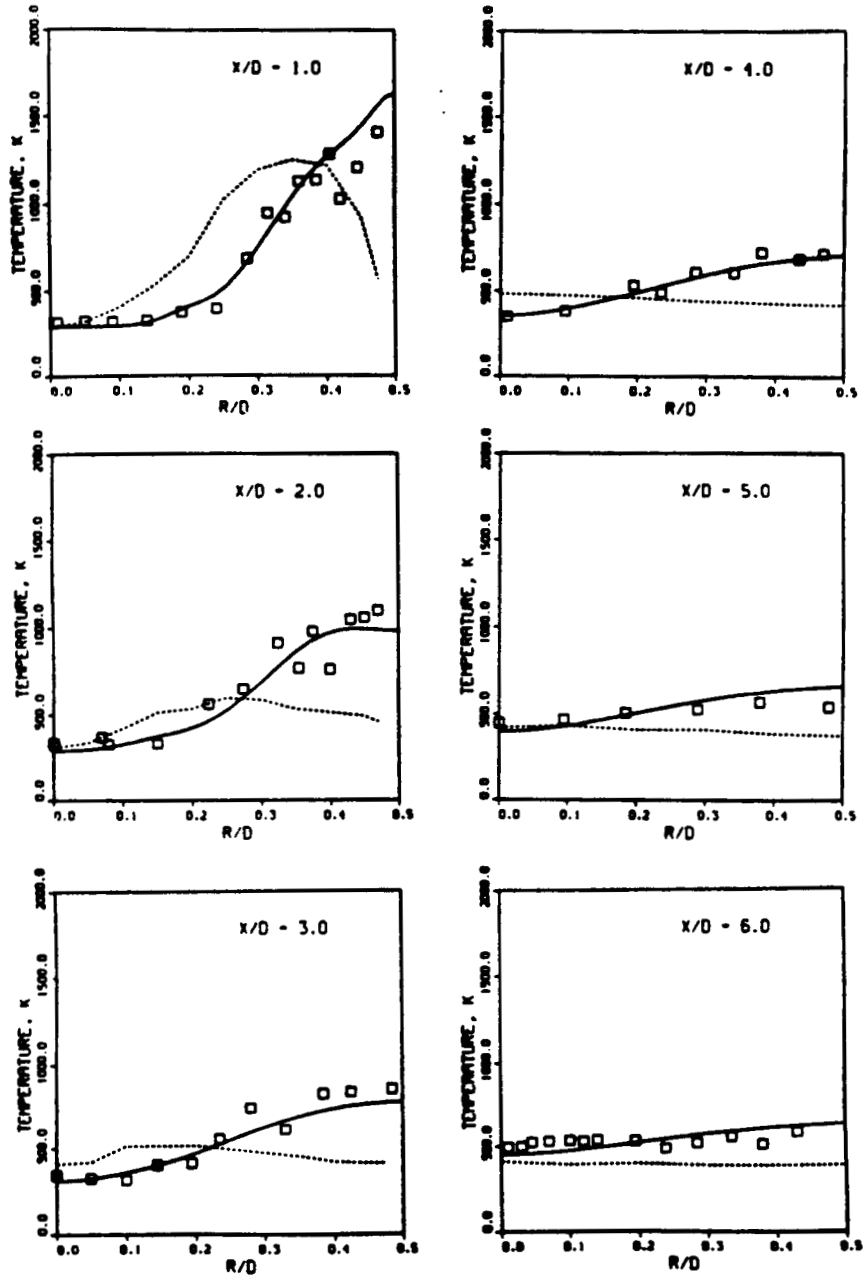

Fig. 25 Radial distribution of mean static temperature. □, experiment; solid line, k−ϵ{T} model; dashed line, Drummond's calculation.

TRANSIENT FUEL PREBURNER SIMULATION

Transient Upstream Boundary Conditions

At the start command, the initial flowfield of the fuel preburner is filled with atmospheric nitrogen purge gas as described by ref. 38. After the start command, the fuel and oxidizer flow out of the augmented spark igniter (ASI) and the injector elements on the faceplate, to prime the chamber and the turbine. The transient upstream boundary conditions therefore include the ASI and injector fuel and oxidizer mass flow rates, and the chamber pressure. These transient flow properties were obtained from Digital Transient Model (ref. 39) simulation (ref. 8). They are written as:

$$\begin{aligned} P_c &= P_c(t) \\ W_{ASI,i} &= W_{ASI,i}(t) \\ W_{INJ,i} &= W_{INJ,i}(t) \end{aligned} \tag{31}$$

where subscript i represents either fuel(f) or oxidizer(o). The species mass fractions at the inlet boundary are given by

$$\alpha_i = W_i/\Sigma W_j \tag{32}$$

and the total mass flow rate at the inlet is

$$W_T = \Sigma W_i \tag{33}$$

The operational pressure variable p in FDNS2DR is the difference between the actual pressure and the pressure at a reference point. When the reference point is placed at the inlet boundary and the reference pressure is varied with the transient chamber pressure, the actual pressure in the whole flowfield will respond instantaneously to the transient chamber pressure and to the solution of the conservation equations. The density at the inlet boundary is then calculated as:

$$\rho' = (p + p_c)/(\Sigma \alpha_i/M_i\ RT) \tag{34}$$

while the velocities at the inlet are updated by

$$u' = uW_T/\int \rho' u dS$$

and

$$v' = 0 \tag{35}$$

Fig. 26-28 show the DTM simulated transient flow properties for a nominal operation at an elapsed time of one second. The engine main fuel valve begins to ramp open at the start command, and the FPB oxidizer valve begins to open at 0.1 seconds (ref. 3). The ASI flow rates are shown in Fig. 26. The fuel flow did

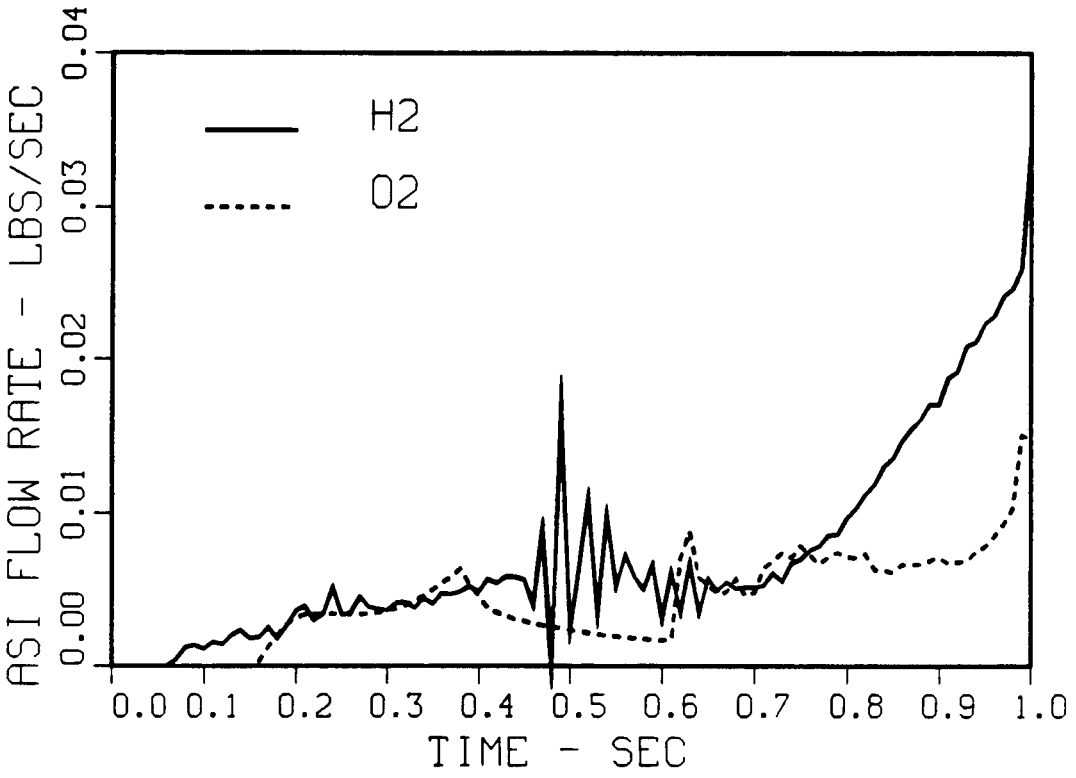

Fig. 26 Transient fuel preburner ASI inlet mass flow rate boundary conditions.

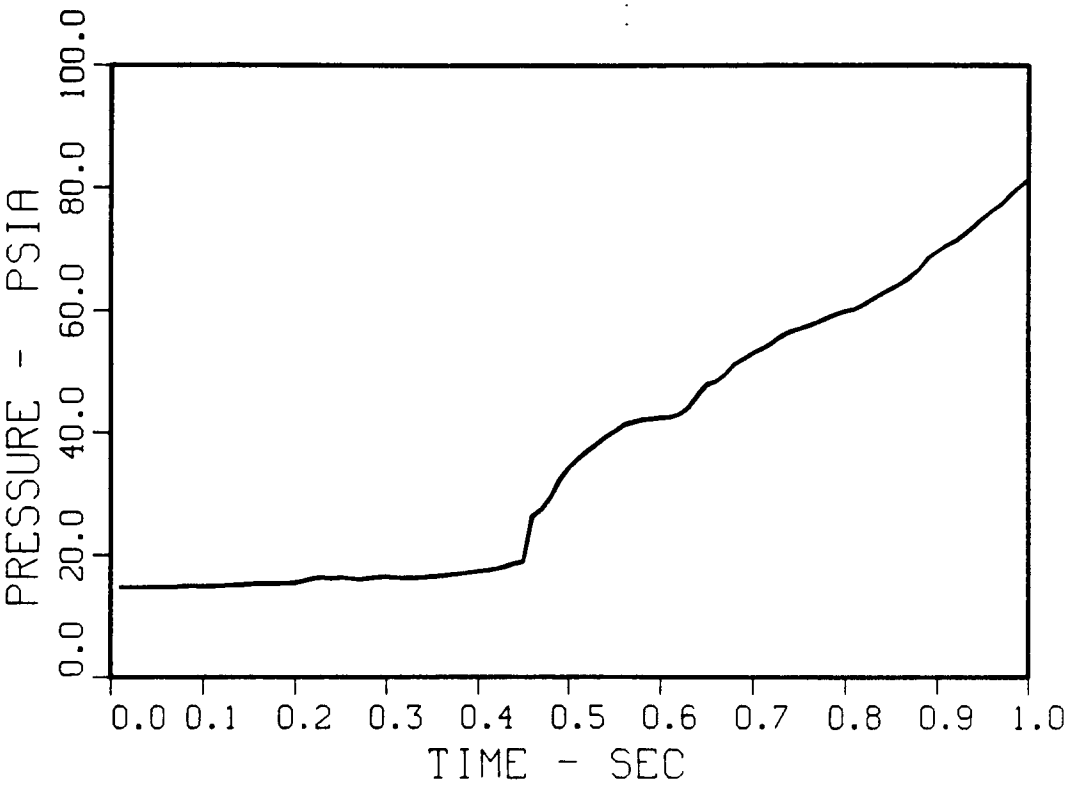

Fig. 27 Transient fuel preburner chamber pressure boundary condition.

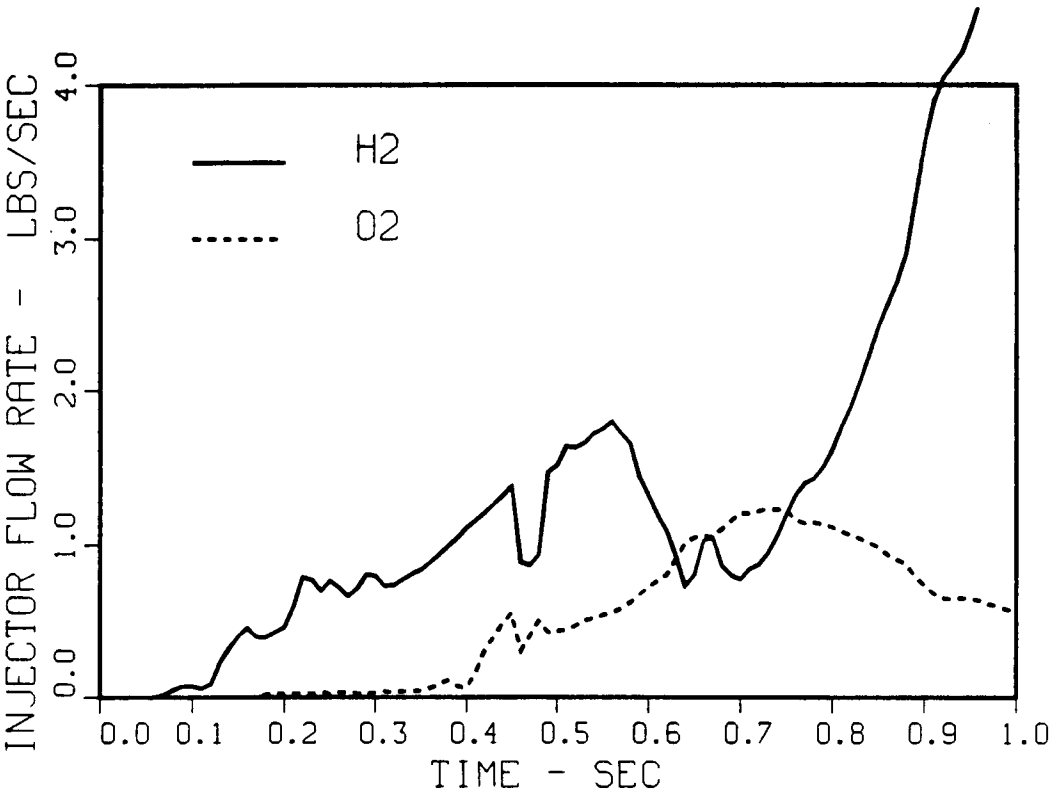

Fig. 28 Transient fuel preburner injector mass flow rate boundary conditions.

not emerge until 0.07 seconds and the oxidizer flow did not appear until 0.15 seconds. The oxidizer flow rate had a drop from 0.4 to 0.6 seconds, and the fuel flow rate oscillated at this time period. The chamber pressure history is given in Fig. 27. The pressure did not start to rise until 0.45 seconds. Fig. 28 shows the DTM simulated injector flow rates. There is an initial decline of fuel flow rate at around 0.45 seconds, corresponding to the time of pressure rise in Fig. 27. A major second drop of fuel flow rate occurred near 0.6 to 0.8 seconds. In the meantime, an increase of oxidizer flow rate also occurred. It can be seen that the fuel flow rates were probably designed to have a lead over the oxidizer flow rates to avoid a local lean mixture in the chamber. But the pressure wave sent from downstream of the fuel preburner due to the sudden pressure rise may have shut down the fuel supply line for a short period of time. During this period of time, the fuel flow rate dropped, and, the oxidizer flow rate increased in order to compensate for the fuel flow rate loss. The combination of the fuel flow rate drop and the oxidizer flow rate increase have caused a lean mixture. The lean mixture combustion would cause a temperature spike. The closer the mixture ratio is to the stoichiometric composition, the higher the thermal gradient will be.

Grid Definition and flow assumptions

The computational grid was constructed based on the assumption that two concentric jets can be used to represent the fuel preburner flows. The inner jet represents the ASI flow and the outer jet stands for the injector flow. Gaseous propellants were assumed to come out of the injectors on the faceplate. Many grids were designed and evaluated with the technique of quantitative measures (ref. 40) and series of steady state flow tests, so that the final computational grid can withstand the transient, swirl, reactive flow with temperature spikes. Fig. 29 shows the final computational grid for the calculation. The grid size was 68x45 and no grid related problems has occurred during the calculation.

FDNS2DR methodology was used to describe the response of an axisymmetric FPB and turbine inlet thermal flowfield to the transient start. To simulate start-up, the propellants must be ignited by the ASI system and the flame must propagate through the chamber at a realistic rate as determined by the chemical kinetics and mixedness level of the system. The upstream boundary conditions were obtained from the DTM simulation, and therefore simulate the actual opening of the FPBOV and the response of the transient combusting flow. Downstream boundary conditions at the FPB exit are extrapolated from the interior flowfield and adjusted by the transient inlet mass flow rate. This does represent an additional degree of approximation but it was found necessary to obtain a well behaved solution. Adiabatic walls were also assumed for the entire simulation.

Results of the Transient Calculation

The transient fuel preburner thermal flowfield calculation was carried out for 1.0 second. Fig. 30 - 40 show the calculated FPB thermal flowfield time histories at an interval of 0.1 seconds. Fig. 30 shows the thermal flowfield at the start command. The upper half of the preburner represents the flow vector streak lines, while the lower half gives the temperature contours. The left-hand side of the preburner indicates the inlet of the propellants. The circular area represents the top of the turbopump dome (Kaiser hat). It can be seen from the temperature contour that the hot igniter flow was coming out of the ASI chamber, and the streak lines showed a quiescent nitrogen gas filled environment. Fig. 31 shows that the igniter flow flame was swirling out of the ASI chamber and penetrated into the injector flow region, at about 0.1 seconds. The flow in the rest of the chamber was still undisturbed nitrogen purge gas. At 0.2 seconds, Fig. 32 shows the hot igniter flow was advancing farther downstream. The injector flow appeared to have gained some momentum, but was not combusted since it was mostly cold hydrogen. About half of the nitrogen purge gas was pushed out of the combustor at this moment. At 0.3 seconds, Fig. 33 shows the hot ASI flame has extended to the top of the turbopump dome. Most of the nitrogen gas was pushed out. The injector flow gained more momentum but was still cold since the injector oxidizer had just entered the chamber. Fig. 34 shows the igniter flow had covered the whole Kaiser hat and a flame front had begun to move toward the faceplate. The injector oxidizer flow rate had increased. The nitrogen concentration had dropped to a negligible amount and the species nitrogen was turned off for more efficient calculation at 0.4 seconds.

Fig. 35 shows the thermal flowfield corresponding to about 0.5 seconds after the start command. The initial decline of injector fuel supply had made the mixture ratio leaner. The flame front propagated to the faceplate. A hotter region had formed on top of the turbopump dome, and propagated toward the ASI. The flow had sped up due to the increase in flow rate and the combustion. Notice a centerline recirculation zone was being formed near the nut location of the Kaiser hat. The calculation proceeded smoothly although the DTM inlet igniter fuel flow rate had shown some oscillations due to the sudden increase of the chamber pressure. At 0.6 seconds, the injector fuel flow rate had past the initial decline and was restored to its original level. Notice the fuel rich combustion and the sudden increase in chamber pressure had slowed down the flow vectors in the chamber. The hotter spot of the igniter flow had continued to propagate towards the ASI, as shown in Fig. 36.

At 0.6 seconds after time zero, the fuel flow rate begins its second drop to a mixture equivalence ratio of about five. It would rise a little bit but proceed to drop back to the same equivalence ratio of about five at 0.7 seconds. Fig. 37 shows the thermal flowfield at 0.7 seconds. The igniter flow flame

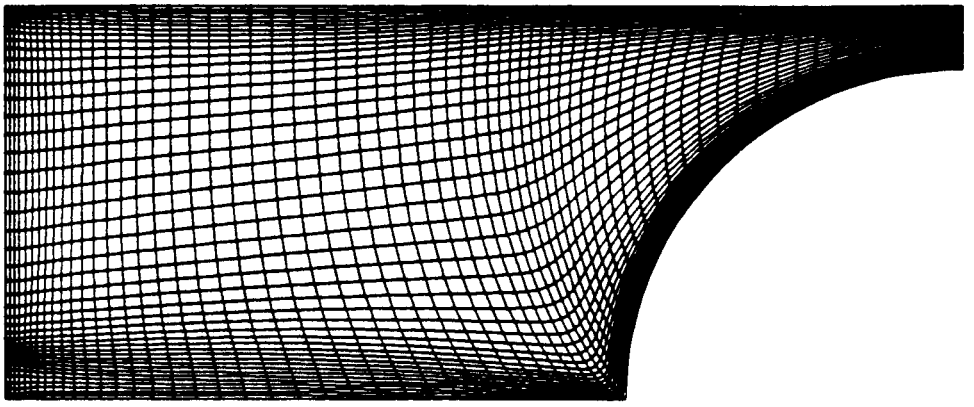

Fig. 29 Finite difference grid used to compute transient fuel preburner flowfield.

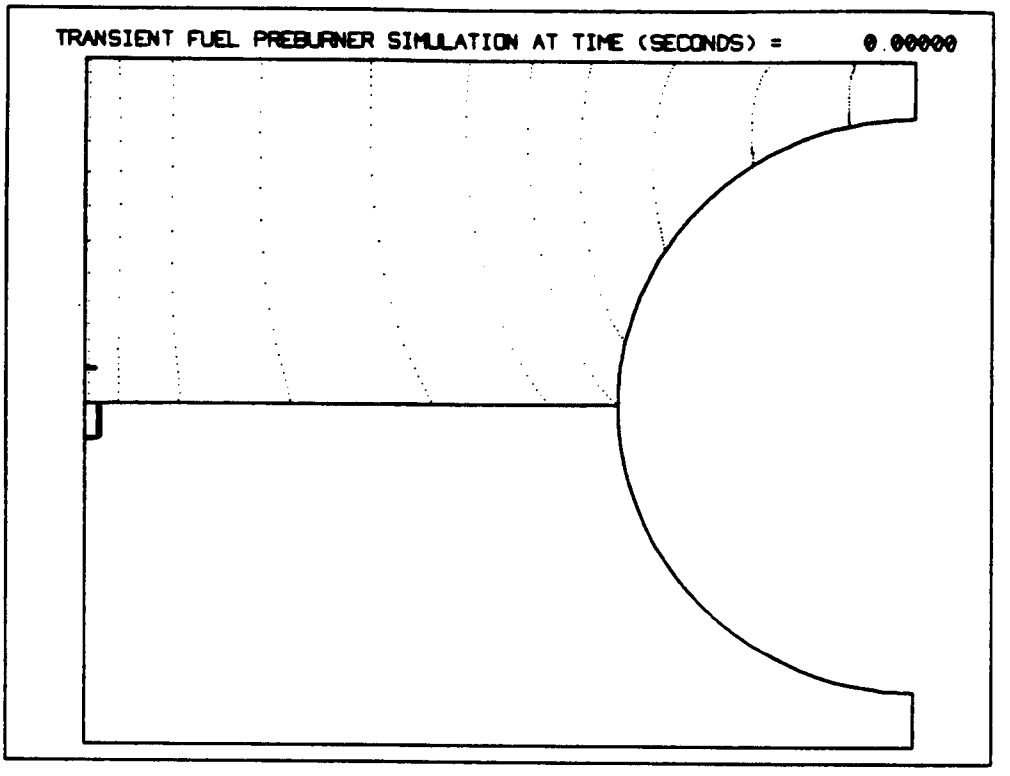
TRANSIENT FUEL PREBURNER SIMULATION AT TIME (SECONDS) = 0.00000

Fig. 30.

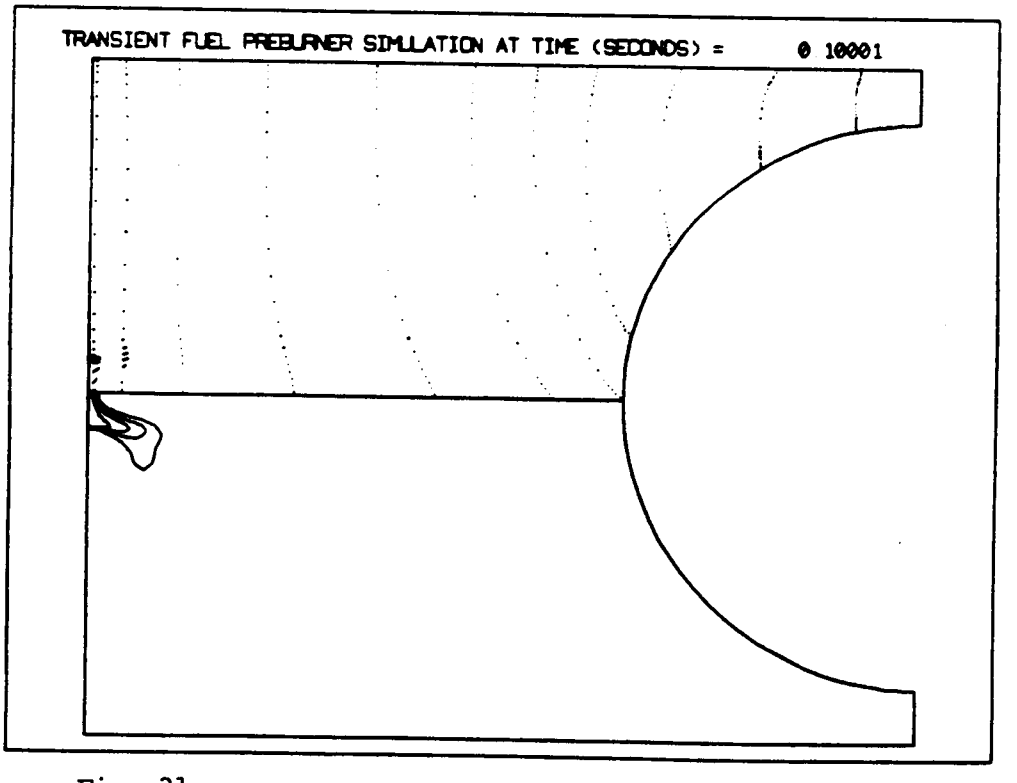
TRANSIENT FUEL PREBURNER SIMULATION AT TIME (SECONDS) = 0.10001

Fig. 31.

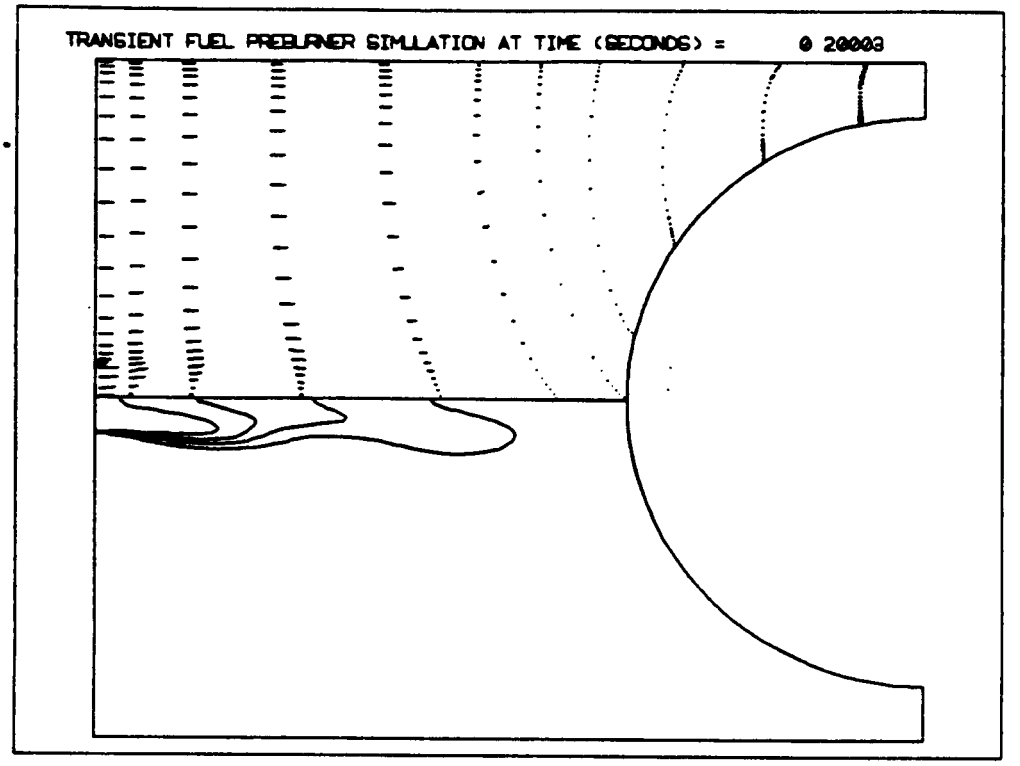
TRANSIENT FUEL PREBURNER SIMULATION AT TIME (SECONDS) = 0 20003

Fig. 32.

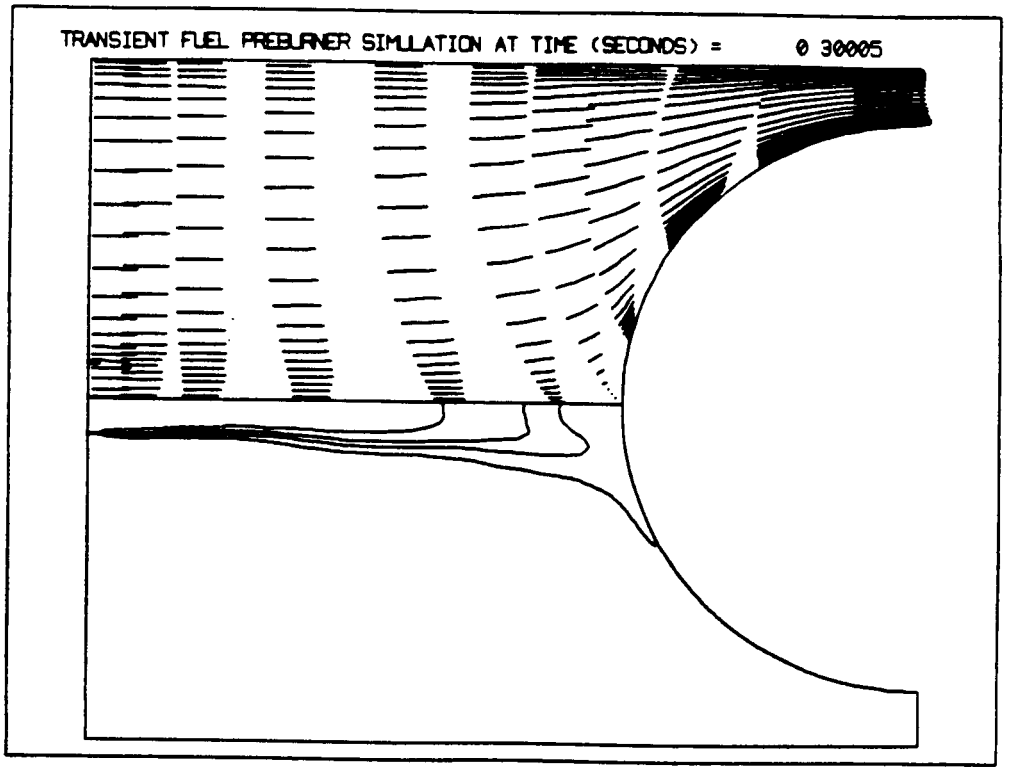
TRANSIENT FUEL PREBURNER SIMULATION AT TIME (SECONDS) = 0 30005

Fig. 33.

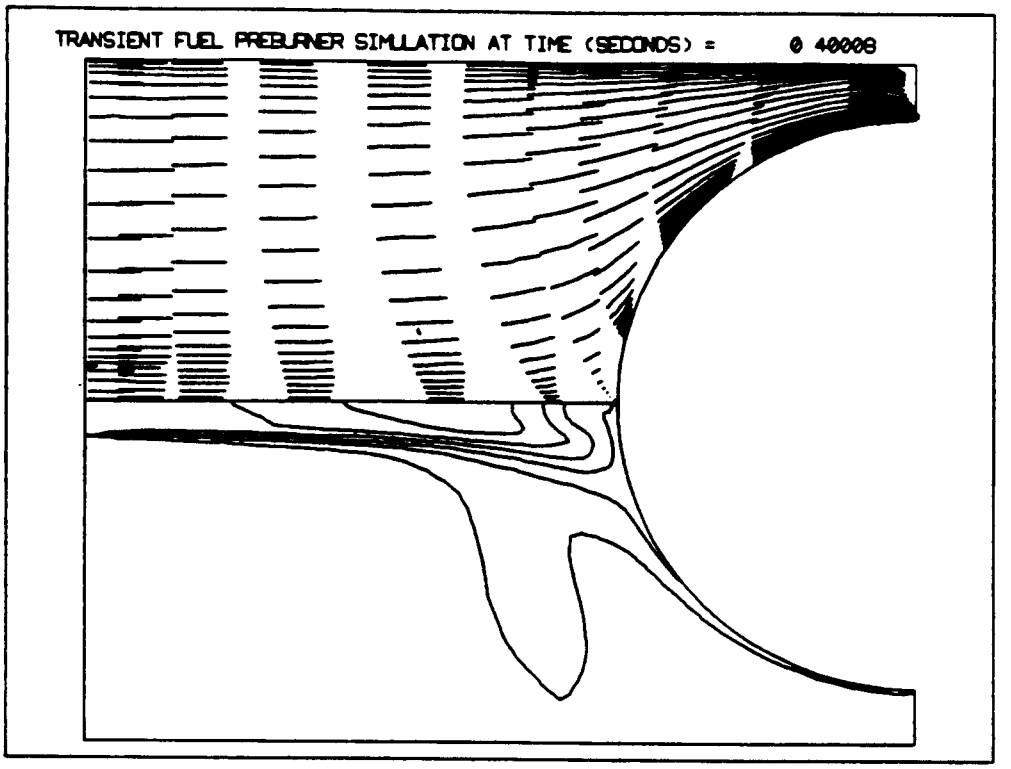
TRANSIENT FUEL PREBURNER SIMULATION AT TIME (SECONDS) = 0 40008

Fig. 34.

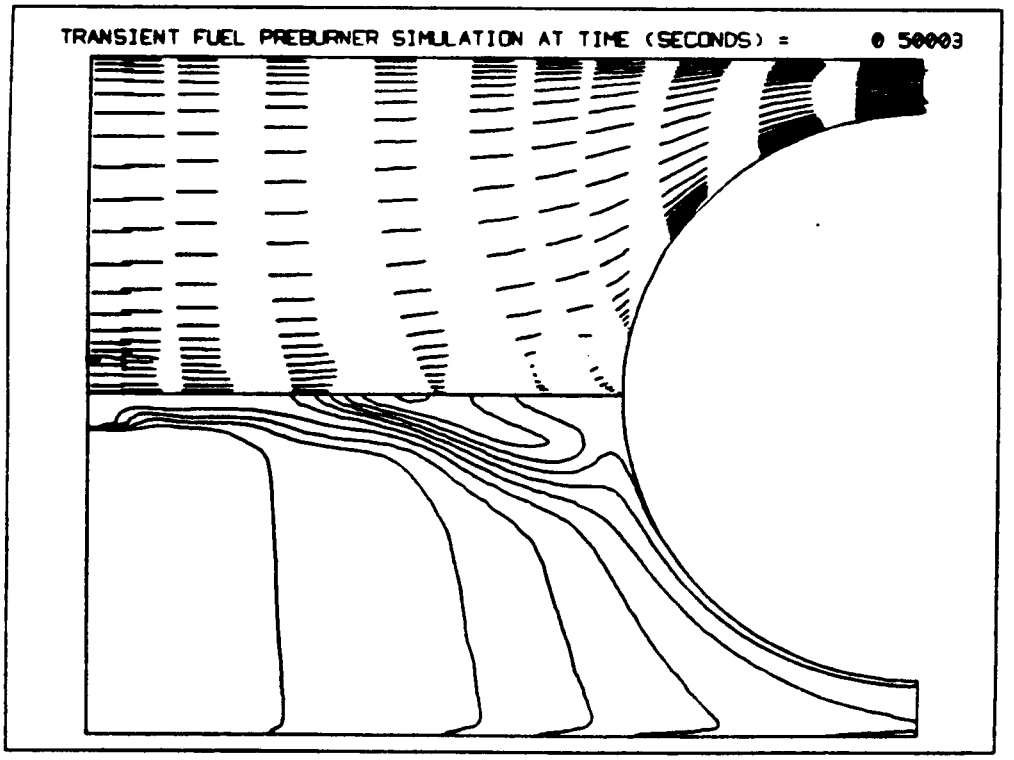
TRANSIENT FUEL PREBURNER SIMULATION AT TIME (SECONDS) = 0 50003

Fig. 35.

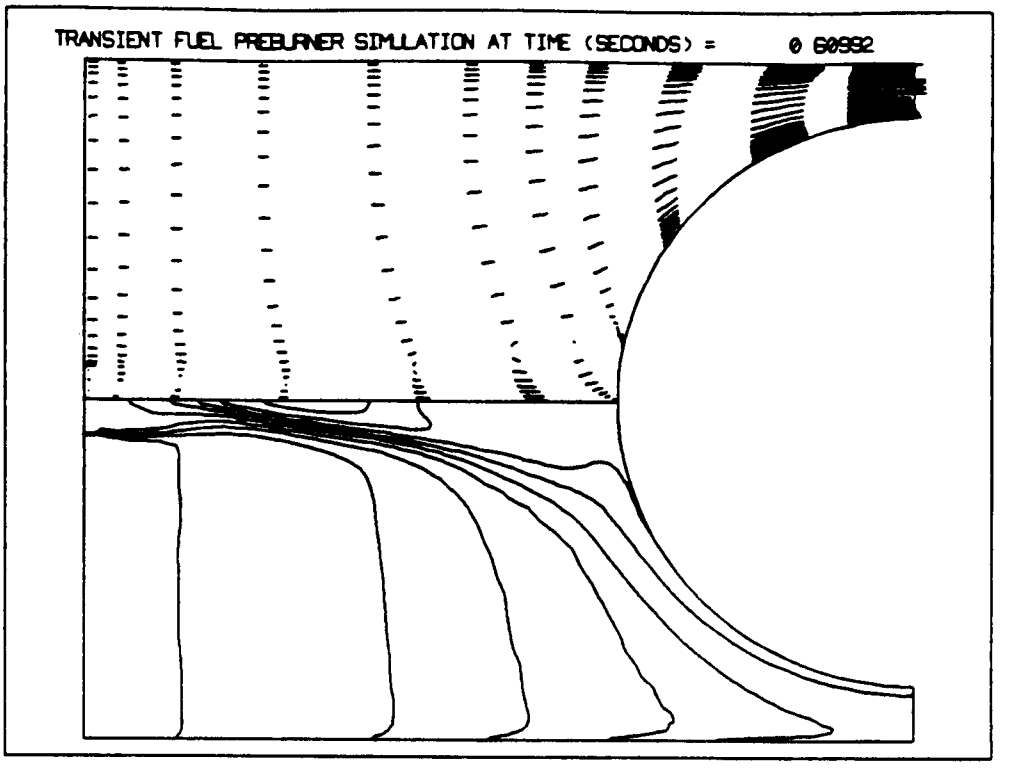
TRANSIENT FUEL PREBURNER SIMULATION AT TIME (SECONDS) = 0 60992

Fig. 36.

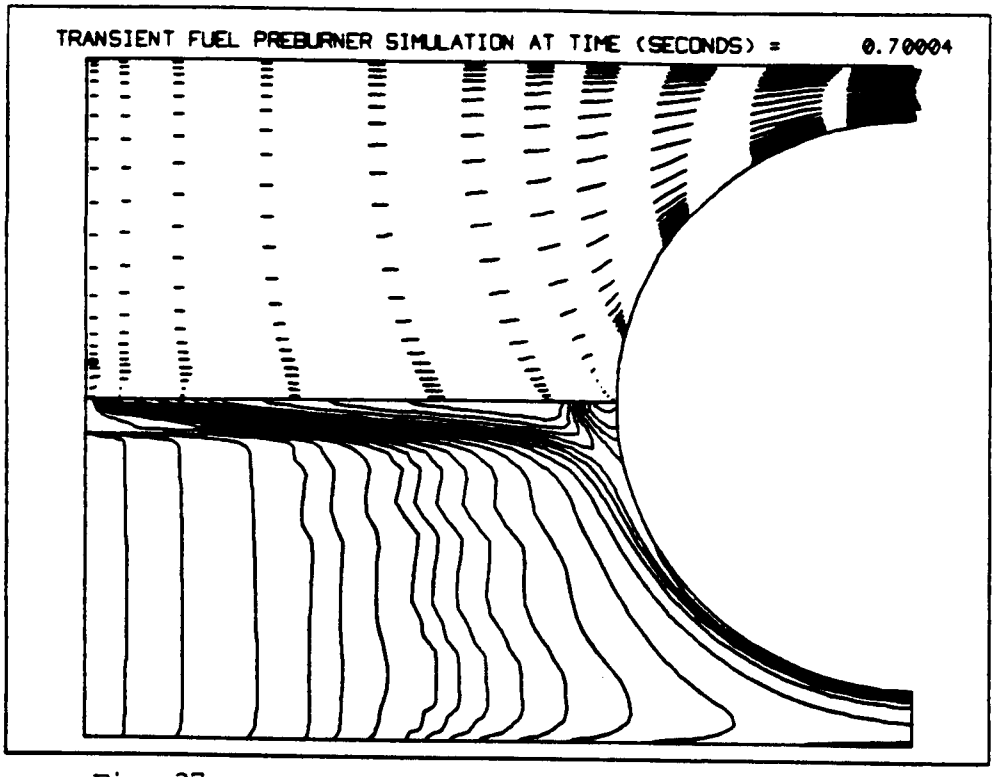
TRANSIENT FUEL PREBURNER SIMULATION AT TIME (SECONDS) = 0.70004

Fig. 37.

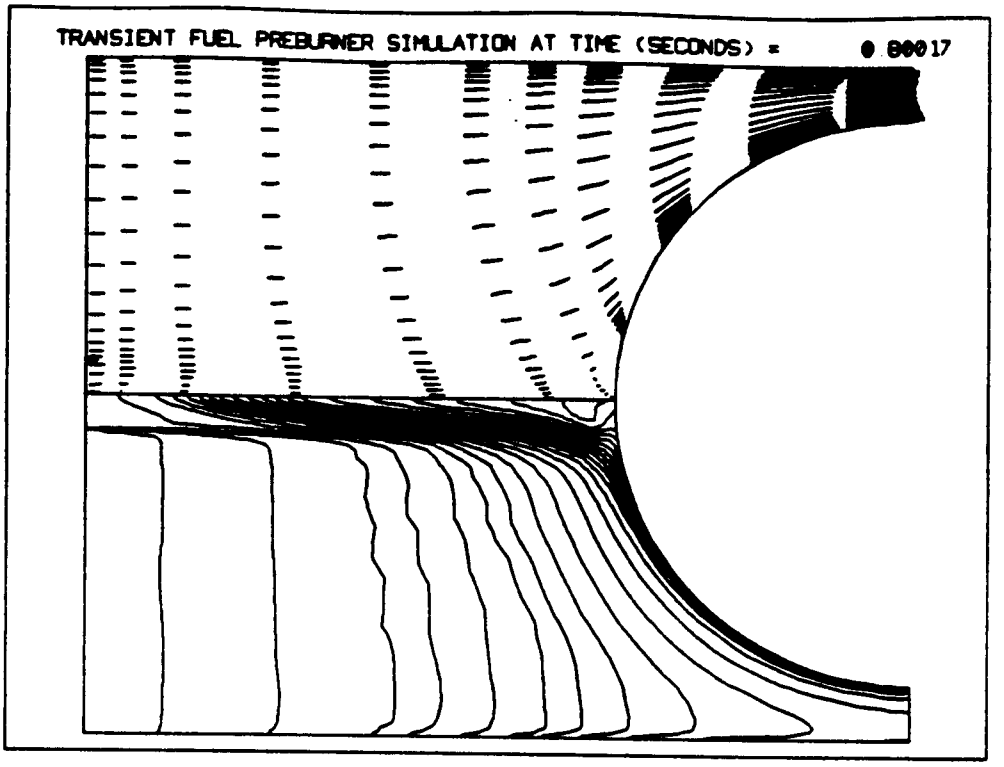
TRANSIENT FUEL PREBURNER SIMULATION AT TIME (SECONDS) = 0 80017

Fig. 38.

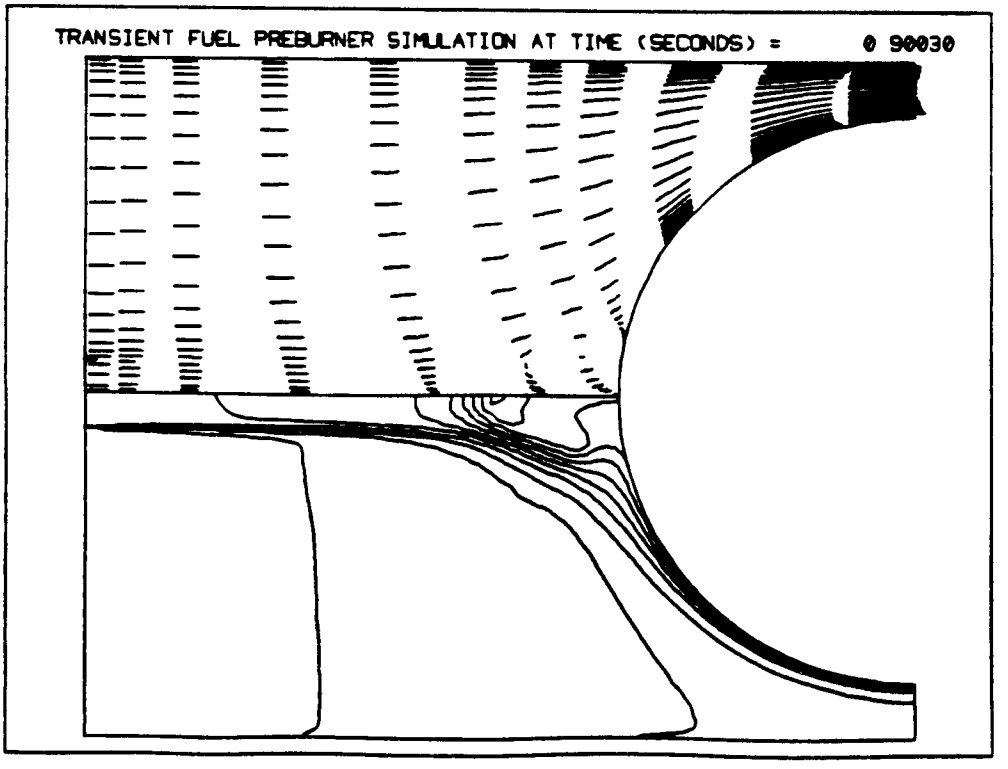
TRANSIENT FUEL PREBURNER SIMULATION AT TIME (SECONDS) = 0 90030

Fig. 39.

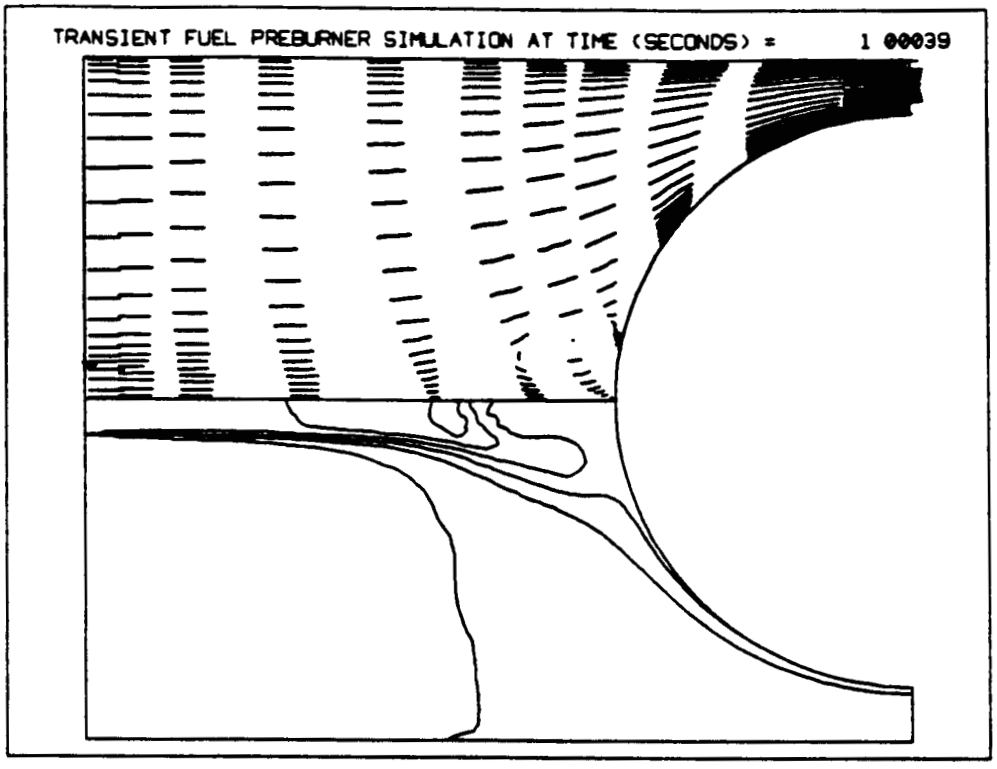
TRANSIENT FUEL PREBURNER SIMULATION AT TIME (SECONDS) = 1 00039

Fig. 40.

front had extended all the way back to the exit of the ASI chamber. Hot spots formed near the Kaiser hat nut, and hot streaks flowed over the turbopump dome. The hottest temperature (2700 deg. R) matches the DTM calculated peak temperature at 0.7 seconds for the nominal start. A disastrous start would have introduced near stoichiometric combustion in the combustion chamber. After 0.8 seconds, fuel rich combustion restored as a consequence of the increase in fuel flow rate. This is shown in Fig. 38.-40. In the present axisymmetric FPB study, the nut of the Kaiser hat seemed to withstand a prolonged period of high thermal gradients.

The transient radial temperature distribution at the fuel preburner exit is given in Fig. 41. The temperature rose 500 deg. R at about 0.5 seconds. A maximum temperature is reached at about 0.7 seconds. The radial temperature dropped afterwards due to the increase in fuel flow rate. Notice the temperature is hotter near the Kaiser hat wall side. This implies that the turbine blade fillets will undergo higher thermal gradients. Fig. 42 represents the transient temperature profile along the Kaiser hat wall. The hottest temperature occurred near the Kaiser hat nut at about 0.8 seconds. The centerline temperature distribution is shown in Fig. 43. A flame front started near the Kaiser-hat nut and moved toward the igniter flow inlet as time went on. The flame was then quenched after 0.8 seconds. The overall centerline temperature was near its hottest at about 0.7 seconds. The corresponding ASI exit temperature had reached about 1700 deg. R. The maximum temperature occurred near the nut at 0.8 seconds. This is probably due to the centerline recirculation zone formed in front of the nut.

A comparison of the FPB start-up transient temperature history at the fuel preburner exit and turbine inlet is shown in Fig. 44. Calculated temperature transients are given at two locations: at the middle of the exit line, and at the exit on the Kaiser-hat wall. The measured (ref. 3) turbine inlet temperature is represented by the thermocouple located near the inboard side of the turbine inlet and in between the baffles, so that three dimensional effects are minimized. Both the calculation and the measurement showed a peak at about 0.5 seconds, and a second peak at about 0.7 seconds. The temperature was then greatly reduced as the time approached one second. The measured first peak temperature is lower than that of the calculations. The final peak temperature and the peaking time of the FDNS2DR calculation at the middle of the FPB exit agreed very well with those of the measurement. The exit temperature calculated on the Kaiser hat wall is higher than that calculated at the middle of the exit, since the hotter striated torch flow was flowing near the turbopump dome. In general, the transient temperature history of the calculation showed qualitatively excellent agreement with that of the measurement.

The transient fuel preburner species mass fraction history at Kaiser hat nut is given in Fig. 45. The unburned oxygen mass

fraction dropped at 0.5 seconds, indicating the onset of the combustion. The mass fraction curve of the combustion product, H20, peaked at about 0.78 seconds, representing the highest temperature in the time frame considered. The unburned hydrogen mass fraction also dropped to its local minimum at 0.78 seconds. These three species mass fraction curves indicate that the combustion reaction near the Kaiser hat nut was almost complete, possibly with the help of flow recirculation. Similar curves are shown in Fig. 46 for the species mass fractions at the center of the fuel preburner exit. H20 mass fraction peaked and unburned hydrogen bottomed at an earlier 0.73 seconds. The unburned oxygen curve indicated an incomplete combustion, since ten to fifteen percent of oxygen was left unburned after 0.45 seconds. This is probably caused by the overall lower temperature in the injector region. Since the calculated temperature history at the fuel preburner exit based on the species composition was very closed to the measured turbine inlet temperature history, as previously shown in Fig. 44. The calculated species composition history is believed to be very close to the actual transient operation. Fig. 45 and 46 showed two different types of transient species composition history at two different flow situations. Obviously the remaining question is whether the unburned oxygen at the exit will cause near stoichiometric combustion in the complex flowfield of turbine stages, if so, this is certainly a likely source of initial turbine blade cracking and should be carefully studied with reactive CFD method.

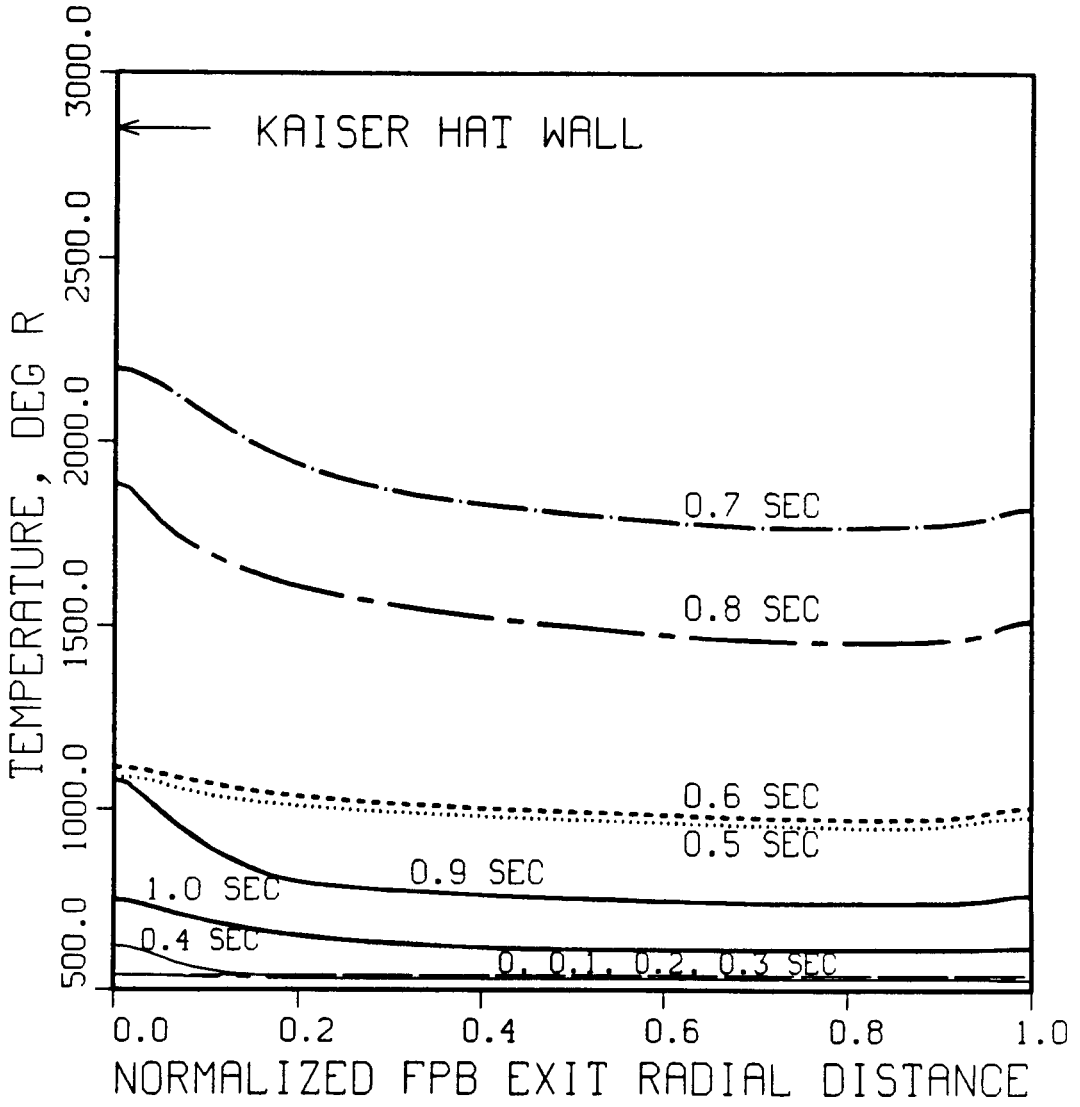

Fig. 41 Simulated radial temperature history at the fuel preburner exit.

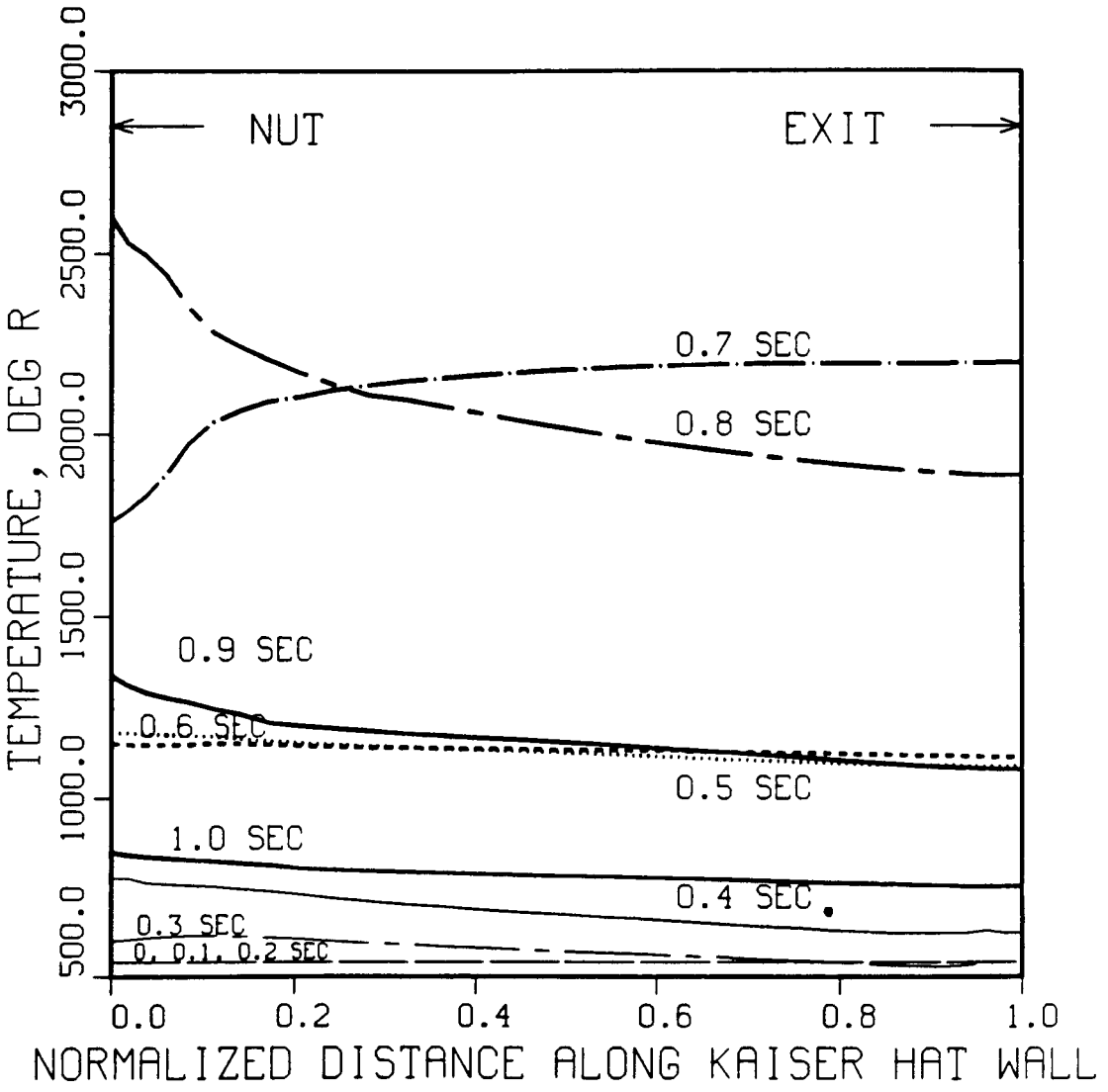

Fig. 42 Simulated temperature history along Kaiser hat wall.

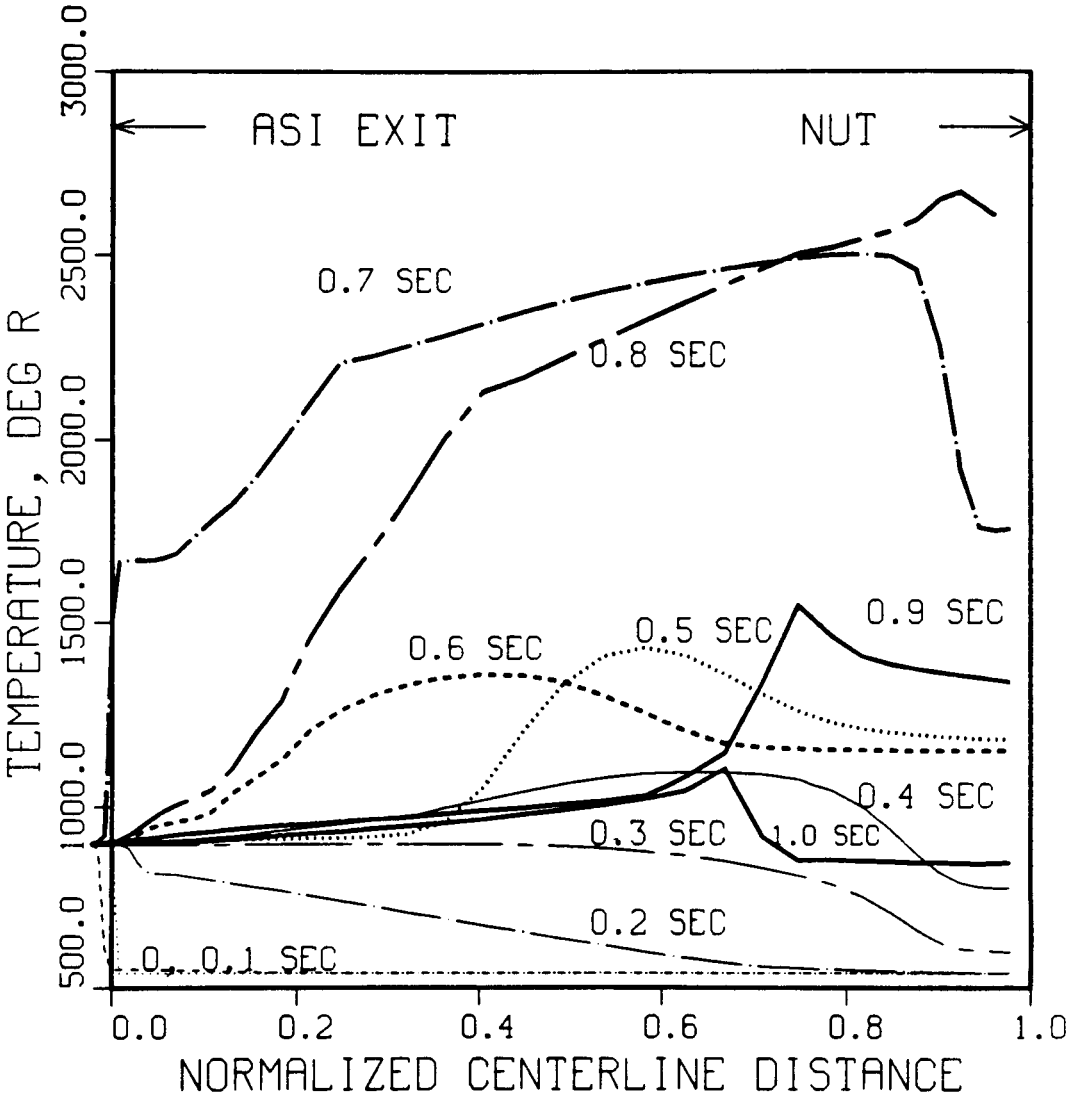

Fig. 43 Simulated centerline temperature history from ASI exit to Kaiser hat nut.

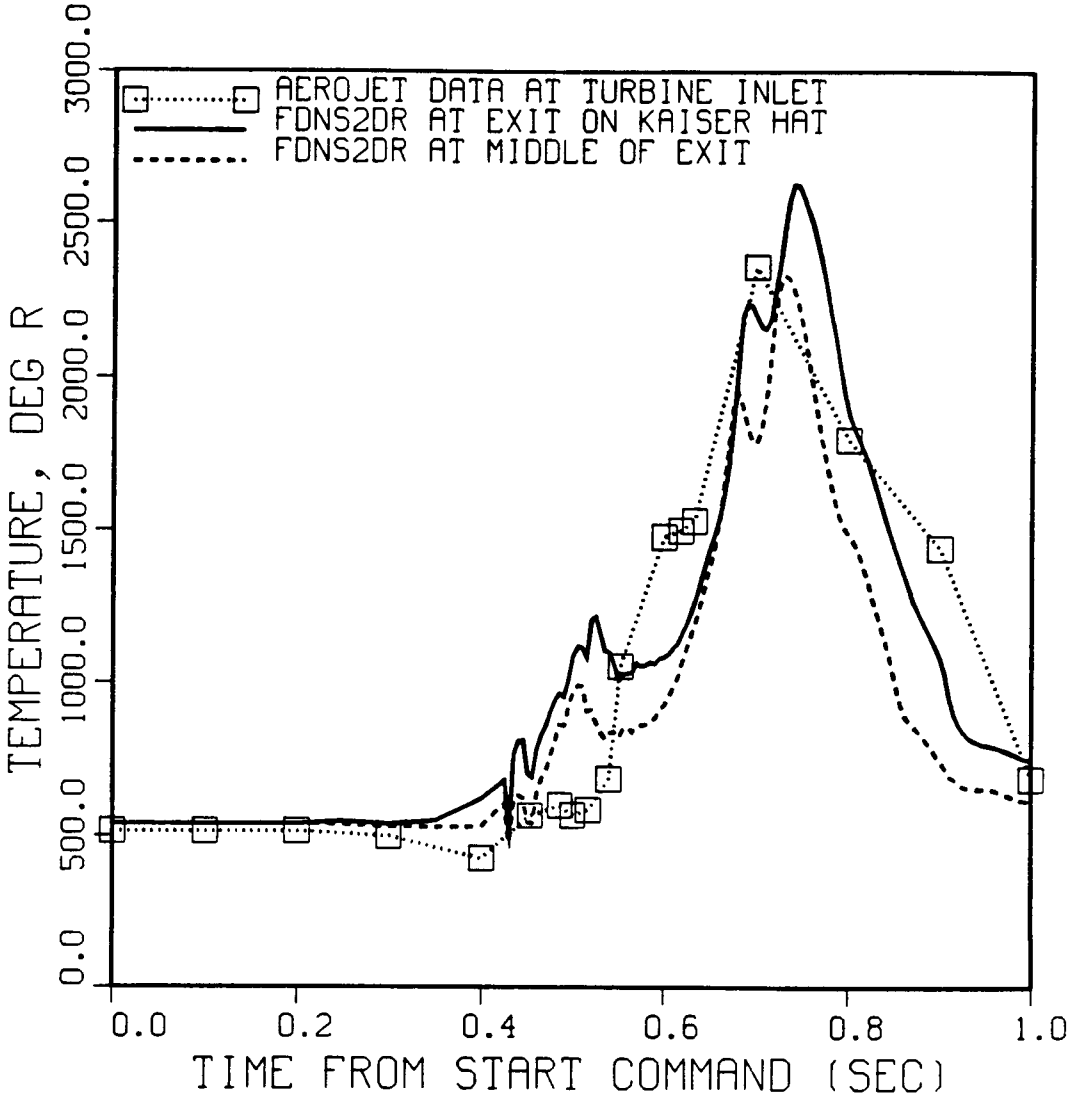

Fig. 44 Comparison of temperature history at calculated fuel preburner exit and measured turbine inlet.

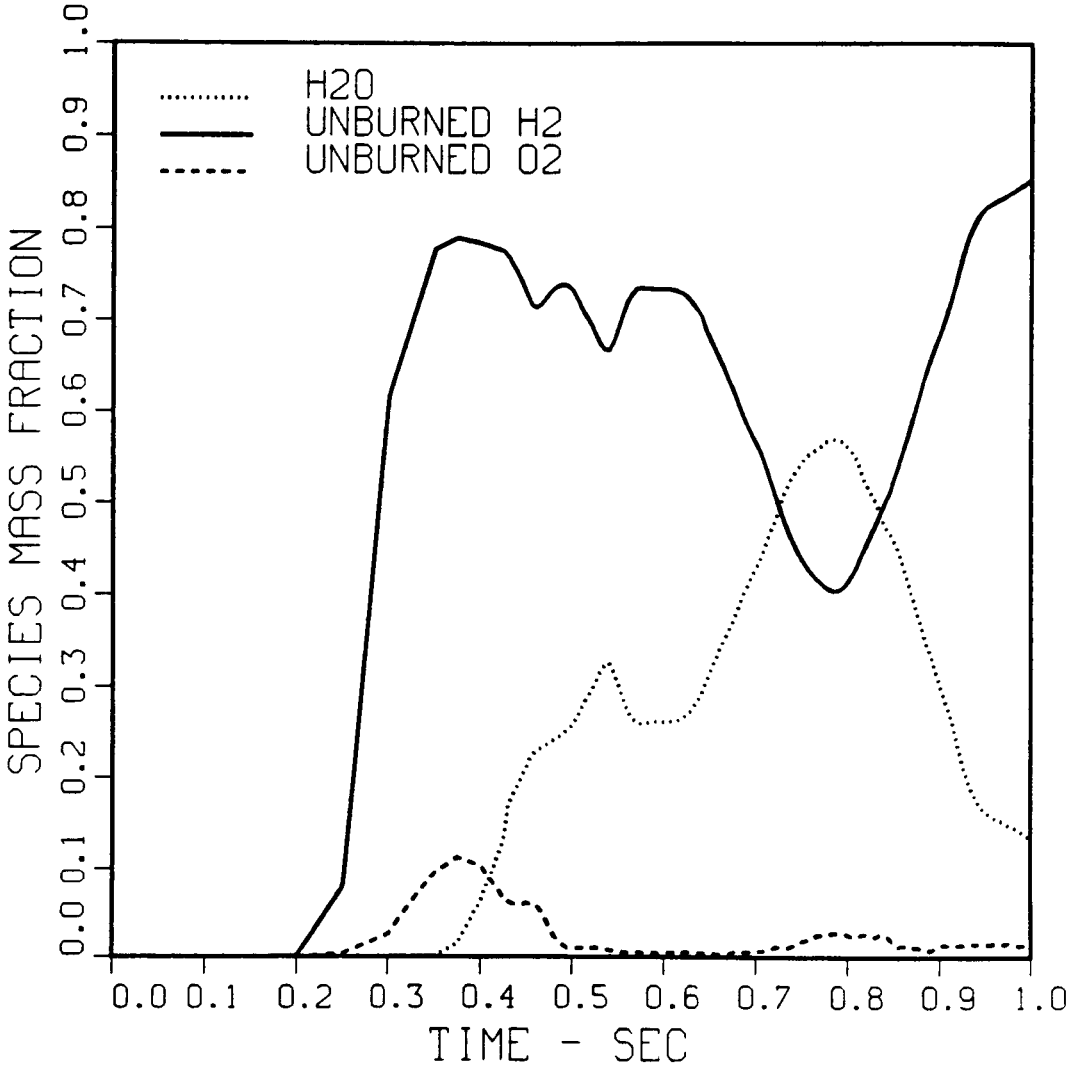

Fig. 45 Transient fuel preburner species mass fraction history at Kaiser hat nut.

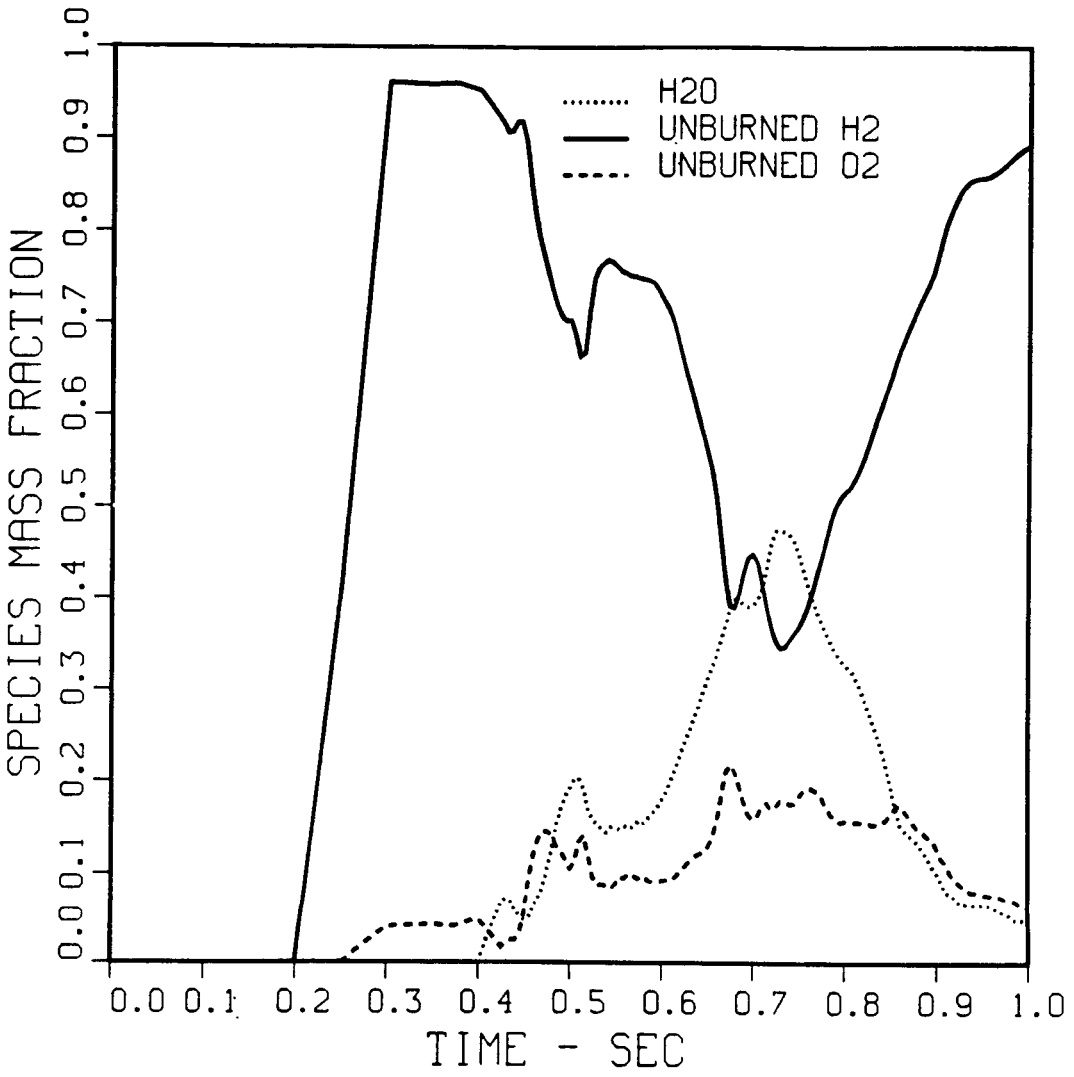

Fig. 46 Transient fuel preburner species mass fraction history at middle of exit.

Conclusions and Recommendations

A pressure based finite rate, reactive CFD model FDNS2DR has been developed to simulate the start transient of the SSME FPB operation. An axisymmetric configuration with a grid size of 68x45 was used to represent the FPB flowfield. The transient upstream boundary conditions were obtained from a one-dimensional DTM simulation to better represent the actual operation. The results of the CFD calculation have shown temperature spikes near the FPB exit. The timing and magnitude of the temperature spikes agreed well with those of the Aerojet measured turbine inlet temperature data. In addition, an appreciable amount of oxidizer was left unburned to enter the turbine stages. This results can not be obtained from a steady state CFD thermal flowfield simulation. Therefore, FDNS2DR is a useful CFD engineering design tool for studying the transient operation dominated SSME flow anomalies.

As a result of the transient thermal flowfields described by the analyses reported herein, the following future work is recommended:

1. Simulate a full three dimensional transient fuel preburner calculation so that the effect of baffle hydrogen flow can be included.

2. Parametrically run the DTM simulation so that the effect of different oxidizer valve sequences can be studied in conjunction with the downstream pressure wave characteristics. Various numerical experiments can also be performed with FDNS2DR to alter the ignition and shut down characteristics to study possible modifications to the operating procedure in order to attenuate the thermal shocks.

3. Although the thermal gradients in shutdown transient are less severe, but possibly more significant since the duration is much longer. A shutdown transient study is recommended for the complete understanding of the turbine blade crack problems.

4. Study the combustion characteristics of the unburned oxidizer once it enters the turbine stages.

REFERENCES

1. Wang, T.S. and Farmer, R.C., "Computational Analysis of the SSME Fuel Preburner Flow," Final Report, Contract NAS 8-35509, Report No. CI-FR-0084, Continuum Inc., Feb. 1986.

2. Liang, P.Y., R.J. Jensen, and Y.M. Chang, "Numerical Analysis of SSME Preburner Injector Atomization and Combustion Processes," AIAA-86-0454, AIAA 24th Aerospace Science Meeting, Reno, Nevada, Jan. 1986.

3. David, D., "Space Shuttle Engine Study," Vol. II, Interim Report, COntract 8-36176, Aerojet Tech. Systems Co., Sacramento, Ca., April, 1985.

4. Ryan, R.M., and L.A. Gross, "Effects of Geometry and Materials on Low Cycle Fatigue Life of Turbine Blades in LOX/Hydrogen Rocket Engines," AIAA-86-1443, AIAA/ASME/SAE/ASEE 22nd Joint Propulsion Conf., Huntsville, AL., June, 1986.

5. Anon, "SSME Orientation (part A - Engine)," Contract NAS8-27980, Rocketdyne Div., Rockwell International, Canoga Park, Ca., Oct., 1982.

6. Defever, G.J., and S.C. Fisher, "Refined Coaxial Element Hot Fire Test Report," CDR-85-176, Rocketdyne Div., Rockwell International, Canoga Park, Ca., Nov. 1985.

7. Rosner, D.E., "On Liquid Drop Combustion at High Pressures," AIAA J., Vol. 5, pp.163-166. 1967.

8. Seymour, D., EP55, Performance Analysis Branch. MSFC/NASA, Personal Communication.

9. Steger, J.L. and Warming, R.F., "Flux Vector Splitting of the Inviscid Fluid Dynamics Equations with Application to Finite-Difference Methods," J. Comp. Physics, 40, pp. 263-293, 1981.

10. Van Leer, B., Thomas, J.L., Roe, P.L. and Newsome, R.W., "A Comparison of Numerical Flux Formulas For The Euler and Navier-Stokes Equations," AIAA Paper 87-1104, July 1987.

11. Roe, P.L., "Approximate Riemann Solvers, Parameter Vectors, and Difference Schemes," J. Comp. Physics, 43, pp. 357-372, 1981.

12. Osher, S. and Chakravarthy, S., "Upwind Schemes and Boundary Conditions with Applications to Euler Equations in General Geometries," J. Comp. Physics, 50, p. 447, 1983.

13. Harten, A., "High Resolution Schemes for Hyperbolic Conservation Laws," J. Comp. Physics, 49, pp. 357-393, 1983.

14. McCormack, R.W., "Current Status of Numerical Solutions of

the Navier-Stokes Equations," AIAA Paper 85-0032, Jan. 1985.

15. Jameson, A., Schmidt, W. and Turkel, E., " Numerical Solution of the Euler Equations by Finite Volume Methods Using Runge-Kutta Time Stepping Schemes," AIAA Paper 81-1259, 1981.

16. Jameson, A., "A Nonoscillatory Shock Capturing Schemes Using Flux Limited Dissipation," Lectures in Applied Mathematics, 22, Part I, AMS, pp. 345-370, 1985.

17. Pulliam, T.H., "Artificial Dissipation Models for the Euler Equations," AIAA J., 24, pp. 1931-1940, Dec. 1986.

18. Launder, B.E. and Spalding, D.B., "The Numerical Computation of Turbulent Flows," Comp. Meth. Appl. Mech. Engr., 3, 269-289, 1974.

19. Chen, Y.S., "Viscous Flow Computations Using a Second-Order Upwind Differencing Scheme," AIAA Paper 88-0417, Jan. 1988.

20. Peric, M., "Efficient Semi-Implicit Solving Algorithm for Nine-Diagonal Coefficient Matrix," Numerical Heat Transfer, 11, pp. 251-279, 1987.

21. Stone, H.L., "Iterative Solution of Implicit Approximations of Multidimensional Partial Differential Equations," SIAM J. Numer. Anal., 5, pp. 530-558, 1968.

22. Magnus, D.E., and Schechter, H.S., "Analysis of Error Growth and Stability for the Numerical Integration of the Equations of Chemical Kinetics," GASL TR-607, 1966.

23. Dongarra, J.J., J.R. Bunch, C.B. Moler and G.W. Stewart, LINPACK User's Guide, SIAM, 1979.

24. Moretti, G., "A New Technique for the Numerical Analysis of Nonequilibrium Flows," AIAA J., 3, No. 2, pp. 223-229, 1965.

25. Chen, Y.S., and Kim, S.W., "Computation of Turbulent Flows Using an Extended k-ε Turbulence Closure Model," NASA CR-179204, Oct. 1987.

26. Wang, T.S., Farmer, R.C., and Edelman, R.B., "Turbulent Combustion Kinetics for Complex Hydrocarbon Fuels," AIAA Paper 88-0733, Jan. 1988.

27. Wang, T.S., Farmer, R.C., and Tucker, K., "Turbulent Hydrocarbon Combustion Kinetics - Stochastic Modeling and Verification," AIAA Paper 89-0486, Jan. 1989.

28. Janica, J. and Kollmann, W., "A Two Variables Formalism for the Treatment of Chemical Reactions in Turbulent H_2-Air Diffusion Flames," Seventeenth Symp. (Int'l) on Combustion, 1979, pp. 421-429.

29. Rogers, R.C., and W. Chinitz, "Using a Global Hydrogen-Air Combustion Model in Turbulent Reacting Flow Calculations," AIAA J., 21, No. 4, 1983, pp. 586-592.

30. Roback, R., and Johnson, B.V., "Mass and Momentum Turbulent Transport Experiments with Confined Swirling Coaxial Jets," NASA CR-168252, 1983.

31. Edelman, R.B., Harsha, P.T., and Schmotolocha, S.N., "Modeling Techniques for the Analysis of Ramjet Combustion Process," AIAA Paper 80-1190, June 1980.

32. Harsha, P.T., Edelman, R.B., Schmotolocha, S.N., and Pederson, R.J., "Combustor Modeling for Ramjet Development Programs," AGARD CP 307, March 1982.

33. Drummond, J.P., "Numerical Study of a Ramjet Dump Combustor Flowfield," AIAA J., 23, No. 4, Apr. 1985, pp. 604-611.

34. MacCormack, R.W., "The Effect of Viscosity in Hypervelocity Impact Cratering," AIAA Paper 69-354, April 1969.

35. Trinh, H.P., "Numerical Study of Hydrogen-Air Mixing Flowfield in A Ramjet Combustor", M.S. Thesis, University of Missouri-Rolla, 1987.

36. Smith, G.D., and Giel, T.V., "An Experimental Investigation of Reactive, Turbulent, Recirculating Jet Mixing," AEDC-TR-79-79, May 1980.

37. Chaturvedi, M.C., "Flow Characteristics of Axisymmetric Expansion," J. Hydraulics Division, Proceedings of the American Society of Civil Engineers, 89, No. HY3, May 1963, pp. 61-92.

38. Space Transportation System Technical Manual - Space Shuttle Main Engine Description and Operation, E41000, RSS-8559-1-1-1, Rocketdyne Division, Rockwell International Corporation, April, 1982.

39. Nguyen, D.G., "Engine Balance and Dynamic Model", RL00001, Rocketdyne Division, Rockwell International Corporation, Sept., 1981.

40. Wang, T.S., and B.K. Soni, "Goodness of Grid: Quantitative Measures," AIAA-88-3736, First National Fluid Dynamics Congress, Cincinnati, June 1988.

APPENDIX

THERMODYNAMIC AND TRANSPORT PROPERTIES FOR OXYGEN

- Introduction

Thermodynamic properties of single-component fluids are defined in terms of thermal and caloric equations of state. At low pressures or high molal volumes, all substances are gases which obey the perfect gas equation of state.

$$P = RT/MV$$

where P is pressure, R is the universal gas constant, T is temperature, M is molecular mass, and V is specific volume (1/density). The caloric equation of state relates enthalpy, H, or internal energy, U, to two state variables, say temperature and density. If the internal energy is a function of temperature only, the gas is said to be ideal. If the gas is thermally perfect and calorically ideal,

$$C_p/C_v = 1 + R/C_v$$

where C_p and C_v are constant pressure and constant volume heat capacities, respectively. If the heat capacities are constant, the ratio

$$\gamma = C_p/C_v$$

is conveniently used to represent all of the thermodynamic properties of the gas. In general, as molal volumes decrease or density increase these simple relationships become invalid; at even higher pressures the "gases" condense to form liquids. The theorem of corresponding states postulates that the critical conditions may be used to non-dimensionalize the equations of state so that all pure gases exhibit the same compressibility factors at the same reduced density and temperature. The compressibility is a multiplitive term included in the perfect gas law to make it apply to any temperature and density. Figures 1 and 2 show a non-dimensionalized plot of O_2 properties as predicted by the methods described herein which are in agreement with the data reported by NBS (1,2). Using a third parameter, the critical compressibility, pressure and enthalpy are well correlated in terms of reduced density and temperature for many substances (3). A more convenient correlation is that reported in (4,5) as the HBMS equation of state, since all of the correlations are expressed as analytic functions. Representations of the NBS thermodynamic data with the HBMS model and of transport property empirical correlation equations will be summarized so that the required properties for two-phase flow analysis of oxygen can be provided for a numerical solution to the conservation equations.

- The Thermal Equation of State

The pressure data shown in Figure 1 may be divided into a gas region (I), a dense gas region (II), a liquid region (III), and a two-phase region (IV). Solid oxygen will not be considered. The gas region may be represented with a modification to the perfect gas law. Van der Waals' equation of state accounts for the energy of attraction between molecules with the "a" term and for physical volume occupied by the molecules with the "b" term.

$$(P + a/V^2)(V-b) = RT$$

The HBMS equation generalizes this equation, thusly

$$[P + a\{T\}/V^2 + a'\{T\}/V^3][V - b + b'/V] = RT$$

Temperature, density, and pressure are non-dimensionalized by dividing by the critical temperature, density and pressure, respectively. These variables are denoted by t, ρ, and p, respectively. Braces are used herein to denote functionality. The functions a and a', and the constants b and b' were evaluated in (4) to produce the HBMS/I equation of state.

$$p_I = -(k_0+(\beta-k_0)t^{-1})\rho^2 - 0.5(1-k_0-\alpha+2\beta)(t+t^{-1})\rho^3 +$$

$$(1+\beta)^3\rho t/[\beta(3\beta-1)-(3\beta^3-6\beta-1)\rho+\beta(\beta-3)\rho^2]$$

where k_0 is 5.5, $\alpha = 7 +(z_c^{-1} - 3.72)/0.26$, and β is defined by

$$z_c = P_cV_c/RT_c = \beta(3\beta-1)/(1+\beta)^3$$

Alternative expressions are given for k_0 and α in (4), but they are not needed to represent O_2 properties.

The expression for pressure required modification to represent the dense gas region, so HBMS/II was developed (4).

$$p_{II} = t^{-1}[B_{30}\rho^2 + B_{40}\rho^3] +$$

$$[B_{01}\rho^{-1} + B_{11} + B_{21}\rho + B_{31}\rho^2 + B_{41}\rho^3] +$$

$$t[B_{02}\rho^{-1} + B_{12} + B_{22}\rho + B_{32}\rho^2 + B_{42}\rho^3 + B_{52}\rho^4] +$$

$$t^2[B_{03}\rho^{-1} + B_{13} + B_{23}\rho + B_{33}\rho^2]$$

In HBMS's nomenclature, this equation is

$$p_{II} = \Sigma\ t^{j-1}\ Q_j\{\rho\} \qquad \text{where } j = 0, 1, 2, 3.$$

For the liquid region, HBMS/III is

$$p_{III} = \Sigma\ t^{j-1}\ (Q_j\{\rho\} - Q_j\{\rho_L\}) + p_v \qquad \text{where } j = 0, 1, 2, 3.$$

The saturated liquid density, ρ_L, and the vapor pressure, p_V, must be obtained from additional correlation equations. Riedel's vapor pressure equation was used in (4) because of its accuracy near the critical point.

$$\ln\{p_V\} = \alpha \ln\{t\} + 0.0838(\alpha - 3.75)(36t^{-1} - 35 - t^6 + 42 \ln\{t\})$$

This equation becomes progressively less accurate as the normal boiling point is approached. Attempts to interpret α as a parameter to fit the vapor pressure at arbitrary temperatures destroy the accuracy of the fit near the critical point. Other vapor pressure correlations should be considered if the region of interest includes pressures which are less than 0.4 T_C; the NBS report (1) suggests a high order polynominal which is used herein.

$$\ln\{P\} = A_1 + A_2T + A_3 T^2 + A_4 T^3 + A_5 T^4 + A_6 T^5 + A_7 T^6 + A_8 T^7$$

where P is in atm and T in Kelvins. The A's are:

$A_1 = -62.5967185$ $\quad A_2 = 2.47450429$

$A_3 = -4.68973315E\text{-}2$ $\quad A_4 = 5.48202337E\text{-}4$

$A_5 = -4.09349868E\text{-}6$ $\quad A_6 = 1.91471914E\text{-}8$

$A_7 = -5.13113688E\text{-}11$ $\quad A_8 = 6.02656934E\text{-}14$

Predictions with these two vapor pressure correlations are shown in Figure 3. The polynominal equation fits the data over a wider range of temperatures. If an accurate vapor pressure correlation is not available for a specific gas of interest, such a correlation should be developed.

The saturated liquid density may be represented by

$$\rho_L(t) = 1 + c(1-t)^{1/3} + d(1-t)$$

where c and d are evaluated by using two data points from the saturated liquid curve (1). Predictions with this equation are compared to the NBS data in Figure 4; the comparison is very good.

The working form of the HBMS/III pressure equation is

$$p_{III} = t^{-1}[B_{30}\rho^2 + B_{40}\rho^3] +$$
$$[B_{01}\rho^{-1} + B_{11} + B_{21}\rho + B_{31}\rho^2 + B_{41}\rho^3] +$$
$$t[B_{02}\rho^{-1} + B_{12} + B_{22}\rho + B_{32}\rho^2 + B_{42}\rho^3 + B_{52}\rho^4] +$$
$$t^2[B_{03}\rho^{-1} + B_{13} + B_{23}\rho + B_{33}\rho^2] -$$
$$t^{-1}[B_{30}\rho_L^2 + B_{40}\rho_L^3] -$$

$$[B_{01}\rho_L^{-1} + B_{11} + B_{21}\rho_L + B_{31}\rho_L^2 + B_{41}\rho_L^3] -$$

$$t[B_{02}\rho_L^{-1} + B_{12} + B_{22}\rho_L + B_{32}\rho_L^2 + B_{42}\rho_L^3 + B_{52}\rho_L^4] -$$

$$t^2[B_{03}\rho_L^{-1} + B_{13} + B_{23}\rho_L + B_{33}\rho_L^2] + p_v(t)$$

The values of the B_{ij}'s are given below. These values correspond to those given in the text of (4); they do not match the values given in the tables of either (4) or (5) which apparently contain some algebraic errors.

$$B_{30} = 5.5 - \beta$$

$$B_{40} = -2.25 - 0.5\ \alpha + \beta$$

$$B_{01} = 88.5 - 3.12\ \beta$$

$$B_{11} = -313.3 + 13.42\ \beta$$

$$B_{21} = 408.9 - 21.54\ \beta$$

$$B_{31} = -237.4 + 15.30\ \beta$$

$$B_{41} = 47.8 - 4.06\ \beta$$

$$B_{02} = -124.46 + 3.84\ \beta + 0.363\ \beta^2$$

$$B_{12} = 429.0 - 9.84\ \beta - 1.815\ \beta^2$$

$$B_{22} = -528.8 + 1.98\ \beta + 0.363\ \beta^2$$

$$B_{32} = 263.0 + 15.70\ \beta - 3.63\ \beta^2$$

$$B_{42} = -27.05 + 0.5\ \alpha - 16.18\ \beta + 1.815\ \beta^2$$

$$B_{52} = -8.44 + 4.50\ \beta - 0.363\ \beta^2$$

$$B_{03} = 44.4 - 5.22\ \beta$$

$$B_{13} = -156.9 + 18.92\ \beta$$

$$B_{23} = 204.3 - 25.44\ \beta$$

$$B_{33} = -115.5 + 15.0\ \beta$$

$$B_{43} = 23.7 - 3.2\ \beta$$

Predicted pressures as a function of temperature and density are shown in Figure 1. The HBMS thermal equation of state is an excellent representation of the NBS data.

- The Caloric Equation of State

For the gas region, the internal energy excess function may be written as

$$(U - U_0)/RT = z_c \int_0^{\rho} \left[\frac{p}{t} - \left(\frac{\partial \rho}{\partial t} \right)_{\rho} \right] \frac{d\rho}{\rho^2}$$

Since $H = U + PV$,

$$(H_I - H_0)/RT = z_c \int_0^{\rho} \left[\frac{p}{t} - \left(\frac{\partial \rho}{\partial t} \right)_{\rho} \right] \frac{d\rho}{\rho^2} + (z_c\, p/\rho t) - 1$$

For the dense gas region, the enthalpy excess function is

$$(H_{II} - H_0)/RT = z_c \int_1^{\rho} \left[\frac{p}{t} - \left(\frac{\partial \rho}{\partial t} \right)_{\rho} \right] \frac{d\rho}{\rho^2} + \frac{z_c}{t} \left[\frac{p}{\rho} - p_1 \right] + (H_1 - H_0)/RT$$

where p_1 and H_1 are evaluated at the intersection between the gas and the dense gas regions. For the liquid region,

$$(H_{III} - H_0)/RT = z_c \int_{\rho_L}^{\rho} \left[\frac{p}{t} - \left(\frac{\partial \rho}{\partial t} \right)_{\rho} \right] \frac{d\rho}{\rho^2} + \frac{z_c}{t} \left[\frac{p}{\rho} - \frac{p_v}{\rho_L} \right] + (H_L - H_0)/RT$$

Inserting the appropriate pressure equation in the enthalpy excess function, the following working equations are obtained.

$$(H_I - H_0)/RT = - z_c[2k_0\, t^{-1} + 3(\beta - k_0)t^{-2})\rho + 0.5(1-k_0-\alpha+2\beta)(1-2t^{-2})\rho^2] + (1-b\rho+b'\rho^2)^{-1} + 1$$

where $b = (3\beta^2-6\beta-1)/\beta(3\beta-1)$ and $b' = (\beta-3)(3\beta-1)$.

$$(H_{II} - H_0)/RT = t^{-2}[3B_{30}\rho + 2B_{40}\rho^2] + t^{-1}[0.5B_{01}\rho^{-2} + B_{21} \ln(\rho) + 2B_{31}\rho + 1.5B_{41}\rho^2] + [B_{02}\rho^{-2} + B_{12}\rho^{-1} + B_{32} + B_{42}\rho^2 + B_{52}\rho^3] - t^{-2}[3B_{30} + 2B_{40}] - t^{-1}[0.5B_{01} + 2B_{31} + 1.5B_{41}] - [B_{02} + B_{12} + B_{32} + B_{42} + B_{52}] + z_c\, t^{-1}[p_{II}\rho^{-1} - p_1] + (H_1 - H_0)/RT$$

where $p_1 = -(k_0+(\beta-k_0)t^{-1}) - 0.5(1-k_0-\alpha+2\beta)(t+t^{-1}) + (1+\beta)^3 t/[\beta(3\beta-1)-(3\beta^3-6\beta-1)+\beta(\beta-3)]$

and

$$(H_I - H_0)/RT = - z_c[(2k_0\ t^{-1} + 3(\beta-k_0)t^{-2}) + 0.5(1-k_0-\alpha+2\beta)(1-2t^{-2})]$$
$$+ (1-b+b')^{-1} + 1$$

For the liquid region,

$$(H_{III} - H_0)/RT = z_c[t^{-2}[3B_{30}\rho + 2B_{40}\rho^2] + t^{-1}[0.5B_{01}\rho^{-2} + B_{21}\ln(\rho) + 2B_{31}\rho$$
$$+ 1.5B_{41}\rho^2] + [B_{02}\rho^{-2} + B_{12}\rho^{-1} + B_{32} + B_{42}\rho^2 + B_{52}\rho^3]$$
$$- t^{-2}[3B_{30}\rho_L + 2B_{40}\rho_L^2] - t^{-1}[0.5B_{01}\rho_L^{-2} + B_{21}\ln(\rho_L) +$$
$$2B_{31}\rho_L + 1.5B_{41}\rho_L^2] - [B_{02}\rho_L^{-2} + B_{12}\rho_L^{-1} + B_{32} + B_{42}\rho_L^2 +$$
$$B_{52}\rho_L^3]] - z_c[2t^{-2}(B_{30}\rho_L^2 + B_{40}\rho_L^3) + t^{-1}(B_{01}\rho_L^{-1} + B_{11} +$$
$$B_{21}\rho_L + B_{31}\rho_L^2 + B_{41}\rho_L^3) - t(B_{03}\rho_L^{-1} + B_{13} + B_{23}\rho_L +$$
$$B_{33}\rho_L^2 + B_{43}\rho_L^3)](\rho_L^{-1} - \rho^{-1}) + z_c[t^{-2}(2B_{30}\rho_L + 3B_{40}\rho_L^2) +$$
$$(-B_{01}\rho_L^{-2} + B_{21} + 2B_{31}\rho_L + 3B_{41}\rho_L^3) + t(-B_{02}\rho_L^{-2} + B_{22} +$$
$$2B_{32}\rho_L + 3B_{42}\rho_L^2 + 4B_{52}\rho_L^3) + t^2(-B_{03}\rho_L^{-2} + B_{23} + 2B_{33}\rho_L +$$
$$3B_{43}\rho_L^2)](\rho_L^{-1} - \rho^{-1})\left(\frac{d\rho_L}{dt}\right) + z_c(p_{III} - p_V)/\rho t$$
$$- z_c(\rho_L^{-1} - \rho^{-1})\left(\frac{dp_V}{dt}\right)$$

This equation may be algebraically simplified, but the form presented expedites eliminating computational errors. To use this equation, the temperature derivatives of ρ_L and p_V and H_L are required. The ρ_L derivative is accurately described by the previously stated correlation equation. H_L may be calculated from the Clapeyron equation

$$(H_V - H_L)/RT = z_c\ (\rho_V^{-1} - \rho_L^{-1})\left(\frac{dp_V}{dt}\right)$$

Riedel's vapor pressure equation is not sufficiently accurate to calculate the indicated derivative at low temperatures. The polynominal equation is sufficiently accurate for the enthalpy correction, but not for evaluating H_L near the critical point. The scheme recommended is to use Riedel's equation for evaluating H_L at a t of 0.9 and to then use the correlation from (6) to determine H_L at any other temperature. Specifically

$$(H_V - H_L)_2/(H_V - H_L)_1 = \left(\frac{1.0 - t_2}{1.0 - t_1}\right)^{0.38}$$

where the subscript 1 indicates the value at t = 0.9 and the subscript 2 indicates the value at the desired temperature.
The predicted heat of vaporization is compared to the NBS values

in Figure 5. This correlation for H_v may be used with the Clopeyron equation to develop a correlation for P_v between t = 0.9 and the normal boiling point.

The final enthalpy predictions are compare to NBS enthalpy data in Figure 2; this comparison is very good. The dimensionless excess function is compared to tabulated values of this parameter from (3) in Figure 6. The shape of the two correlations is very close, but some differences are seen in the magnitude of the correction. The comparison in Figure 2 indicates that the HBMS equation of state yields better enthalpy values than the correlations from (3).

- The Two-Phase Region

The quality, s, and saturation properties are related by

$$\rho_{IV} = [s/\rho_V + (1.0 - s)/\rho_L]^{-1}$$

$$H_{IV} = H_V\ s + H_L(1.0 - s)$$

If ρ and t or H are specified, the state is determined. Specifying p and t (or H) does not uniquely determine the state in the two-phase region.

- Low Pressure Enthalpy

H_o is the enthalpy at low pressure which is that of an ideal gas, hence

$$H_o = \int_0^T C_p\ dt$$

Many heat capacity expressions have been reported which use a lower limit of a non-zero reference temperature (including the NBS data (1)); such expressions are not convenient for general flow calculations. The heat capacity correlation recommended is that from (6)

$$C_p = C_{pa} + C_{pb}\ T + C_{pc}\ T^2 + C_{pd}\ T^3$$

The units on C_p are $Btu/lb_m\ R$, and the constants are

$$C_{pa} = 0.20978$$

$$C_{pb} = -7.6040E\text{-}9$$

$$C_{pc} = 1.3407E\text{-}8$$

$$C_{pd} = -3.4079E\text{-}12$$

- Transport Properties

The thermal conductivity is represented by three additive terms

$$k = k_o(T) + k_e(\rho,T) + k_c(\rho,T)$$

where k_o is the low pressure gas contribution, k_e is the excess or dense gas contribution, and k_c is due to enhancement near the critical point. Values for the thermal conductivity taken from (1) are shown in Figure 7. Analytical expressions for k_o and k_e are given in reference (7). These expressions are:

$$k_o = \Sigma\ x_i\ T^i \qquad \text{for } i = 1,\ldots,9$$

$$k_e = \Sigma\ x_i\ \rho^i \qquad \text{for } i = 10,..,15$$

A convenient expression was not given for k_c, therefore step function about the critical point is recommended for describing superconductivity. An 8-fold increase was assumed for the critical point; this factor decreases to zero 2 degrees away from the critical temperature. This increase was estimated from CO_2 data given in (6). The correction is used only at these temperatures and if the density is within ± 5% of the critical value.

The viscosity does not experience abnormal behavior near the critical point so only two terms are needed, one each for the low pressure gas and for the dense gas.

$$\mu = \mu_o(T) + \mu_e(\rho,T)$$

Analytical expressions are given for these terms in (7); values for the viscosity are given in Figure 8. Scant data exist for bulk viscosity, therefore assume it is zero and use only the viscosity to evaluate normal stresses. Normal stresses will be important only for low density gas flows where it is known that the bulk viscosity is small. Note that an erroneous definition is used for bulk viscosity in the NBS report (1), which implies that assuming zero bulk viscosity eliminates all normal stresses. Such is not the case. The correlations for viscosity are:

$$\mu_o = \Sigma\ y_i\ T^i \qquad \text{for } i = 1,\ldots,9$$

$$\mu_e = \Sigma\ y_i\ \rho^i \qquad \text{for } i = 10,..,12$$

Notice that temperature effects on the dense gas contributions to thermal conductivity and viscosity do not appear in the correlations, such effects have not yet been established. The constants are:

x_1 = 9.3648096074E-7 $\qquad$ y_1 = 8.344128902E-7

x_2 = -4.1398868586E-9 $\qquad$ y_2 = -6.4319584704E-9

x_3 = 1.0278371325E-10	y_3 = 1.3385840412E-10
x_4 = -1.0590730434E-12	y_4 = -1.3283970709E-12
x_5 = 5.9317072836E-15	y_5 = 7.4604203289E-15
x_6 = -1.9858382126E-17	y_6 = -2.5398419748E-17
x_7 = 3.9809422422E-20	y_7 = 5.2077731498E-20
x_8 = -4.4173352317E-23	y_8 = -5.9258985472E-23
x_9 = 2.0893500738E-26	y_9 = 2.8773126492E-26
x_{10} = 6.2807950678E-4	y_{10} = 4.7293376329E-4
x_{11} = -4.9337311644E-4	y_{11} = -1.7410413651E-4
x_{12} = 2.5242925212E-3	y_{12} = 5.9995361171E-4
x_{13} = -5.1527923868E-3	y_{13} = 0.65391907848
x_{14} = 5.4461096782E-3	y_{14} = 2.9886313449E-5
x_{15} = -1.8991126599E-3	y_{15} = 9.25

The units on k are W/cm K, and on μ are gm/cm s. T is in K, and ρ is in gm/cm^3. If the density is above 0.932 gm/cm^3, a different correlation equation is used:

$$\mu_e = (y_{13}\ \rho + y_{14}(\exp\{y_{15}\ \rho\}-1.0))/1000$$

If different units are desired, it is more convenient to make the change once the transport property has been calculated. The correlation equations give transport property values comparable to those shown in Figures 7 and 8.

Transport properties in the two-phase region are determined from the quality with an equation like that used to determine enthalpy.

- Closure

The property equations presented herein have been evaluated with a FORTRAN program. The formulation has been presented so that a minimum of terms have to be recomputed during the course of evaluating all of the properties and so that the empirical constants can be identified in terms of the original work from which they were obtained. The properties estimated with the aforementioned code are not intended to be more accurate than the referenced NBS values, but they are of good engineering accuracy and are of a form which is convenient to use when computing flowfields. The FORTRAN code produces files of properties which may be used as tables of data for a CFD calculation.

REFERENCES

1. Roder, H.M., and L.A. Weber, ASRDI Oxygen Technology Survey, Vol. I: Thermophysical Properties, NASA SP-3071 (1972).

2. Weber, L.A., "Extrapolation of Thermophysical Properties Data for Oxygen to High Pressures (5,000 to 10,000 psia) at Low Temperatures (100-600°R), NBS Report 10 727 (1971).

3. Hougen, O.A., et al, Chemical Process Principles, Part II, Wiley & Sons, Inc. (1966).

4. Hirschfelder, J.O., et al, IEC, 50, pp.375-385 (1958).

5. Hirschfelder, J.O., et al, IEC, 50, pp.386-390 (1958).

6. Reid, R.C., et al, The Properties of Gases and Liquids, McGraw-Hill Book Co. (1977).

7. McCarty, R.D., and L.A. Weber, NBS, Tech. Note 384 (1971).

NASA National Aeronautics and Space Administration

Report Documentation Page

1. Report No.	2. Government Accession No.	3. Recipient's Catalog No.

4. Title and Subtitle

Investigation of the Transient Fuel Preburner Manifold and Combustor

5. Report Date

June, 1989

6. Performing Organization Code

7. Author(s)

Ten-See Wang, Yen-Sen Chen, and Richard C. Farmer

8. Performing Organization Report No.

SECA-89-10

10. Work Unit No.

9. Performing Organization Name and Address

SECA, Inc.
3311 Bob Wallace Avenue, Suite 203
Huntsville, AL 35805

11. Contract or Grant No.

NAS8-37461

13. Type of Report and Period Covered

Contractor - Final

12. Sponsoring Agency Name and Address

George C. Marshall Space Flight Center
Marshall Space Flight Center, AL 35812

14. Sponsoring Agency Code

15. Supplementary Notes

Kevin Tucker, MSFC/Technical Monitor

16. Abstract

A computational fluid dynamics (CFD) model with finite rate reactions, FDNS, has been developed to study the start transient of the Space Shuttle Main Engine (SSME) fuel preburner (FPB). FDNS is a time accurate, pressure based CFD code. An upwind scheme was employed for spatial discretization. The upwind scheme was based on second and fourth order central differencing with adaptive artifical dissipation. A state of the art two-equation k-ε(T) turbulence model was employed for the turbulence calculation. A Pade' Rational Solution (PARASOL) chemistry algorithm was coupled with the point implicit procedure. In this study, FDNS was benchmarked with three well documented experiments: a confined swirling coaxial jet, a non-reactive ramjet dump combustor and a reactive ramjet dump combustor. Excellent comparisons were obtained for the benchmark cases. The code was then used to study the start transient of an axisymmetric SSME fuel preburner. Predicted transient operation of the preburner agrees well with experiment. Furthermore, it was also found in this study that an appreciable amount of unburned oxygen entered the turbine stages.

17. Key Words (Suggested by Author(s))	18. Distribution Statement
Transient fuel preburner computational fluid dynamics turbulence finite rate chemistry temperature spikes	unclassified - unlimited

19. Security Classif. (of this report)	20. Security Classif. (of this page)	21. No. of pages	22. Price
unclassified	unclassified	80	

NASA FORM 1626 OCT 86